LASER MASS SPECTROMETRY AND SPECTROSCOPY OF MOLECULES AND SUPRAMOLECULAR COMPLEXES

FRANCISCO GÁMEZ MÁRQUEZ

DIRECTOR: PROF. DR. BRUNO MARTÍNEZ HAYA

UNIVERSIDAD PABLO DE OLAVIDE
FACULTAD DE CIENCIAS EXPERIMENTALES
DEPARTAMENTO DE SISTEMAS FÍSICOS, QUÍMICOS Y NATURALES

Contents

Part I

Laser Desorption Ionization and Gas phase aggregation

0.1 Gas phase ions.

A vast part of processes of chemical interest take place in a condensed phase. The microscopic description of condensed phases is a challenging task. Simplified environments become necessary in order to gain insights into the intrinsic molecular properties and behavior that are responsible for nanoscopic and mesoscopic phenomena. The isolation of molecular systems in the gas phase, or in cold inert molecular matrices, provides such an environment. Isolated systems can be characterized with a variety of modern spectroscopic and mass spectrometric techniques that probe their structure and interactions. The precise definition of the molecular framework that is achieved in this approach also provides a valuable reference to validate quantum chemistry and molecular modelling methods. Moreover, the combination of experimental and theoretical techniques allows to sketch the conformational pathway from gas–phase to solution through a stepwise microsolvation of the molecular systems under study. The interested reader is referred to the recent textbook of J.P. Schermann for an extended overview on these topics [1].

Transfering intact molecules from a condensed phase to the gas phase under controlled conditions is far from trivial. If the molecule is thermostable and has a sufficiently low melting point, transference is possible by moderate heating the sample. This is however not the case for organic molecules of sufficiently high molecular case (above 500 amu), nor it is for polymers and most biomolecules. This work deals mainly with gas phase molecular ions that cannot be produced by traditional techniques (sample heating, electron impact, etc). Among the soft (non-fragmentative) molecular ion sources available nowadays, this investigation makes extensive use of laser-desorption-ionization (LDI) and of electrospray ionization (ESI) techniques. The development of these techniques is relatively recent and was recognized with the 2002 Nobel Price in Chemistry received by Koichi Tanaka [2, 3] and John Fenn [4] in 2002.

0.1.1 LDI-like techniques

LDI

When a material absorbs a short laser pulse of sufficient power it melts and vaporizes with a degree of molecular decomposition and ionization that depends on laser energy and the intrinsic characteristics of the material. This process is called Laser Desorption ionization (LDI).

Mechanisms responsible for material ejection in LDI can be of mechanical and/or thermal nature. Considering these two limiting mechanisms, it is possible to determine a thermal and mechanical time-scales for relaxation as $\tau_{thermal} = L_{abs}^2/D$ and $\tau_{mech} = L_{abs}/c$ respectively, where c is the speed of sound, D the thermal diffusivity and L_{abs} the penetration depth of the laser beam into the material. Hence, when the laser pulse duration $\tau < \tau_{thermal}$ (thermal confinement conditions) relaxation of the excess energy occurs almost solely *via* heat diffusion and dominates for experiments in the UV region with nanosecond lasers. On the other hand, relaxation occurs through mechanical waves when $\tau < \tau_{mech}$ (stress confinement conditions). In addition, explosive boiling may take place at high laser fluences as a consequence of competitive energy consuming processes inducing as bubbles/clusters formation and ejection. This topic has been addressed in a comprehensive review by Georgiou and Koubenakis [5].

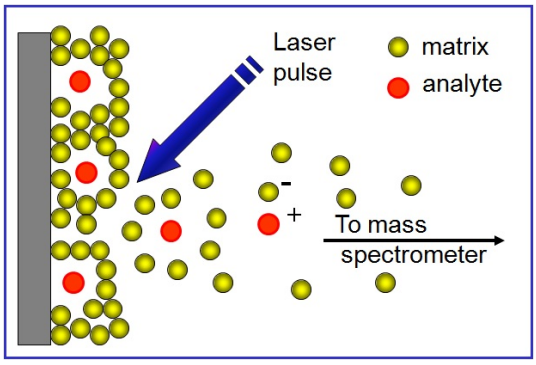

Figure 1: Schematic representation of the MALDI process (adapted from ref. [9])

LDI is likely to induce fragmentative processes in thermolabile molecules. A way to avoid this drawback consists in introducing an organic chromophore as matrix capable of assisting the codesorption of the analyte of interest at low laser powers. This is the so-called MALDI technique (see below). Nevertheless, the first part of this thesis deals mainly with matrix-less LDI methodologies. The aim behind this approach is to study gas phase processes free of matrix effects and to investigate the aggregation/fragmentation pathways of benchmark molecular systems (in the present case, polyaromatic hydrocarbons) in different background environments. The lack of matrix is also a crucial aspect in analytical applications focused on low mass species (e.g. metabolomics).

MALDI

MALDI is a technique aimed at the enhancement of the laser desorption/ionization process. For this purpose, the analytes of interest are diluted in an organic chromophore matrix that efficiently absorbs the laser radiation. In the most common applications the matrix molecules are good proton donors or acceptors in order to ionize the analytes. MALDI provides a soft non–

destructive route for the mass spectrometry analysis of molecules with high molecular weight and has become a keystone technique in biotechnology as well as in the industrial analysis of materials.

The general mechanism underlying MALDI process is still under debate because of the many factors affecting the desorption and ionization processes, such as the analyte/matrix concentration, their chemical nature or the laser parameters. None of the models proposed to date account for the whole complex path from the neutral solid sample to the ionized gas phase molecules. Consequently, the development and optimization of MALDI methods have involved a high load of empirical work. Nevertheless, it is broadly accepted that MALDI occurs in a two stage mechanism leading to primary and secondary ionization pathways in the desorption plume. It is illustrative to briefly outline these two steps. One of the early models for the primary ionization step is the cluster or "lucky survivors" model of Karas [6]. Many modifications of the original model have been described, but the idea is that ions are preformed in the sample, and hence, laser has the only function of eject the molecules from the solid phase by inducing mechanical charge separation. The released material contains both matrix and analyte molecules and the final charged and clustering state of the resulting ions is the consequence of intracluster redistribution and matrix desolvation reactions. The mechanism proposed by Karas might be relevant under certain operation conditions, in particular for dried-droplet sample preparation (coprecipitation of matrix and analyte) and especially for IR-MALDI. However, it does not describe many of the features observed for UV-MALDI. Also importantly, it cannot account for the efficiency of solvent-free MALDI for which the sample is a mixtures of fine powders of the matrix and the analyte. An alternative perspective of the MALDI process is based on multiphoton ionization mechanisms combined with energy pooling effects that concentrate excitons on single desorbed molecules [7, 8]. This type of models is consistent with the common observation of hot-spots on MALDI samples where the laser incidence leads to particularly large ion yields. The primary ions originated in this way expand into the plume and reach a low density regime that is kinetically controlled by neutral matrix-analyte collision rates where secondary ionization follows via protonation, cationization and/or electron transfer occur. The net effect is that a measurable amount of ionized molecules is obtained from a non-destructive laser fluence as is schematized in Fig. 1.

LDI assisted by nanostructures (NALDI)

Significant efforts have been devoted to the development of matrix-less LDI methods that avoid some of the limitations of MALDI. Among the main drawbacks related to the use of organic matrices are the requirement of physicochemical compatibility with the analyte and the background signal generated in the low mass range. Optically active nanoparticles and nanostructured substrates have received much attention in this context. The use of metal nanoparticles as LDI substrates is in fact older than the demonstration of conventional MALDI [2, 10, 11, 12, 13]. A broad range of nanostructured LDI substrate materials have been reported in the past two decades. Early investigations employed porous silicon as desorption/ionization assistant -i.e the so–called DIOS technique [14]. More recently, micrometric and nanometric metal and semiconducting metal oxide interfaces with or without coatings [19] have been employed as LDI assisters. These include carbon nanotubes [20], activated carbon [21], mesoporous compounds [22], nanowires [23] and microcolums arrays [24]. A revival of the field is currently taking place which is fueled by the advent of efficient synthetic routes to produce nanoparticles functionalized for the binding of specific chemicals species.

The mechanism of the Assisted or Enhanced Laser Desorption Ionization by inorganic nanostructured materials (referred to in the literature as SALDI, SELDI or NALDI) is very much dependent on the electronic, optical and geometrical properties of the substrate [15]. A common aspect to nanometric interfaces is of course the high specific surface available for interaction with the analytes during the early stages of the desorption process. For metal nanoparticles quantum size effects, such as plasmonic absorption [16] or radiation-trapping [18] are particularly relevant and yield pathways for energy and charge transfer through electromagnetic field enhancement not available in conventional MALDI. Radiation trapping is a phenomenon in which photons are subsequently absorbed and emitted by atoms in a system and is most prominently observed in very small nanoparticles. On other hand, surface plasmons are quasiparticles that result from the collective oscillations of metal electrons confined within a dielectric/conductor interface. In nanoparticles, plasmons are localized and their photon excitation results in high local electric fields that are known to enhance light absorbance, fluorescence and inelastic dispersion (Raman) by molecular adsorbates. A recent review on nanoparticles uses in mass spectrometry [17] gives a overall perspective of the state–of–the–art of this research field in both mechanisms knowledge and applications in metabolomics, proteomics or imaging.

In this work, we explore two different types of nanomaterials as LDI active substrates. On one hand, gold nanoparticles of different size and geometry are applied in order to tune plasmonic absorbance in spectral ranges from the near-ultraviolet to the visible and near infrared. On the other hand, we employ nanostructured TiO_2 semiconductor substrates obtained by Pulsed Laser Deposition (PLD) [25]. Semiconducting substrates display a broad band optical absorption above their energy band-gap. PLD constitutes a reliable method for deposition of thin films of controlled properties. The size,

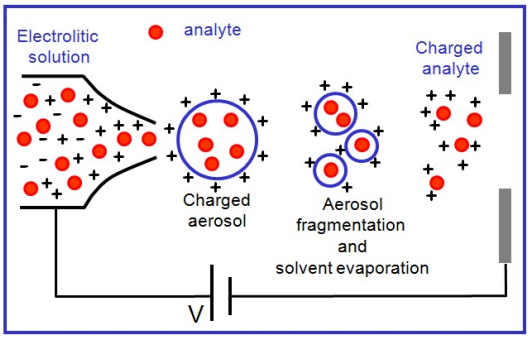

Figure 2: Schematic representation of the ESI process addapted from [9]

distribution and density of the interfacial nanostructures depends on the ablation mechanisms, and can be modulated by technical parameters such as laser pulse duration, deposition time or distance from surface to spot.

0.1.2 Electrospray Ionization ESI

In ESI experiments, ions are transferred from a solution to the gas phase by means of charged aerosols that decompose to charged analytes upon solvent evaporation as sketched in Fig. 2. While, the mechanisms underlying the ESI process are still poorly understood, it is accepted that the following three consecutive steps occur: (a) Production of charged microdroplets (aerosols) at the exit of the electrospray tip, where an electric field of up to 10^6 V m^{-1} is applied. The electric field polarizes the solution and and causes a electrophoretic flux that eventually breaks up into nearly monodisperse small droplets; (b) The solvent in the droplets evaporates at constant charge until the charge-to-diameter ratio becomes small enough as to induce Coulomb instability. That occurs when the surface tension adhesion becomes lower than electrostatic repulsion and the droplet disaggregates explosively into smaller droplets, each of them carrying a part of the solvated ions; (c) The final formation of a the isolated gas-phase ions from the smaller droplets is one of the worst known processes in ESI. Two models, namely the charge residue (CR) model [26] and the Ion Evaporation (IE) [27] model give partial explanations for this final step of the ion formation. Briefly, the IE model is based on transition state theory concepts and establishes that the ions are ejected from the droplets before its complete evaporation. This appears to be the case for small molecular ions. On the other hand, the CRM model assumes that ion isolation occurs only *via* solvent evaporation and the original charge of the droplet is retained by the solute molecule. In any case, it is a fact that the ESI process generates multiply charged ions (in contrast to MALDI) and is therefore capable of producing heavy gas phase ions with small m/z ratios.

MALDI apparatus at UPO and o-TOF system at Muenster

We will present the result of MALDI investigations of polymers and hydrocarbons. A significant part of this part of the thesis project was devoted to the development of LDI active substrates based un metal and semiconducting nanostructures. The bulk of the experiments have been performed in a home-made MALDI-TOF equipment already described elsewhere [28]. Briefly, it consists of a ion source of Wiley-McLaren type in which the MALDI sample is inserted in the repeller plate. The laser beam is focused thorugh a quartz or a CaF_2 window on the sample plate at a 45 degree incidence with a covex lens of 25 cm focal length. The ions generated inthe LDI process are accelerated by a pulse-controlled voltage of typically 4.2 kV. The delay between the laser pulse and the application of the ion extraction voltage can be varied from zero (continuous ion extraction) up to several microseconds. The typical delays employed in our experiment were within 0.5–1.0 μs. The ions are accelerated in the ion source into a time-of-flight (TOF) spectrometer (Jordan TOF Products, Inc.) The ion source provides the same kinetic energy to all the ions (having the same charge), so that the ions are mass separated in the field-free TOF tube according to their mass/charge ratio and detected in a Multichannel plate (MCP) detector, where the signal is amplified and collected in a fast digital oscilloscope. The mass resolution is improved by operating the spectrometer in reflectron mode, i.e. ions are reflected and describe a "V-shape" trajectory towards an additional MCP detector. The reflectron method corrects for the spread in initial velocities of ions with the same m/z ratio produced by the LDI process. The time of flight scale is converted into a mass spectrum with the proper external calibration with known mass analytes with m/z values in the range of interest.

The ion source and TOF chambers are kept at high vacuum (about 10^{-7}torr) with a turbomolecular pump system. A view of the TOF tube and ionization chamber are provided in Fig. 3 and Fig. 4.

Our laboratory at UPO has a versatile laser equipment for spectroscopic and mass spectrometry experiments. Fixed and tuneable laser systems are available covering an spectral range from the near UV to the mid-infrared. Two Nd:YAG pumped dye laser systems can generate radiation within 200-800 nm, while an optical parametric oscillator system (OPO) produces visible and near and mid-infrared laser pulses (1.2-5 μm). The projects presented in this thesis report were nevertheless performed with a Q-switched Nd:YAG laser (Minilite II, continuum) delivering the fundamental emission at 1064 nm, and the three harmonics at 532, 355 and 266 nm. The system produces laser pulses of 10 ns duration, at a repetition rate of 10 Hz. The actual setup of the system are depicted in Fig. 5.

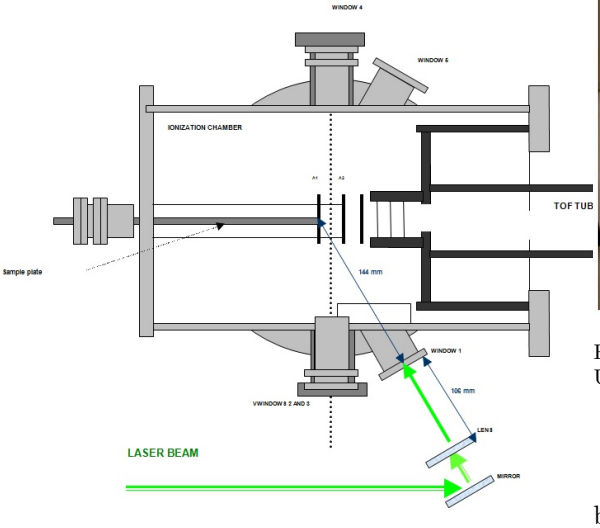

Figure 3: View of the ionization chamber design of the MALDI system at UPO

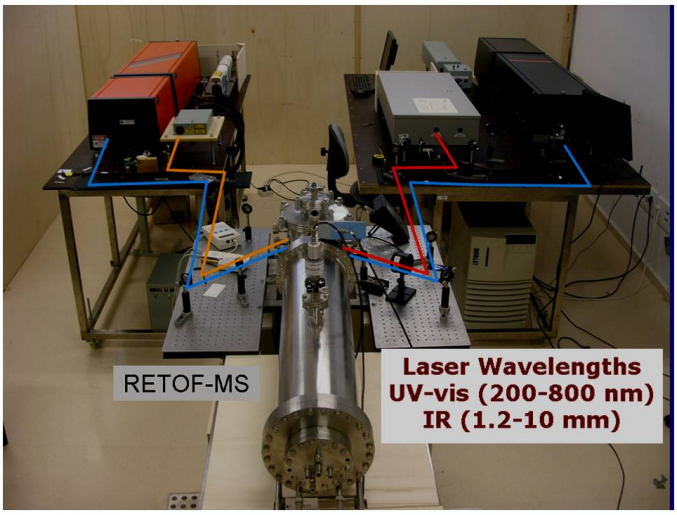

Figure 5: Laser setup and ubication in the MALDI laboratory at UPO.

Part of the investigation on polyaromatic hydrocarbons and asphaltenes required the control of the background pressure of the ion source chamber. The background gas was employed to collisionally relax the molecules and ions desorbed in the LDI proces. These experiments were not possible with our equipment and were performed through a collaboration with the group of Klaus Dreisewerd at the University of Münster (Germany) in an orthogonal extraction TOF spectrometer (o-TOF) that has been described elsewhere [29]. In this system, the ions are thermalized with a N_2 gas bath of up to 1.5 mbar pressure in a quadrupolar ion-guide oriented at 90 degrees with respect to the ion source, and collinear with the axis of the TOF spectrometer. A simple scheme is depicted in Fig. 6.

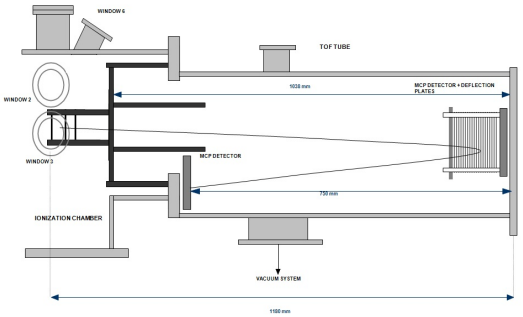

Figure 4: View of the ionization chamber design of the MALDI system at UPO

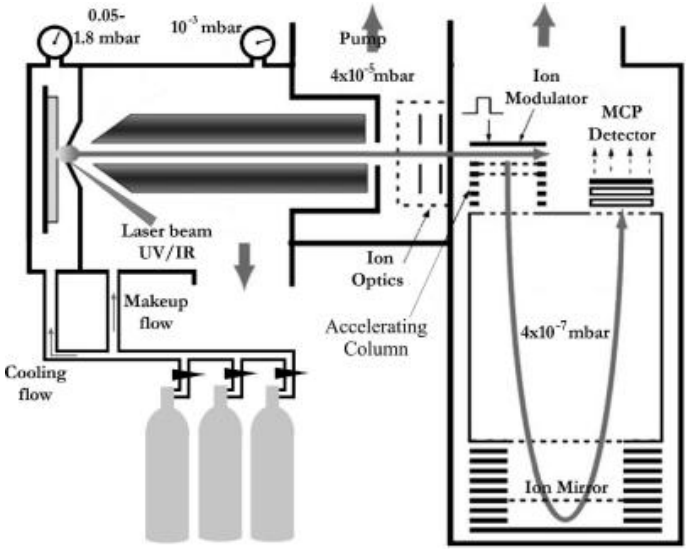

Figure 6: View of the o-TOF MALDI system described in the text.

Bibliography

[1] J.P. Schermann Spectroscopy and Modelling of Biomolecular Building Blocks Elsevier, Amsterdam 2008.

[2] K. Tanaka. The Origin of Macromolecule Ionization by Laser Irradiation. Nobel Lecture, 2002.

[3] K. Tanaka, H. Waki, Y. Ido, S. Akita, Y. Yoshida, Rapid Commun. in Mass Spectrom. 2 (1988) 151.

[4] J. Fenn Electrospray Wings for Molecular Elephants, Nobel Lecture, 2002.

[5] S. Georgiou, A. Koubenakis, Chem. Rev. 103 (2003) 349 and references herein.

[6] M. Karas, M. Glückmann, J. Schäfer. J. Mass Spectrom. 35 (2000) 1.

[7] H. Ehring, M. Karas, F. Hillenkamp. Org. Mass Spectrom. 27 (1992) 427.

[8] P. Setz, R. Knochenmuss. J. Phys. Chem. A. 109 (2005) 4030.

[9] B. Martínez-Haya. An. Quím. 107(4) (2011) 367.

[10] T. W. Hutchens, T. Yip. Rapid Commun. Mass Spectrom. 10 (1996) 1927.

[11] S. D. Cornett, T. D. Lee, J. F. Mahoney. Rapid Commun. Mass Spectrom. 8 (1994) 996.

[12] F. G. Hopwood, L. Michalak, S. D. Alderdice, K. J. Fisher, G. D. Wilett. Rapid Commun. Mass Spectrometry. 8 (1994) 881.

[13] Q. Zhan, S. J. Wright, R. Zenobi. J. Am. Soc. Mass Spectrom. 8 (1997) 525.

[14] J. Wei, J. M. Buriak, G. Siuzdak. Nature 399 (1999) 243.

[15] J. Sunner, E. Dratz, Y. Chen. Anal. Chem. 67 (1995) 4335.

[16] S. Eustis, M.A. El-Sayed. Chem. Soc. Rev. 35 (2006) 209.

[17] J.A. Stolee, B.N. Walker, V. Zorba, R.E. Russo, A. Vertes. Phys. Chem. Chem. Phys. (2012) DOI:10.1039/C2CP00038E and references therein.

[18] E. P. C. Lai, S. Owega, R. Kulczycki. J. Mass Spectrom. 33 (1998) 554.

[19] T. Kinumi, T. Saisu, M. Takayama, H. J. Niwa. J. Mass Spectrom. 35 (2000) 417.

[20] C. H. Wang, S. J. Li, Y. L. Guo, X. H. Xia. Anal. Chim. Acta 604 (2007) 158.

[21] M. J. Dale, R. Knochenmuss, R. Zenobi. Anal. Chem. 68 (1996) 3321.

[22] Z. Shan, L. Han, Y. Minjia, C. Deng, D. Zhao, B. Tu, P. Yang. Anal. Chim. Acta 593 (2007) 13.

[23] E. P. Go, J. V. Apon, G. Luo, A. Saghatelian, R. H. Daniels, R. Sahi, R. Dubrow, B. F. Cravatt, A. Vertes, G. Siuzdak. Anal. Chem. 77 (2005) 1641.

[24] Y. Chen, A. Vertes. Anal. Chem. 78 (2006) 5835.

[25] R. Eason. Pulsed Laser Deposition on thin films: Applications-Led Growth of functional materials. Wiley-Interscience (2006). ISBN-10: 0471447099.

[26] a).- M. Dole, L. L. Mack, R. L. Hines, R. C. Mobley, L. D. Ferguson, M. B. Alice. J. Chem. Phys. 49 (1968) 2240; b).- G. Schmelzeisen-Redeker, L. Kebarle, F. W. Rollgen. Int. J. Mass Spectrom. ion. Proc. 90 (1989) 139.

[27] a).- J. V: Iribarne, B. A. Thomson. J. Chem. Phys. 64 (1976) 2287; b).- B. A. thomson, J. V. Iribarne. J. Chem. Phys. 71 (1979) 4451.

[28] A. R. Hortal. PhD Thesis. Universidad Pablo de Olavide (2007).

[29] A. V. Loboda, S. Ackloo, I. V. Chernushevic. Rapid Commun. Mass Spectrom. 17 (2003) 2508.

Chapter 1

Pressure-dependent Laser Desorption Ionization Study of Polyaromatic hydrocarbons and asphaltenes

Model polyaromatic hydrocarbons (PAHs) have been investigated with LDI–MS experiments. The study focuses on the characterization of the in–plume fragmentation and aggregation processes that take place under different background pressures of an inert gas. The dominant fragmentation channels are related to H_2–loss (from concerted C-H cleavage). Ring fragmentation and cleavage of C–C linkages between aromatic cores are also observed, although the precise patterns vary significantly among the PAHs. Whereas fragmentation occurs readily in LDI under vacuum, it is largely suppressed when the laser desorption is performed with a moderate pressure of background cooling gas (1.2 mbar of N_2). Aggregation proceeds both covalently, via recombination of radical fragments, and non-covalently, presumably through π–π stacking. Similar experiments were also performed on asphaltenes from crude oil. The results allow to draw tentative conclusions about the complex molecular architecture of asphaltenes.

1.1 Introduction

The investigation of complex mixtures of hydrocarbons with laser desorption/ionization mass spectrometry (LDI-MS) techniques has been intensively investigated in the past decades. In the study described in this chapter we apply this technique to polyaromatic hydrocarbons (PAHs) of different molecular structure in order to understand the dominant ionization pathways and the related fragmentation and aggregation processes.

The electronic structure of PAHs can change significantly as new fused rings are incorporated to their structure. For instance, the photostability is largely affected by the size of the PAH core and by its pericondensed (sheet–like) or catacondensed (chain–like) fused ring architecture. Supramolecular aggregation is of course also affected by molecular architecture as it is driven mainly by the competition between the attractive dispersive forces of the aromatic cores and the repulsive steric interactions introduced by the side alkane chains [1].

In this chapter, we follow an approach scarcely explored in the past to characterize the photochemistry and gas-phase supramolecular behavior of model PAHs. The methodology is based on investigating the LDI of the PAH molecules under different background pressures to modulate the fragmentation, aggregation and polymerization processes occurring in the desorption plume. The LDI and MALDI techniques are nowadays commonly applied both under vacuum (pressures below 10^{-6} mbar) and at atmospheric pressure [2]. Our experiments will employ intermediate pressures, within the 10^{-3} mbar range, in order to control the internal energy of the desorbed molecules and quench or enhance different photochemical pathways. We show that the desorption/ionization occurring at intermediate controls efficiently the metastable decomposition of the PAHs (in– and post–source decay) which provides relevant information about the relation between structure and photophysical/chemical properties of PAHs and allows to discern between non-covalent and covalent association processes.

In the second part of the investigation described in this chapter, the observations for the model PAHs are employed to understand the outcome of similar experiments performed on asphaltene samples. Asphaltenes conform a complex extract of crude oil that is defined by convention as the fraction of *n*–heptane/insoluble–toluene/soluble (or similar solvents depending on the definition) compounds. This definition includes a broad range of chemical compounds with relatively heavy masses and large polarities within the crude oil. Asphaltenes are of practical importance since their tendency to nanoaggregate and stack interferes in heat transfer, lubrication, transport and efficiency in the combustion of the fuel. The aggregation propensity of asphaltenes has been in fact the cause of a long misunderstanding concerning their molecular weight distribution (MWD) as measured from different instrumental techniques. The scientific discussion of this matter seems to have finally settled, with a relevant contribution from the LDI experiments in our group employing both single–colour and two–colour schemes [3, 4, 5]. The dominant architecture of asphaltenes appears to consist of one central PAH core (occasionally two cores) with eventual heteroatoms and side aliphatic arms.

Recently, high resolution MS methods, in particular Fourier Transform Ion Cyclotron Resonance Mass Spectrometry (FTICR-MS) pioneered by A. Marshall in Florida, has had a crucial impact in the oil industry. This has led to a rapid development of the field of *petroleomics*, defined as "the characterization of the petroleum at molecular level" [6]. Indeed, FTICR-MS displays an unprecedented accuracy for the determination of the exact mass of any compound, and it is therefore capable of defining the precise stoichiometry of the thousands of components that are typically present in natural hydrocarbon samples, such as asphaltenes.

The resolution of the present LDI experiments (ΔM/M$\approx$6000) is about two orders of magnitude lower than the one achieved with modern FTICR-MS systems. Nevertheless, LDI equipments are significantly less expensive and are readily available in many laboratories worldwide. Hence, we have kept in mind the recent advances in the field and have tried to extract as much compositional and structural information as possible from the LDI spectra of the asphaltenes. In particular, we have employed a genetic algorithm to extract relative populations of different families of compounds from the mass spectra. The LDI photochemical response of those compounds at different background pressures is then employed to infer their dominant polyaromatic architecture.

1.2 Experimental and Calculation Methods

1.2.1 Mass Spectrometry analysis

The UV-MALDI-o-TOF Mass Spectrometer employed in these studies is a modified prototype similar to the MDS Sciex prOTOF 2000 instrument, and has been already described in ref. [8]. The N_2 background pressure in the ion source and in the interface region, housing the collisional focusing transfer quadrupole, were controlled with two gas inlet valves. Four different ion-source pressures were employed in this study, namely 0.05 (vlp), 0.2 (lp), 0.6(np) and 1.2 (hp) mbar. The pressure in the quadrupole ion guide was adjusted to 0.003 mbar throughout the experiments. The N_2 (337 nm) laser

repetition rate is 30 Hz and about 3 min sampling was recorded per spectrum. Since the PAHs considered in this study have ionization potentials around 7 eV [7], at least two photons are required for ionization. The laser energy was kept at 30 μJ/pulse. Samples for the LDI measurement were simply deposited in the form of powder. The sample plate was constantly moved during data acquisition to irradiate the entire sample area.

1.2.2 Mass spectra analysis

All the relevant peaks in the spectra were fitted by including lorentzian peaks centered on the exact masses given by the possible stoichiometries of the observed products. In particular, all plausible C_nH_m compounds (with masses n*12.000 + m*1.008) and their natural isotopes were considered. The intensity associated to each species was determined from the best fit of the mass spectrum, performed with a genetic algorithm outlined below. The corresponding FORTRAN code is included as supplementary material at the end of this chapter.

In the genetic algorithm, the mass spectrum $S(W)$ is considered to be the sum of mass peaks $\mathfrak{L}(W_i)$ centered on the mass of each C_nH_m compound with intensities α_i (the width of the peaks is given by the experimental resolution):

$$S(W) = \sum_i \alpha_i \mathfrak{L}(W_i) \tag{1.1}$$

A population of n_g "chromosomes" of sets of α_i genes are constructed. Each chromosome is ordered according to the difference δ between the experimental and the corresponding "genetic" spectrum associtae with it. The chromosomes are then sequentially mutated according to the following rules:

1.- 65 % of the chromosomes with the smaller δ value remains unchanged.
2.- 5 % of the new chromosomes are generated by changing a randomly chosen chromosome and change their genes in a maximum of 5 %.
3.- 10 % of the new population are the result of a modification of maximum 0.5% some gene of a randomly chosen chromosome from the first positions of the listed ones. 4.- 10 % of the new generation are generated by interchanging of genes (at least one) between two randomly chosen chromosomes among the second quartil.
5.- The last 10 % of chromosomes are generated by averaging the genes of two chromosomes belonging to the second decil.

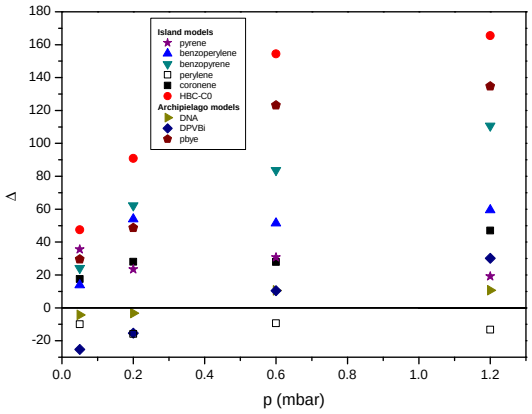

Figure 1.1: Deviation of the computed average molecular mass to the nominal one.

The evolution follows until a predefined maximum number of steps, or the δ value reaches the desired tolerance.

1.3 Results

The direct evaluation of the average molecular mass of the PAH LDI products provides a first clue about the aggregation/fragmentation behavior that each model compound, under different pressure conditions. We have calculated it directly from the measured mass spectra $f(W)$:

$$\langle W \rangle = \frac{\int f(W)\, W dW}{\int f(W) dW} \tag{1.2}$$

It can be observed in Fig. 1.1, that only the less pericondensed archipielago PAHs have negative deviations at the lowest pressure. This is indicative of their lower stability under increasing laser fluence. On the contrary, there exists a general trend to aggregation as long as steric effects (due to side chains) diminish and the overall ring number becomes bigger.

Let ut now discuss in detail the results obtained from the mass spectra recorded for the different model PAHs and for the UG8 asphaltene. As a sample, in Fig. 1.2, we show an example of the calculated and experimental mass spectrum together with the extracted relative population.

"ISLAND"-TYPE PAHs

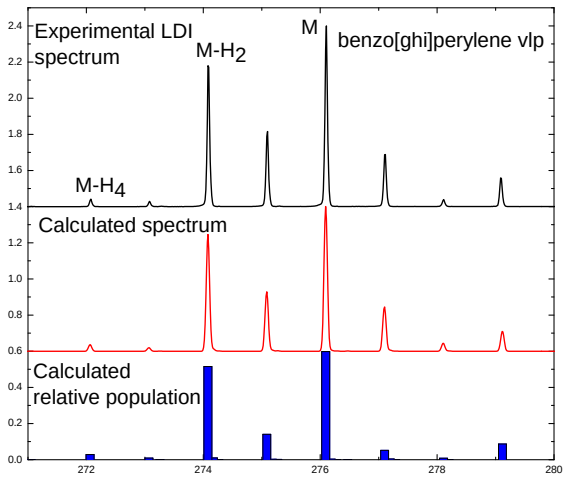

Figure 1.2: Experimental (black) and calculated (red) mass spectrum for a model PAH. The blue columns representd the best gene obtained in the minimization process of the genetic algorithm.

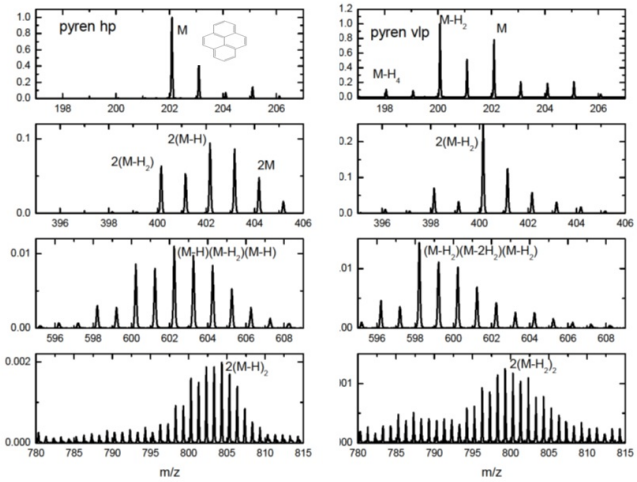

Figure 1.3: Experimental LDI mass spectra of pyrene.

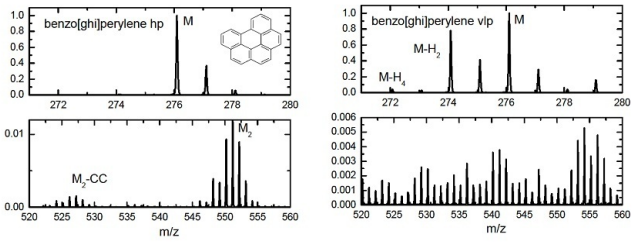

Figure 1.4: Experimental LDI mass spectra of benzo[ghi]perylene.

Four ring species:

a).- Pyrene $C_{16}H_{10}$. **I-1**

This four ring unsubtituted PAH has a nominal mass of m/z 202 (Py, $C_{16}H_{10}$, exact mass 202.078). The corresponding LDI spectra are shown in Fig. 1.3. The radical cation $C_{16}H_{10}^{+}$ is stabilized under background pressure, while a major component corresponding to the dehydrogenation channel (concerted loss of H_2) is observed for LDI under vacuum. The Py_2 non-covalent dimer stabilized by π–π stacking is only observed at high pressure. Due to the small number of rings, such aggregation process is not very efficient and the high degree of aggregation observed in the spectra is mainly due to covalent linking between dehydrogenated radicals. It is also observed the general trend of increasing fragmentation (with main components corresponding to lost of a CH) as pressure diminishes.

Five ring species:

a)**Benzo[ghi]perylene ($C_{22}H_{12}$, I-2)**: The parent ion (276 m/z) is provides the most intense peak at both pressures, but the dehydrogenated adduct competes with it at low pressure (see Fig. 1.4). At high pressure the main dimer channel is the non-covalent dimer, whereas at low pressure the covalent link between two dehydrogenated monomers is most intense. The product pattern is however considerably more complex than the one found for pyrene and a broader range of covalent species are formed associated with the loss of a different number of H atoms. Loss of full C-C chains is also a relevant process for this PAH. Overall, the largest size of the the clusters decreases from 5 monomers at high pressure to about 3 in the low pressure regime.

b)**Benzo[a]pyrene ($C_{20}H_{12}$, I-3)**: The experimental mass spectrum of this PAH is depicted in Fig. 1.5. The parent ion (252 m/z) is dominant at high pressure, while dehydrogenation and large scale fragmentation routes become more relevant at low pressure. Stacking aggregation is enhanced –and dominates- at high pressure, with about 20 % of intensity corresponding to –H and -2H covalent dimers.

c)**Perylene ($C_{20}H_{12}$, I-4)**: The dehydrogenatation channel is observed at the lowest pressure condition, while the parent ion dominates the ion yield at high pressure conditions as observed in Fig. 1.6. Aggregation phenomena are not predominant in the spectrum.

Six ring species

d)**Coronene ($C_{24}H_{12}$, I-5)**: The pressure–

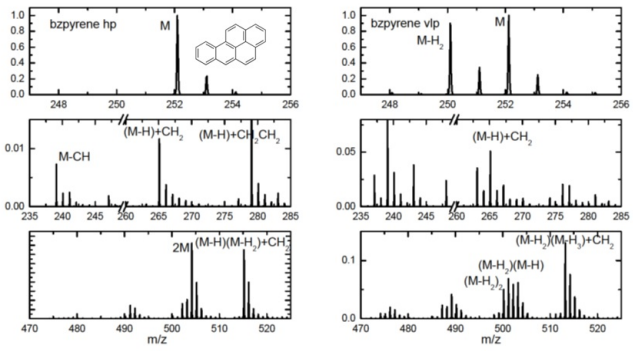

Figure 1.5: Experimental LDI mass spectra of benzo[a]pyrene.

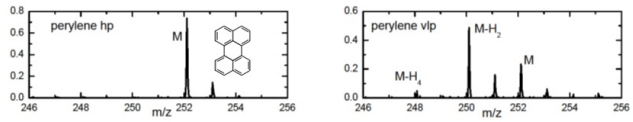

Figure 1.6: Experimental LDI mass spectra of perylene.

dependent behavior of this prototypical PAH model is shown in Fig. **??**. The parent ion (m/z 300) is the principal channel at both pressures, but competes with the dehydrogenated adduct at the lower pressure. The stacking dimer (53 % population) competes with dicoronilene (the covalent dimer -4H) and the -2H and -1H dimers at high pressure, but it is absent at low pressure where the -2H/1H dimers diminish their intensity. The maximum aggregation number decreases from 9 to 3 as pressure decreases, but stacking loses importance as the monomer number increases.

larger PAHs:

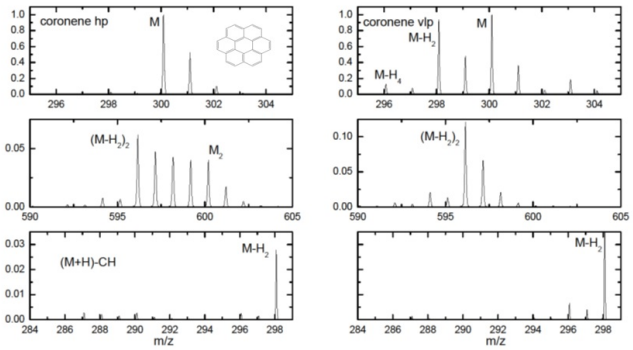

Figure 1.7: Experimental LDI mass spectra of coronene.

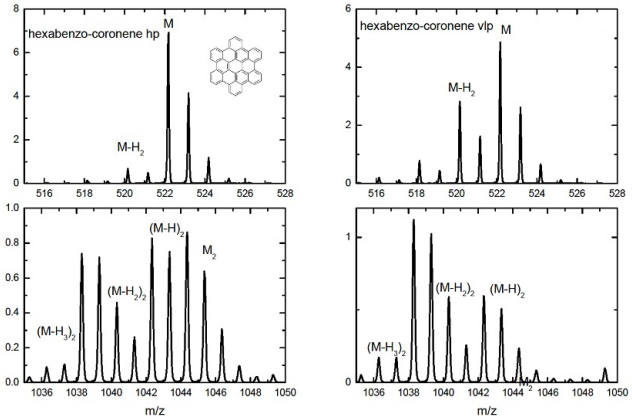

Figure 1.8: Experimental LDI mass spectra of HBC

e) **Hexabenzocoronene ($C_{42}H_{18}$, I-6)**: Mass spectra for this compound are shown in Fig. 1.8. At high pressure, the parent ion dominates, and the dimer is predominantly formed from monomers that have lost two or three H atoms. The predominance of complexes formed from the union of monomers after the cleavage of an odd number C-H bonds is noticeable. This is in consonance with the results obtained in Ref.[9].

'ARCHIPIELAGO'-TYPE PAHs

f)**4-4'-Bis(2,2-diphenyl-ethen-1-yl)biphenyl (DPBVi, $C_{40}H_{30}$, A-1)**: The main peak observed high pressure is the parental ion (m/z 510, see Fig. 1.9). Traces of aggregation of covalent character is observed. In contrast, in the low pressure regime, significant aggregation does not take and fragmentation becomes quite relevant. The most common fragments (not shown) are related to the loss of a bencylbencene ($C_{13}H_{12}$, 339 m/z) and two bencyl groups follows by a sequence of peaks corresponding to CH groups (352 m/z).

g) **1,4-Di(pyren-1-yl)benzene(pBye) ($C_{38}H_{22}$, A-2)**: The m/z pattern shows in Fig. 1.10 is very similar at all the pressures investigated. The dominant peak corresponds to the loss of 4H (two H_2 molecules), but with a higher intensity of the parent ion at high pressure. Aggregation has a covalent character and is more noticeable at higher pressures. The secondary peak is due to a pyren group (276 m/z). Notice this is the more "island–like" compound among the archipielago models considered in the study.

h) **9,10-Di(naphth-2-yl)anthracene (ADN) ($C_{34}H_{22}$, A-3)**: The parent ion at 430 m/z is the

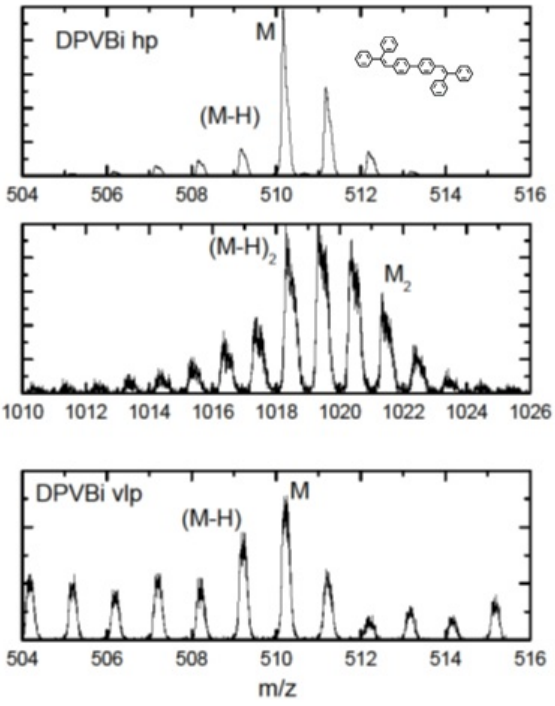

Figure 1.9: Experimental LDI mass spectra of DPBVi.

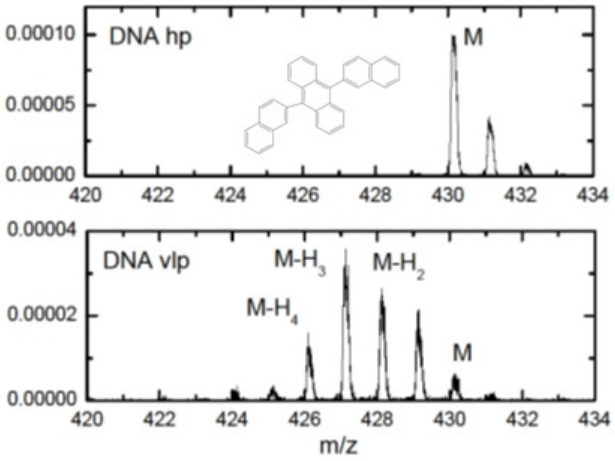

Figure 1.11: Experimental LDI mass spectra of ADN.

only observable species in the mass spectrum at high pressure (Fig. 1.11). At the low pressure condition, the loss of a lateral naphthyl group (not shown) is the preponderant peak, and as concerned to the monomer region, poly-dehydrogenation also occurs as in the preceding island models. No significant aggregation is observed at any pressure and are also visible species generated by the loss of C_nH_m groups, with n=1,2.

THE UG8 ASPHALTENE

the same methodology employed for the model PAH samples was applied to a complex mixture of polyaromatics, namely the UG8 asphlatene extract from crude oil. This material has been analyzed by LDI in our group in several studies included in the Ph.D. thesis of Paola Hurtado [10]. Here, we investigate the result of LDI experiments on a UG8 sample under different background pressures, seeking to correlate the fragmentation and aggregation propensities observed with the molecular architecture postulated for asphaltenes.

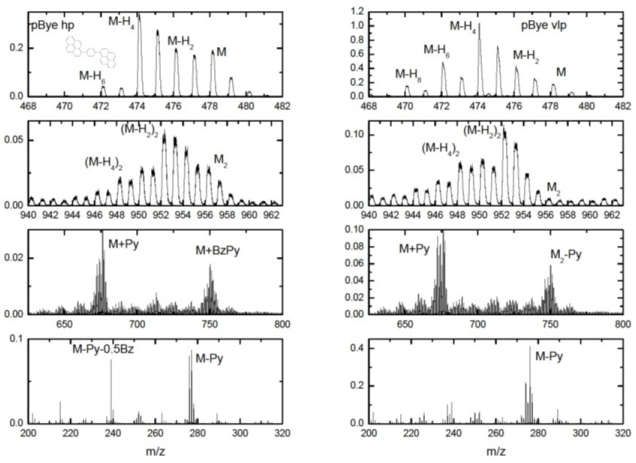

Figure 1.10: Experimental LDI mass spectra of pbye.

Fig. 1.12 shows that the UG8 asphaltene displays a limited degree of fragmentation and a significant propensity to aggregate into heavier compounds. Fig. 1.13 shows the a representation of the average molecular weight, $\langle W \rangle$, versus laser power. The aggregation and fragmentation regimes at moderate and at high laser powers, respectively, can be appreciated. This behavior is similar to the one found for the island–like PAHs and, hence, asphaltenes can be expected to have dominant molecular structures of this kind.

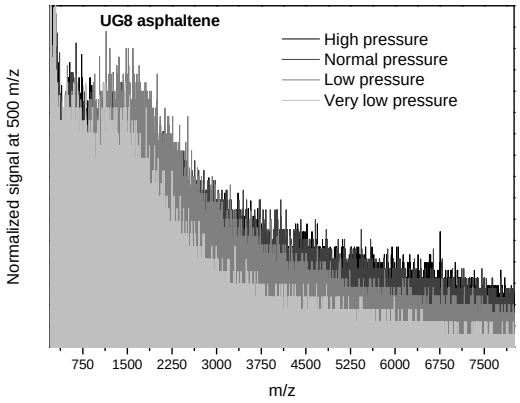

Figure 1.12: Experimental mass spectra of asphaltene UG8 under different pressure in the ionization chamber. Notice the intensity has been normalized at the intensity at 500 m/z

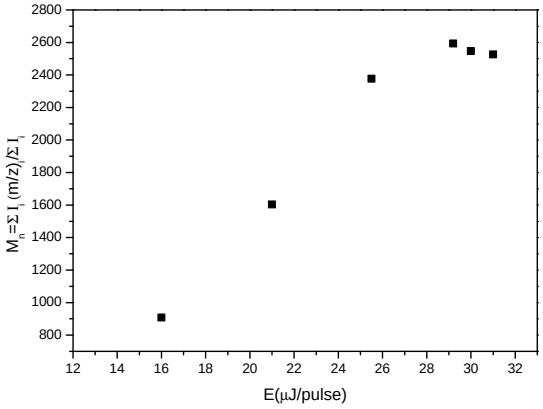

Figure 1.13: Average molecular mass of UG8 as a function of the laser fluence.

1.4 Conclusions

Fragmentation and aggregation studies of polyaromatic hydrocarbons (PAH) under pressure–controlled LDI mass spectrometry have been carried out. With the help of a genetic algorithm specially programmed for high resolution mass spectrometry data analysis, the relative populations of covalent and non-covalent aggregates and the main fragmentation channels can be inferred. This aggregation/fragmentation behavior upon differential pressure condition in the ion source depends on the molecular architecture (aromatic condensation and symmetry of the PAH). Island-like polyaromatics are less fragmentative than archipelago-type ones. Nevertheless, C-H cleavage is efficient in all cases and drives the in-plume covalent polymerization of the PAHs.

Comparative experiments on model PAHs and the UG8 asphalten have demonstrated that no general trends in aggregation/fragmentation under different pressure–controlled conditions can be easily ascribed to a specific molecular architecture because of the complex charged radical stabilization occurring in π-rings containing systems and steric effects in catacondensed and propeller–like molecules. However, although aggregation is enhanced with pressure in general, at least for the models considered here, when it is present in island models, it is shifted to the non–covalent stacking besides the covalent counterpart and more extensively in the bigger PAHs. Moreover, island–like models are more stable under photofragmentative conditions than the archipielago models. This is the case for UG8 asphaltene: it shows a trend to enhance aggregation with pressure as the rest of PAH but a higher stability than archipielago PAH models. Although a more extensive study, employing the genetic algotihm presented in this work, is requiered to give a definite confirmation of the predominant character of the molecular components of this complex mixture, an island like average architecture can be inferred from the commented results.

SUPPLEMENTARY MATERIAL

```
program MSFITTED
c program to fit MALDI spectra and extract populations
implicit double precision (a-h,o-z)
c maa = number of fitting parameters
c ndata = number of data points in exptal data to be fitted
parameter(ndata=400000,mgene=100,maa=10000)
parameter(nnc=100)
common/isotope1/ w0(8,10), w1(8,10), w2(8,10)
common/isotope2/ dm(10,3), wiso(maa,10), weight(maa)
common/basis1/ mc(maa),mn(maa),mo(maa),mh(maa),mcu(maa)
common/basis2/ xmass(maa), xinten(maa), width(maa), fitnes0
common/basis3/nci,ncf,fhi,fhf,noi,nof,nni,nnf,ncui,ncuf
common/basis4/xchi,xchf,ncf0,iTrimers
dimension chrat(nnc), rch(nnc)
dimension yy(mgene), chisqt(mgene), chisqet(mgene)
common/exp/ xexp(ndata), yexp(ndata),
chisqe,xmin,xmax,nndata common/exp2/ fcalib, xmaxx, S0, thresh0
common/gene/ gene(maa,mgene), fitnes(mgene), sumfit, matot
common/gene2/ abest(maa),oldfit(mgene), amax, amin, itest
(mgene) CHARACTER*25 files(0:10)
common/file/ files


   open (unit=2,file='input.inp')
do 5 i=0,5
read(2,*) files(i)
write(*,*) files(i)
5 continue
read(2,*) iFromOld
read(2,*) kgmax, kgavg
read(2,*) xmin, xmax
write(*,*) xmin, xmax
read(2,*) xmaxx
read(2,*) thresh0
read(2,*) fcalib
read(2,*) S0
read(2,*) nci, ncf0
read(2,*) xchi,xchf
read(2,*) noi, nof
read(2,*) nni, nnf
read(2,*) ncui, ncuf
read(2,*) iTrimers
close(2)
* max. number of carbons is limited by the maximum mass to be
analyzed
ncf=min(ncf0,int(xmax/12.0D0))
pi=4.0D0*atan(1.D0)
root2pi= dsqrt(2.D0*pi)
* call the initiation subroutine
* iFromOld=1 if computation follows a previous run


   call START(iFromOld)


   * kgmax is the number of steps in the optimization
do 50 kg= 1, kgmax
```

```
if(mod(kg,kgavg).EQ.0.OR.kg.eq.kgmax) open(unit=
1,file=files(1))


   * calling the routine that performs the "mutations"
call genet


   do 800 ng = 1,mgene
chisqt(ng)= 0.D0
chisqet(ng)= 0.D0
yy(ng)=0.D0
800 continue


   * Each chromosome is a vector with the populations of all the molecular
* species included in the calculation (genes)
* For each chromosome, the mass spectrum is computed. The "fitness" of such
* spectrum is given by its chi square deviation from the experiment
do 100 j=1,nndata
xj=xexp(j)
do 120 ma= 1, matot
xm= xmass(ma)
S= width(ma)
xnorm=1.D0
* Each molecular species enters the computation together with
* its eight most relevant isotopes (due to C and Cu)
do 210 isot=1,8
if(wiso(ma,isot).eq.0) goto 210
xxm= xm + dm(isot,mcu(ma)+1)
if(abs(xxm-xj).LT.4.*S) then
ybasis= xnorm*exp(-(xj-xxm)**2/(2.D0*S**2))
do 110 ng= 1, mgene
yy(ng)= yy(ng) + weight(ma)*wiso(ma,isot)*gene(ma,ng)
ybasis
110 continue
endif
210 continue
120 continue
if(mod(kg,kgavg).EQ.0.OR.kg.eq.kgmax) write(1,*) xj,yexp
(j),yy(1)
* deviation is computed for all the spectra
do 810 ng = 1,mgene
chisqt(ng)= chisqt(ng) + yy(ng)*yy(ng)
chisqet(ng)= chisqet(ng) + (yexp(j)-yy(ng))**2
yy(ng)=0.
810 continue
100 continue
sumfit=0.
do 910 ng = 1,mgene
fitnes(ng)= chisqet(ng)/chisqe
sumfit=sumfit + fitnes(ng)/dfloat(mgene)
if(fitnes(ng).lt.fitnes0) then
fitnes0 = fitnes(ng)
do 150 ma=1,matot
abest(ma) = gene(ma,ng)
150 continue
endif
```

```
910 continue


   * Storing results every given number of steps
if(mod(kg,kgavg).EQ.0.OR.kg.eq.kgmax) then
close(1)
open(unit=3, file= files(2), access='sequential')
write(3,*) kg,' fitnes',fitnes0
write(*,*) kg,' fitnes',fitnes0
close(3)
open(unit=16,file=files(3))
open(unit=17,file=files(4))
write(16,169) mgene, matot
write(17,169) mgene, matot
do 520 ma= 1, matot
write(16,169) mc(ma), mh(ma), mo(ma), mn(ma),
1 mcu(ma), xmass(ma), width(ma), weight(ma)
169 format(5(I8,2x),F10.4,3(2x,1PE12.3))
write(17,1699) mc(ma), mh(ma), xmass(ma), gene(ma,1)
1699 format(2(I8,2x),F10.4,3(2x,1PE12.3))
520 continue
do 560 ng= 1, mgene
do 550 ma= 1, matot
write(16,*) gene(ma,ng)
550 continue
560 continue
close(16)
close(17)


   do 570 ma= 1, matot
if(mh(ma).ne.0) then
chrat(mc(ma))= chrat(mc(ma))+mc(ma)/(1.D0*mh(ma))*gene(ma,1)
rch(mc(ma)) = rch(mc(ma)) + gene(ma,1)
endif
570 continue


   open(unit=15,file=files(5))
do 530 mmc= nci, ncf
if(rch(mmc).ne.0.) then
write(15,*) mmc, rch(mmc), chrat(mmc)/rch(mmc)
rch(mmc)=0.
chrat(mmc)=0.
endif
530 continue
close(15)
endif


   50 continue


   stop
end
********
* INITATION SUBROUTINE
```

```
* initial guess of parameters, based on intensity of experimental
spectrum


   subroutine START(iFromOld)
implicit double precision (a-h,o-z)
c maa = number of fitting parameters
c ndata = number of data points in exptal data to be fitted
parameter(ndata=400000,mgene=100,maa=10000)
parameter(nnc=100)
common/exp/ xexp(ndata), yexp(ndata),
chisqe,xmin,xmax,nndata
common/exp2/ fcalib, xmaxx, S0, thresh0
common/gene/ gene(maa,mgene), fitnes(mgene), sumfit, matot
common/gene2/ abest(maa), oldfit(mgene), amax, amin, itest
(mgene)
common/isotope1/ w0(8,10), w1(8,10), w2(8,10)
common/isotope2/ dm(10,3), wiso(maa,10), weight(maa)
common/basis1/ mc(maa),mn(maa),mo(maa),mh(maa),mcu(maa)
common/basis2/ xmass(maa), xinten(maa), width(maa), fitnes0
common/basis3/nci,ncf,fhi,fhf,noi,nof,nni,nnf,ncui,ncuf
common/basis4/xchi,xchf,ncf0,iTrimers
dimension yy(mgene), chisqt(mgene), chisqet(mgene)
CHARACTER*25 files(0:10)
common/file/ files


   pi=4.0D0*atan(1.D0)
root2pi= dsqrt(2.D0*pi)


   open(unit=10,file=files(0),status='unknown')
ie=0


   ymax=0.
ymax0=0.
do 10 j=1,ndata
* A smoothing of the experimental mass spectrum may be made before optimization read(10,*) x2, y2
if(x2.gt.xmaxx) goto 11
xsmo= x2*fcalib
ysmo= y2
if(ysmo.GT.ymax) ymax=ysmo
if(x2.ge.xmin.AND.x2.le.xmax) then
ie=ie+1
xexp(ie)= xsmo
yexp(ie)= ysmo
if(ysmo.GT.ymax0) ymax0=ysmo
endif
99 format(f8.4,2x,f8.4)
10 continue
11 nndata=ie
close(10)


   open(unit=3, file=files(2))
write(3,*) 'number of points in spectrum=', nndata
```

```
write(*,*) 'number of points in spectrum=', nndata
chisqe=0.
do 12 j=1,nndata
yexp(j)=yexp(j)/ymax
chisqe= chisqe + yexp(j)*yexp(j)
12 continue


  amin=0.D0
amax=1.D-1


  * RELEVANT MASSES (MAIN ISOTOPES)
xH= 1.00783D0
xC12= 12.000D0
xC13= 13.0034D0
xN= 14.00307D0
xO= 15.99492D0
xS1= 31.9721 !100
xS2= 33.9679 !4.5
xCu63= 62.9296D0 !100
xCu65= 64.92779D0 !44.6
* mass increment for main isotopes
dc= - xC12 + xC13
dcu= - xCu63 + xCu65
* if no copper
do 130 kk= 1, 8
dm(kk,1)= (kk-1)*dc
130 continue
* if one copper
dm(1,2)= 0.
dm(2,2)= dc
dm(3,2)= dcu
dm(4,2)= 2.*dc
dm(5,2)= dc + dcu
dm(6,2)= 3.*dc
dm(7,2)= 2.*dc + dcu
dm(8,2)= 3.*dc + dcu
* if two coppers
dm(1,3)= 0.
dm(2,3)= dc
dm(3,3)= dcu
dm(4,3)= 2.*dc
dm(5,3)= dc + dcu
dm(6,3)= 3.*dc
dm(7,3)= 2.*dc + dcu
dm(8,3)= 2.*dcu


  * the following loop checks which species have a mass with signal
above threshold
* to include them in the computation. An initial guess for the
population is
* set from the signal at that the closest mass channel in the
experiment.
threshold=thresh0/ymax
ma=0
do 100 nc= nci, ncf
```

```
do 200 no= noi, nof
do 300 nn= nni, nnf
if(nn+no.gt.3.AND.iTrimers.eq.1) goto 300
do 400 nh= int(nc/xchf), int(nc/xchi)
do 500 ncu= ncui, ncuf
xm0= nc*xC12 + nn*xN + no*xO + nh*xH + ncu*xCu63
if(xm0.lt.xmin) goto 500
xxmod= mod(xm0,202.D0)
if(xxmod.lt.185.AND.xxmod.gt.6) goto 500
if(xm0.lt.210.AND.nc.eq.16) goto 501
if(xm0.lt.415.AND.nc.eq.32) goto 501
if(xm0.lt.620.AND.nc.eq.48) goto 501
if(xm0.lt.825.AND.nc.eq.64) goto 501
goto 500
501 continue
iflag=0
do 600 ie=1,nndata
xe= xexp(ie)
if(xe.gt.xm0) then
if(yexp(ie).gt.threshold) then
iflag=1
ye=yexp(ie)
endif
goto 601
endif
600 continue
601 if(iflag.eq.1) then
ma= ma+1
mc(ma)= nc
mn(ma)= nn
mo(ma)= no
mh(ma)= nh
mcu(ma)= ncu
xmass(ma)= xm0
xinten(ma)=ye
width(ma)= S0*(xm0/300.D0)**0.75
ww=0.
do 700 isot=1,8
ixnc= int(mc(ma)/10.)
xw1= mc(ma)/10. - ixnc
if(mcu(ma).eq.0)
1 wm= xw1*w0(isot,ixnc+1) + (1.-xw1)*w0(isot,ixnc)
if(mcu(ma).eq.1)
2 wm= xw1*w1(isot,ixnc+1) + (1.-xw1)*w1(isot,ixnc)
if(mcu(ma).ge.2)
3 wm= xw1*w2(isot,ixnc+1) + (1.-xw1)*w2(isot,ixnc)
ww = ww + wm
wiso(ma,isot)=wm
700 continue
weight(ma)=(1.D0/ww)*(1.D0/(root2pi*width(ma)))
endif
500 continue
400 continue
300 continue
200 continue
100 continue
matot=ma
write(3,*) 'number of basis functions', matot
```

```
close(3)
write(*,*) 'number of basis functions', matot


   If(iFromOld.eq.1) then
* Continuation from a previous run: genes are read from basis file
open(unit=16,file= files(3))
read(16,*) mgene0, matot0
if(mgene.ne.mgene0.OR.matot0.ne.matot) then
write(*,*) 'inconsistent mgene or matot in basis file'
write(*,*) 'mgene, mgene0:', mgene, mgene0
write(*,*) 'matot, matot0:', matot, matot0
stop
endif
do 520 ma= 1, matot
read(16,*) mc(ma), mh(ma), mo(ma), mn(ma),
1 mcu(ma), xmass(ma), width(ma), weight(ma)
169 format(5(I3,2x),2(F10.4, 2x), 1PE12.3)
520 continue
do 560 ng= 1, mgene
do 550 ma= 1, matot
read(16,*) gene(ma,ng)
550 continue
560 continue
close(16)
else
* In a new computation, the starting genes are guessed from the
* intensities of the mass spectrum
do 530 ng= 1, mgene
do 540 ma= 1, matot
xxg= xinten(ma)/weight(ma)*(1.0-0.5*ng/(1.D0*mgene))
gene(ma,ng)=xxg*200.D0/xmass(ma)*ymax0/ymax
540 continue
530 continue
endif


   * Initial MASS spectra and square deviations (fitness)
do 800 ng = 1,mgene
chisqt(ng)= 0.D0
chisqet(ng)= 0.D0
800 continue
do 900 j=1,nndata
xj=xexp(j)
do 230 ng=1,mgene
yy(ng)=0.
230 continue
do 110 ma= 1, matot
xm= xmass(ma)
S=width(ma)
xnorm=1.D0
do 210 isot=1,8
if(wiso(ma,isot).eq.0) goto 210
xxm= xm + dm(isot,mcu(ma)+1)
if(abs(xxm-xj).LT.4.*S) then
ybasis= xnorm*exp(-(xj-xxm)**2/(2.D0*S**2))
do 220 ng=1,mgene
yy(ng)= yy(ng) + weight(ma)*wiso(ma,isot)*gene(ma,ng)*ybasis
```

```
220 continue
endif
210 continue


   110 continue
do 240 ng=1,mgene
chisqt(ng)= chisqt(ng) + yy(ng)*yy(ng)
chisqet(ng)= chisqet(ng) + (yexp(j)-yy(ng))**2
240 continue
900 continue
sumfit=0.
fitnes0=chisqet(1)/chisqe
mbest=1
do 710 m= 1, mgene
fitnes(m)= chisqet(m)/chisqe
if(fitnes0.gt.fitnes(m)) then
fitnes0=fitnes(m)
mbest=m
endif
sumfit=sumfit + fitnes(m)/dfloat(mgene)
710 continue
open(unit=3, file=files(2), access='sequential')
write(3,*) 'initial fitness', fitnes0
write(*,*) 'initial fitness', fitnes0
if(mbest.ne.1) then
write(3,*) 'initial fitness for gene 1', fitnes(1)
write(3,*) 'initial fitness for gene',mbest,fitnes(mbest)
endif
close(3)
*********************************************************
*ISOTOPIC ratios
* 0, dc, 2dc, 3dc, ..., 7dc
DATA w0/1.D0,0.11D0,0.,0.,0.,0.,0.,0.,
1 1.D0,0.22D0,0.02D0,0.,0.,0.,0.,0.,
2 1.D0,0.32D0,0.05D0,0.,0.,0.,0.,0.,
3 1.D0,0.43D0,0.09D0,0.01D0,0.,0.,0.,0.,
4 1.D0,0.54D0,0.14D0,0.03D0,0.,0.,0.,0.,
5 1.D0,0.65D0,0.21D0,0.04D0,0.,0.,0.,0.,
6 1.D0,0.76D0,0.28D0,0.07D0,0.01D0,0.,0.,0.,
7 1.D0,0.86D0,0.37D0,0.10D0,0.02D0,0.,0.,0.,
8 1.D0,0.97D0,0.47D0,0.15D0,0.04D0,0.,0.,0.,
9 0.92D0,1.D0,0.54D0,0.19D0,0.05D0,0.01D0,0.,0./


   DATA w1/1.D0,0.11D0,0.45D0,0., 0.05D0,0., 0., 0.,
1 1.D0,0.22D0,0.45D0,0.02D0,0.10D0,0., 0.01D0,0.,
2 1.D0,0.32D0,0.45D0,0.05D0,0.15D0,0., 0.02D0,0.,
3 1.D0,0.43D0,0.45D0,0.09D0,0.19D0,0.01D0,0.04D0,0.,
4 1.D0,0.54D0,0.45D0,0.14D0,0.24D0,0.03D0,0.06D0,0.01D0,
5 1.D0,0.65D0,0.45D0,0.21D0,0.29D0,0.04D0,0.09D0,0.02D0,
6 1.D0,0.76D0,0.45D0,0.28D0,0.34D0,0.07D0,0.13D0,0.03D0,
7 1.D0,0.86D0,0.45D0,0.37D0,0.39D0,0.10D0,0.17D0,0.05D0,
8 1.D0,0.97D0,0.45D0,0.47D0,0.43D0,0.15D0,0.21D0,0.07D0,
9 0.92D0,1.D0,0.41D0,0.54D0,0.45D0,0.19D0,0.23D0,0.08D0/


   DATA w2/1.D0,0.11D0,0.89D0,0., 0.10D0,0., 0.20D0,0.02D0,
```

```
1 1.D0,0.22D0,0.89D0,0.02D0,0.19D0,0., 0.20D0,0.04D0,
2 1.D0,0.32D0,0.89D0,0.05D0,0.05D0,0., 0.20D0,0.06D0,
3 1.D0,0.43D0,0.89D0,0.09D0,0.39D0,0.01D0,0.20D0,0.09D0,
4 1.D0,0.54D0,0.89D0,0.14D0,0.14D0,0.03D0,0.20D0,0.11D0,
5 1.D0,0.65D0,0.89D0,0.21D0,0.21D0,0.04D0,0.20D0,0.13D0,
6 1.D0,0.76D0,0.89D0,0.28D0,0.28D0,0.07D0,0.20D0,0.15D0,
7 1.D0,0.86D0,0.89D0,0.37D0,0.37D0,0.10D0,0.20D0,0.17D0,
8 1.D0,0.97D0,0.89D0,0.47D0,0.47D0,0.15D0,0.20D0,0.19D0,
9 0.92D0,1.D0,0.82D0,0.54D0,0.54D0,0.19D0,0.18D0,0.20D0/


   RETURN
end
c ------------------------------------------------------------
subroutine genet
c ------------------------------------------------------------
c Genetic Algorithm


   implicit double precision (a-h,o-z)
c mgene is the number of genes, maa is the number of fitting coeffs (intensities),
c nran is the number of random mutations (set to  5parameter(nran=50,mgene=100,maa=10000)
dimension list(mgene),oldgene(maa,mgene),ftemp(mgene)
common/gene/ gene(maa,mgene), fitnes(mgene), sumfit, matot
common/gene2/ abest(maa), oldfit(mgene), amax, amin, itest(mgene)


   fact = 1.0d0


   do 5 k=1,mgene
list(k) = k
5 continue


   call hpsort(mgene,fitnes,list)


   do 10 k=1,mgene
itest(k) = 1
oldfit(k) = fitnes(k)
ftemp(k) = fitnes(k)
do 20 i=1,matot
oldgene(i,k) = gene(i,list(k))
20 continue
10 continue


   num = 1
do 30 k=1,mgene
if (fitnes(k) .lt. sumfit) then
oldfit(num) = fitnes(k)
do 40 i=1,matot
oldgene(i,num) = gene(i,list(k))
40 continue
num = num+1
ftemp(k) = fitnes(k)-sumfit
```

```
if (num .gt. mgene) goto 230
endif
30 continue
200 do 50 k=1,mgene
val = sumfit*ran1(idum)
if (ftemp(k) .lt. val) then
oldfit(num) = fitnes(k)
do 60 i=1,matot
oldgene(i,num) = gene(i,list(k))
60 continue
num = num+1
ftemp(k) = 0.0d0
endif
if (num .gt. mgene) goto 230
50 continue
if (num .lt. mgene+1) goto 200


   230 do 70 k=1,mgene,2
if (oldfit(k) .eq. oldfit(k+1)) goto 70
ipos = dint(dble(matot)*ran1(idum))+1
do 80 i=ipos,matot
hold = oldgene(i,k)
oldgene(i,k) = oldgene(i,k+1)
oldgene(i,k+1) = hold
80 continue
itest(k) = 0
itest(k+1) = 0
70 continue


   if(nran.ne.0) then
do 90 m=1,nran
imut = dint(dble(matot)*ran1(idum))+1
kmut = dint(dble(mgene)*ran1(idum))+1
er = 2.0d0*ran1(idum)-1.0d0
er = abest(imut)+er*fact
if (er .lt. amin) goto 90
if (er .gt. amax) goto 90
oldgene(imut,kmut) = er
itest(kmut) = 0
90 continue
do 95 m=1,nran
imut = dint(dble(matot)*ran1(idum))+1
kmut = dint(dble(mgene)*ran1(idum))+1
itest(kmut) = 0
er = (amax-amin)*ran1(idum)+amin
oldgene(imut,kmut) = er
95 continue
endif
do 100 k=1,mgene
do 110 i=1,matot
gene(i,k) = oldgene(i,k)
110 continue
100 continue


   return
```

```
end


  c ---------------------------------
subroutine hpsort(n,ra,list)
c ---------------------------------
implicit double precision (a-h,o-z)
dimension list(n),ra(n)


  c Heapsort routine


  if (n .lt. 2) return
l = n/2+1
ir = n
10 continue
if (l .gt. 1) then
l = l-1
rra = ra(l)
lrr = list(l)
else
rra = ra(ir)
lrr = list(ir)
ra(ir) = ra(1)
list(ir) = list(1)
ir = ir-1
if (ir .eq. 1) then
ra(1) = rra
list(1) = lrr
return
endif
endif
i = l
j = l+l
20 if (j .le. ir) then
if (j .lt. ir) then
if (ra(j) .lt. ra(j+1)) j = j+1
endif
if (rra .lt. ra(j)) then
ra(i) = ra(j)
list(i) = list(j)
i = j
j = j+j
else
j = ir+1
endif
goto 20
endif
ra(i) = rra
list(i) = lrr
goto 10


  end
c ---------------------------------
double precision function ran1(idum)
```

```
c ------------------------------
c Random number generator


   implicit double precision (a-h,o-z)
integer idum,ia,im,iq,ir,ntab,ndiv
parameter (ia=16807,im=2147483647,iq=127773,ir=2836,
*ntab=32,ndiv=1+(im-1)/ntab)
parameter (eps=1.2d-7,rnmx=1.0d0-eps)
integer j,k,iv(ntab),iy
save iv,iy
data iv /ntab*0/, iy /0/
am=1.0d0/dble(im)


   if ((idum.le.0) .or. (iy.eq.0)) then
idum = max0(-idum,1)
do 11 j=ntab+8,1,-1
k = idum/iq
idum = ia*(idum-k*iq)-ir*k
if (idum .lt. 0) idum = idum+im
if (j .le. ntab) iv(j) = idum
11 continue
iy=iv(1)
endif
k = idum/iq
idum = ia*(idum-k*iq)-ir*k
if (idum .lt. 0) idum = idum+im
j = 1+iy/ndiv
iy = iv(j)
iv(j) = idum
ran1 = dmin1(am*dble(iy),rnmx)


   return
end
```

Table 1.1: Relative population of the main species found within the monomer (m) and dimer (d) m/z ranges as extracter from the genetic algorithm calculations island–like compounds. A null population is considered when it is smaller tan 10 %

Nominal m/z	Stoichiometry	relative population	
		High pressure	Low pressure
M = Pyrene $C_{16}H_{10}$			
200 (m)	M-H_2	0.00	1.00
201 (m)	M-H	0.00	0.42
202 (m)	M	1.00	0.76
400 (d)	(M_2)-H_4	0.95	1.00
401 (d)	(M_2)-H_3	0.48	0.20
402 (d)	(M_2)-H_2	0.86	0.13
403 (d)	(M_2)-H	1.00	0.00
404 (d)	(M_2)	0.35	0.00
M = Benzo[ghi]perylene $C_{22}H_{12}$			
274 (m)	M-H_2	0.00	0.85
275 (m)	M-H	0.00	0.24
276 (m)	M	1.00	1.00
549 (d)	M_2-H_3	0.55	0.00
550 (d)	M_2-H_2	0.60	0.00
551 (d)	M_2-H	1.00	0.00
552 (d)	M_2	0.55	0.00
M = Benzo[a]pyrene $C_{20}H_{12}$			
250 (m)	M-H_2	0.00	0.90
251 (m)	M-H	0.00	0.19
252 (m)	M	1.00	1.00
M = Perylene $C_{20}H_{12}$			
250 (m)	M-H_2	0.00	1.00
251 (m)	M-H	0.00	0.14
252 (m)	M	1.00	0.50
M = Coronene $C_{24}H_{12}$			
520 (m)	M-H_2	0.00	0.91
522 (m)	M	1.00	1.00
594 (d)	(M_2)-H_6	0.12	0.18
595 (d)	(M_2)-H_5	0.26	0.00
596 (d)	(M_2)-H_4	1.00	1.00
597 (d)	(M_2)-H_3	0.48	0.58
598 (d)	(M_2)-H_2	0.70	0.19
599 (d)	(M_2)-H	0.65	0.00
600 (d)	(M_2)	0.53	0.00
M = Hexabenzocoronene $C_{42}H_{18}$			
520 (m)	M-H_2	0.00	0.64
521 (m)	M-H	0.44	0.00
522 (m)	M	1.00	1.00
1036 (d)	(M_2)-H_8	0.15	0.00
1037 (d)	(M_2)-H_7	0.83	0.38
1038 (d)	(M_2)-H_6	0.21	1.00
1039 (d)	(M_2)-H_5	0.17	0.13
1040 (d)	(M_2)-H_4	0.00	0.00
1041 (d)	(M_2)-H_3	1.00	0.00
1042 (d)	(M_2)-H_2	0.42	0.44
1043 (d)	(M_2)-H	0.72	0.00
1044 (d)	(M_2)	0.13	0.00

Table 1.2: Relative population of the main species found within the monomer (m) and dimer (d) m/z ranges as extracter from the genetic algorithm calculations for archipielago–like compounds. A null population is considered when it is smaller tan 10 %

Nominal m/z	Stoichiometry	relative population	
		High pressure	Low pressure
M = DPBVi $C_{40}H_{30}$			
509 (m)	M-H	0.31	0.70
510 (m)	M	1.00	1.00
M = DNA $C_{34}H_{22}$			
426 (m)	M-H_4	0.00	0.40
427 (m)	M-H_3	0.00	1.00
428 (m)	M-H_2	0.00	0.46
429 (m)	M-H	0.00	0.36
430 (m)	M	1.00	0.00
M = pBye $C_{38}H_{22}$			
472 (m)	M-H_6	0.24	0.58
473 (m)	M-H_5	0.24	0.13
474 (m)	M-H_4	1.00	1.00
475 (m)	M-H_3	0.76	0.49
476 (m)	M-H_2	0.37	0.22
477 (m)	M-H	0.58	0.26
478 (m)	M	0.52	0.00

Bibliography

[1] M. R. Gray, R. R. Tykwinski, J. M. Stryker, X. Tan. Energy and Fuels. 25 (2011) 3125.

[2] A. N. Krutchinsky, A. V. Loboda, V, L. Spicer, R. Dworschak, W. Ens, K. G. Standing. Rapid Commun. Mass Spectrom. 12 (1998) 508.

[3] B. Martínez-Haya, A. R. Hortal, P. Hurtado, M. D. Lobato, J. M. Pedrosa. J. Mass Spectrom. 42 (2007) 701.

[4] A. R. Hortal, P. Hurtado, B. Martínez-Haya, O. C. Mullins. Energy and Fuels. 21 (2007) 2863.

[5] P. Hurtado, F. Gámez, B. Martínez-Haya, Energy and Fuels, 24 (2010) 6067.

[6] S. Kim, R. P. Rodgers, G. T. Blakney, C. L. Hendrickson, A. G. Marshall. J. Am. Soc. Mass. Spectrom. 20 (2009) 263.

[7] S.G. Lias, "Ionization Energy Evaluation" in NIST Chemistry WebBook, NIST Standard Reference Database Number 69, Eds. P.J. Linstrom and W.G. Mallard, National Institute of Standards and Technology, Gaithersburg MD, 20899, http://webbook.nist.gov.

[8] J. Soltwisch, J. Souady, S. Berkenkamp, K. Dreisewerd. Anal. Chem. 81 (2009) 2921.

[9] A. Cristadoro, H. J. Räder, K. Müllen. Rapid Commun. Mass Spectrom. 21 (2007) 2621.

[10] P. Hurtado. PhD Thesis. Universidad Pablo de Olavide. 2012.

Chapter 2

UV-vis-NIR laser desorption/ionization of synthetic polymers assisted by gold nanospheres, nanorods and nanostars

The laser desorption/ionization (LDI) assisted by gold nanospheres, nanorods and nanostars has been investigated. Laser fluence thresholds for the appearance of cationized adducts of a polydispersed polyether standard (polyethylenglycol PEG600) have been determined at the near ultraviolet–visible–near infrared wavelengths delivered by a Nd:YAG laser (266, 355, 532, 1064 nm). The results demonstrate the efficiency of surface plasmon excitation to assist laser desorption/ionizaton at laser wavelengths extending to the visible and near infrared, with advantages with respect to conventional LDI techniques using ultraviolet wavelengths. A close correlation is found between the optical absorbance of the nanoparticles and the LDI thresholds, although for the nanospheres plasmonic excitation in the visible appears to be more efficient than non–plasmonic excitation at shorter UV wavelengths. The recorded molecular weight distributions for the PEG600 standard show that the LDI process tends to be less efficient for the heavier components of the polymer mixture, presumably as a consequence of their stronger bonding to the nanoparticle substrate. The role of the coating agent of the nanoparticles in the observed LDI behavior is discussed.

2.1 Introduction

The use of metal nanoparticles as substrates for laser desorption/ionization (LDI) is currently attracting renewed attention. Even though the concept was demonstrated more than two decades ago [1, 2, 3, 4], it has been within the last few years that the consolidation of nanoparticle synthesis techniques has catalyzed systematic studies in this field [5, 6, 7, 8, 9, 10, 11, 12, 13, 14, 15, 16, 17, 18, 19, 20]. There is a growing interest in the application of plasmonic LDI, in particular, to organic and biochemical analysis and in the development of novel molecular sensors [6, 15, 21, 22, 23].

As mentioned in the introduction, LDI techniques based on nanostructures share the ability to overcome practical limitations of more conventional matrix–assisted LDI employing organic matrices (MALDI). On one hand, they avoid the common problems related to the physicochemical compatibility between matrix and analytes, which in practice makes the choice of the adequate organic MALDI matrix largely a trial-and-error procedure [24]. Moreover, one fundamental advantage of plasmonic nanoparticle substrates with respect to semiconducting materials relies on the tunability of the plasmon excitation, *e.g.* by controlling the size and geometry of the nanoparticles [25, 26, 27, 28, 29]. For LDI applications, this unique feature paves the ground for the use of a single material for broadband laser irradiation. Laser excitation in the visible and longer wavelengths is often advantageous for the detection of labile UV–absorbing species. Furthermore, it allows for the application of a range of alternative laser sources. Plasmon excitation yields large electromagnetic field and charge interactions in the vicinity of the particle surface. The subsequent energy and charge transfer processes involved in the desorption/ionization mechanisms assisted by the plasmon constitute exciting topics of fundamental research.

The present chapter intends to provide a systematic study of the laser wavelength dependence of the LDI of model synthetic polymers assisted by gold nanoparticles three different geometries (spheres, rods, stars). The four wavelengths (UV-vis-NIR) delivered by a Nd:YAG laser are employed to probe the broadband LDI behavior of the three materials. Wavelength dependent studies are relatively scarce, as most previous experiments have employed the 337 nm wavelength (nitrogen laser) of the commercial MALDI equipments. Chen and coworkers compared LDI at 355 nm and 532 nm on gold nanorods [10, 11], and LDI at 532 nm and 1064 nm on gold ablated films [17]. They concluded that the plasmonic resonant 532 nm wavelength was most efficient. Spencer and coworkers employed a tunable dye laser to scan the visible plasmonic band of gold nanospheres suspended in aerosols, and found negligible LDI signal in the region of weak absorbance (wavelengths longer than 600 nm) [12]. In contrast, Schürenberg and coworkers reported a weak dependence on laser wavelength in LDI processes assisted by different conducting nanoparticles dispersed in glycerol [4].

We have undertaken an extension of the above mentioned Au–assisted LDI studies, with the aim to provide further information about the dominant processes involved.

2.2 Nanoparticle synthesis and characterization

Gold nanospheres, nanorods and nanostars were synthesized with the procedures outlined below. All chemicals were commercial reagent grade and used as received. Standard polydispersed polyethylene glycol (PEG600) was purchased from Fluka; Hydrogen tetrachloroaurate(III) hydrate from Alfa Aesar; tri–sodium citrate 2–hydrate, silver nitrate and L(+)–ascorbic acid from Panreac; polyvinylpyrrolidone (PVP, average mol. weight ~ 10000), cetyltrimethylammonium bromide, sodium sulfide and N,N-dimethylformamide (DMF) from Sigma–Aldrich. Water was purified using a Milli-Q reagent grade water system from Millipore.

Transmission Electron Microscopy (TEM) images of the nanoparticles were taken using a Philips CM200 microscope. The TEM samples were prepared by air drying a drop of an aqueous solution of nanoparticles on a copper grid coated with a carbon film. Illustrative TEM images are shown in Fig. 2.1. UV–vis–NIR absorption spectra of the nanoparticles were recorded with an optical fiber CCD spectrometer (DH2000, Ocean optics). The optical absorbances were measured both from an aqueous dispersion and from thin films deposited on quartz. Thin films were produced by precipitation of nanoparticle and nanoparticle/PEG solutions on a quartz plate after evaporation of the solvent in air. Fig. 2.2 shows that the absorption spectra of the three types of the nanoparticles feature distinct plasmonic bands and cover a broad UV–vis–NIR range.

Spherical citrate–capped gold nanoparticles were synthesized according to a established protocol [30]. Briefly, an aqueous solution of tri–sodium citrate (34 mM, 3 mL) was added, all at once under vigorous stirring, to an aqueous solution of $HAuCl_4$ (0.259 mM, 200 mL) previously heated to 90^oC. The reaction mixture was maintained at 90^oC under stirring for 10–15 min, until ruby–red color development was complete. The gold nanospheres employed in the present study had an average diameter of 20 nm (Fig. 2.1, top). The gold nanosphere working solution had an optical density of 0.95 at the 532 nm of the Nd:YAG laser and of 0.85 at

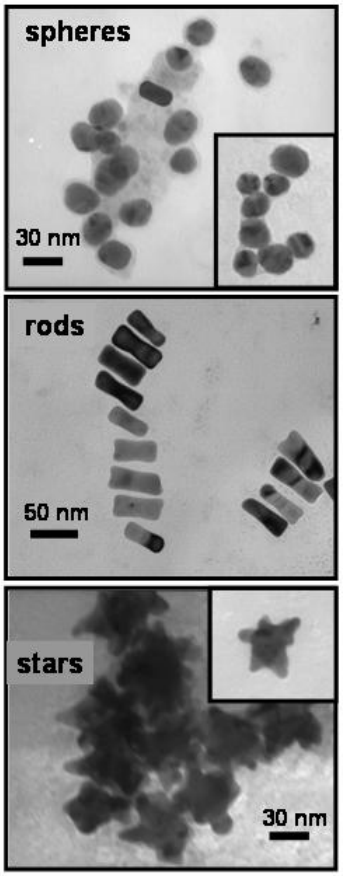

Figure 2.1: Transmission electron microscopy (TEM) images of the three types of gold nanoparticles employed in the present LDI investigation. The nanorods (middle) have a length of 50 nm and an average diameter of 18 nm. The nanospheres (top) have a 20 nm average diameter and are protected with citrate coating. The nanostars (bottom) have average diameters of 35 nm (core) and 50 nm (whole particle), and are protected with a polyvinylpyrrolidone polymer of average molecular weight ~ 10000.

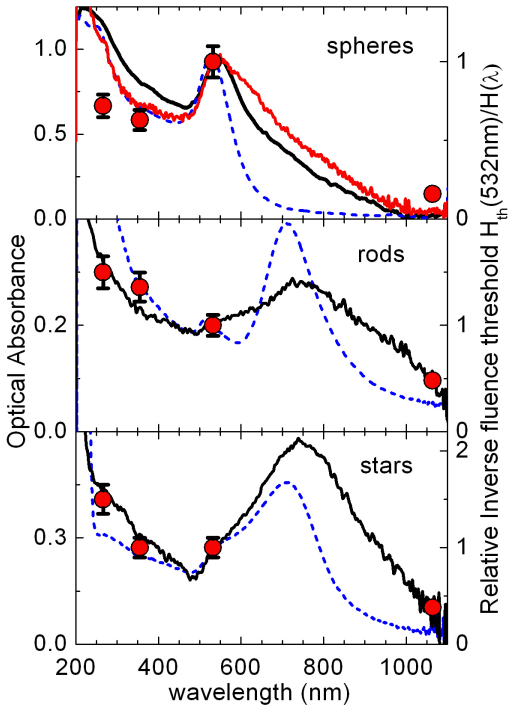

Figure 2.2: Optical absorbance of the gold nanospheres (top), nanorods (middle) and nanostars (bottom) in aqueous solution (dotted lines) and in a thin film of each of the nanoparticles deposited on quartz (solid lines). The top panel also includes the spectrum measured for a film of nanospheres precipitated with PEG (dot–dashed curve). The thin film spectra have been arbitrarily scaled to match the value of the solution spectra at 532 nm (left–hand y–axis). The plasmon bands account for the absorbance above 400 nm, extending to the near–infrared. Relative *inverse* LDI laser fluence thresholds, $H_{th}(532\,\mathrm{nm})/H_{th}(\lambda)$, are represented (circles with error bars, referred to the right–hand y–axis) to illustrate the degree of correlation between the fluence thresholds and the optical densities at the different wavelengths.

506 nm. Considering the absolute extinction coefficients reported in ref. [31], the concentration of the nanospheres in our working solution is estimated to be ≈ 1 nM. This value is consistent with the total reduction of the Au employed in the synthesis.

Gold nanorods were prepared with the procedure described by Sau and Murphy [32]. Aqueous solutions of $HAuCl_4$ (10 mM, 250 μL) and CTAB (100 mM, 7.5 mL) were gently mixed. When the solution turned light brown–yellow in color, an ice–cold aqueous solution of $NaBH_4$ (10 mM, 600 μL) was added and gently mixed for 2 min. The resulting "seed solution" was stored at 25^{o}C. In a second step, $HAuCl_4$ (10 mM, 200 μL), $AgNO_3$ (10 mM, 30 μL), ascorbic acid (100 mM, 32 μL) and 10 μL of the seed solution were added, in the order indicated, to an aqueous solution of CTAB (100 mM, 4.75 mL). The reaction mixture was gently mixed and left undisturbed for 20 min. Blue color development indicated the formation of the nanorods, which were finally stabilized by addition of sodium sulfide (1.25 mM, 7.35 mL; molar ratio of sulfur to total metal content of 4:1) [33]. The TEM images show that the gold nanorods have a slight dumbbell shape, with average length of 50 nm, maximum diameter of 18 nm and a smaller central diameter of 16 nm (Fig. 2.1, middle). The gold nanorod working solution had an optical density of 0.20 at 532 nm. We are not aware of absolute extinction coefficients for gold nanorods, but they can be expected to be significantly greater in the visible region than for the nanospheres [25]. Similar considerations hold for the nanostars described below [34]. In agreement with this expectation, the assumption of complete gold reduction in the synthesis leads to concentration of the nanorods in the working solution an estimation of 0.1 nM (*i.e.*, one order of magnitude smaller than the one estimated above for the nanospheres).

Gold nanostars were prepared in a three step procedure [35], simpler in practice than that of the nanorods. A "seed solution" was prepared by adding an aqueous solution of tri–sodium citrate (3.4 mM, 7.5 mL) to a boiling aqueous solution of $HAuCl_4$ (0.42 mM, 30 mL) under vigorous stirring. Boiling was continued for 11 min and stirring for additional 15 min. A "growth solution" was prepared by adding aqueous solution of $HAuCl_4$ (50 mM, 84 μL) to a solution of PVP in DMF (10 mM, 15 mL) under vigorous stirring at room temperature. Finally, 400 μL of seed solution were injected under vigorous stirring to the growth solution and the reaction mixture was stirred for 10–15 min, until blue color development was complete. Nanostars were recovered by centrifugation, washed with Milli–Q water and resuspended in 10 mL Milli–Q water. The size of the gold nanostars achieved for this investigation can be described by an average internal diameter of 35 nm (central core) and an external diameter (including the rod–like protuberances) of 50 nm (Fig. 2.1, bottom). The gold nanostar working solution had an optical density of 0.27 at 532 nm. An estimated concentration of nanostars of roughly 0.08 nM results from assuming the total reduction of the gold employed in the synthesis.

2.3 Laser desorption/ionization mass spectrometry and LDI thresholds measurements

A polydispersed polyethylene glycol standard (PEG600) was chosen for our systematic LDI investigation. The thermochemical stability and appreciable alkali cation affinity of the ether moieties make them particularly suitable for laser desortion/ionization studies [36, 37, 18]. PEG is easily cationized by the ubiquitous Na^+ and K^+ impurities. We added a small amount of Na^+ salt to our samples in order to maintain a constant concentration of cationizing agent in the different substrates. In the present context, PEG cationization is advantageous as it provides a simpler framework in comparison to chemical ionization via proton transfer. Proton sources from the metal nanoparticle substrates are uncertain, unless specific acidic groups or buffers are incorporated to the surface [13, 18]. The LDI PEG–Na^+ ion yields can then be expected to resemble more closely desorption efficiencies, decoupled from complex secondary ionization processes.

Sample solutions for the LDI measurements were prepared by adding 100 μL aliquots of a methanol:water (0.1:1) solution 1 mM in PEG600 and 0.1 mM in the cationizing agent (NaI or NaCl), to 100 μL of the aqueous dispersions of the gold nanoparticles described above. The LDI samples were then produced with the conventional dried–droplet method: 10 μL of sample solution were spotted all at once on the stainless–steel sample plate, covering its *ca.* 20 mm^2 area, and allowed to dry in air. NaI was chosen as cationizing because of its relatively small lattice energy (705 kJ mol^{-1}), which ensures a large yield of free Na^+ ions in the desorbing plume to assist PEG cationization. The use of NaCl yielded similar relative LDI thresholds, but the recorded signals were overall weaker due to the comparably greater lattice energy of the salt (790 kJ mol^{-1}) [36]. The use of NaI also served to test the robustness of the substrates against the addition of I^-. Previous studies have shown that the presence of iodate enhances aggregation of the nanoparticles and deteriorates the LDI signal [**?**, **?**]. In our experiments, such effects were only noticeable when the sample concentration of NaI was increased roughly fivefold with respect to the one employed for the bulk of the present measurements.

LDI mass spectrometry measurements were performed in a reflectron time–of–flight mass spectrometer

(RETOF–MS) from Jordan TOF Products Inc. (Grass Valley, CA, USA). The apparatus has been employed in a number of previous LDI investigations of our group (*e.g.*, see ref. [36]) and is described here only briefly. The sample plate is mounted on the repeller plate of the ion source. For the present measurements, the positive analyte ions were accelerated with a total voltage drop of 4.2 kV, applied with a 1 μs delay with respect to the laser pulse. The reflectron was operated with a 4.5 kV voltage rise to reflect the ions toward the multichannel–plate detector. Under these operating conditions, the mass resolution of the LDI spectra was $M/\Delta M \approx 2000$ for the molecular weights of interest.

The laser radiation employed corresponded to the fundamental and harmonics (1064 nm, 532 nm, 355 nm, 266 nm) of a Nd:YAG laser (Minilite II, Continuum Inc.). All the experiments were performed with the laser beam focused on the sample plate, with lenses of 25 cm (UV–vis) or 20 cm (NIR) nominal focal length, providing focal waists of *ca.* 100 μm and 80 μm, respectively. The precise focal length for each wavelength was determined by the size and intensity of the focal spot, as measured on a burn paper sheet mounted on a travelling stage. Laser pulses with 5 ns duration and energies ranging 1–100 μJ were applied. Pulse energies throughout the text refer to values on the sample, *i.e.*, after calibration to account for losses due to optical components and windows. The mass spectra were averaged over 128 laser shots, at 10 shot–per–second operation.

The LDI thresholds were conveniently defined as the laser fluence (energy per unit area), $H_{th}(\lambda)$, required to record mass spectra with the major PEG–Na^+ adduct peaks having a signal–to–noise ratio of $S/N \approx 3$. The experiments were repeated on up to five independent samples of similar composition, taking different orders for the application of each of the four Nd:YAG wavelengths. Sample–to–sample variation of the *relative* values of the thresholds observed at the four wavelengths on each sample was within 15 % (range between the lowest and the highest thresholds measured for the set of five samples, relative to the average value). On the other hand, sample–to–sample variations in the *absolute* threshold energies determined in the experiments were within 30 %. This appreciable experimental deviation can be attributed to the heterogeneous precipitation of the sample leading to local "sweet spots" of greater LDI efficiency. In order to minimize this latter sweet–spot effect, the sample plate was continuously rotated during the data collection. Sample preparation with a spin coating methodology did not improve the reproducibility.

2.4 Results

The first step of the investigation was the characterization of the UV–vis–NIR absorption spectra of the nanoparticles, both in solution and in thin films. Such spectra are shown in Fig. 2.2 where, for direct comparison, the curves for the films have been arbitrarily scaled as to match the absorbance of the aqueous dispersions at 532 nm. On one hand, the nanoparticles display a strong absorbance at short UV wavelengths (< 400 nm) associated to excitations of valence electrons to the conduction band. On the other hand, the plasmon excitation bands cover a broad region of longer wavelengths in the visible and near–infrared. Plasmon absorbance in the gold nanospheres leads to a characteristic band centered in the range 500–600 nm (*e.g.*, see ref. [12]). The broader spectra of the nanorods and the nanostars are qualitatively similar to each other. Both spectra feature a shoulder located at a similar visible wavelength as the nanosphere plasmon, associated with the excitation of transversal plasmons. In addition, the stronger longitudinal plasmon leads to a prominent absorption band centered around 700–800 nm and extending to the near infrared. The observation of the transversal/longitudinal plasmonic bands is characteristic of the gold nanorods [25, 29]. In the nanostars these bands result from the rod–like shape of the protuberances of the star geometry [40, 34, 29].

Fig. 2.2 also shows that the plasmon bands of the solid films are systematically broadened toward the infrared with respect to those of the corresponding particle solutions. This feature can be attributed to distortion of the plasmonic absorption due to the interaction of the nanoparticles with each other upon evaporation of the solvent [29]. The coprecipitation of the nanospheres with the PEG analyte induces only a slight additional broadening of the spectrum. We did not succeed in measuring similar nanorod/PEG and nanostar/PEG film spectra due to the smaller concentration of the nanoparticles. Nevertheless, broadening effects due to PEG for the nanorods and nanostars can be expected to be of similar or lesser importance than for the nanospheres due to their more bulky coating agents.

The broadband absorbance displayed by the nanoparticles is *a priori* appropriate for LDI applications with UV–visible–NIR laser wavelengths. Table 2.1 lists the absolute fluence thresholds, $H_{th}(\lambda)$, measured in the LDI of PEG600 assisted by each of the nanoparticles at the four Nd:YAG laser wavelengths presently considered. As can be observed, under our experimental conditions, fluences within 0.7–8.0 kJ m^{-2} (pulse energies within 6–40 μJ) were required for threshold detection (signal/noise $S/N = 3$). Fig. 2.2 illustrates the correlation found between the optical absorption of the nanoparticles and the *relative* laser fluence thresholds for

the LDI production of the PEG600–Na^+ adducts at the four wavelengths explored. Smaller thresholds are consistently observed at the wavelengths of greater optical absorbance of the nanoparticles. Hence, in order to provide a clearer representation of such correlation, Fig. 2.2 presents an overlay of the absorption spectra with the *inverse* of each relative threshold fluence, normalized with respect to 532 nm. Furthermore, the axis corresponding to the inverse threshold and absorbance graphs are arbitrarily scaled so that the two magnitudes overlap visually at 532 nm in each case. Such scaling provides an intuitive illustration of the remarkable degree of correlation found between the relative values of inverse thresholds, $H_{th}(532\,\mathrm{nm})/H_{th}(\lambda)$, and the relative absorbances $A(\lambda)/A(532\,\mathrm{nm})$, at the four wavelengths scoped in our study.

We discuss in the first place the results obtained for the nanospheres. Previous studies with gold nanospheres have primarily employed the 337 nm wavelength of the N_2 laser, most common in commercial MALDI equipments, hence exciting the nanoparticles outside the plasmon band. Our experiments yield a particularly low threshold ($0.64\,\mathrm{kJ\,m^{-2}}$) at 532 nm, which lies on the maximum of the differentiated plasmonic band. At the two shorter UV wavelengths 266 nm and 355 nm, both inside the valence electron band (*i.e.*, negligible plasmonic excitation), the threshold increases appreciably, by *ca.* 40–60 % (to 0.89 and $1.02\,\mathrm{kJ\,m^{-2}}$, respectively). This finding is remarkable, since the absorbance measured for the substrate is for instance significantly greater at 266 nm with respect to 532 nm. Plasmonic excitation seems therefore to be more efficient than valence electron excitation in promoting the LDI process. Finally, at 1064 nm the observation of the PEG polymers required a comparably high threshold fluence of $\sim 4\,\mathrm{kJ\,m^{-2}}$. Nevertheless, the substrate produces good quality LDI mass spectra at 1064 nm (see below). The only previous systematic wavelength dependence study of the LDI response of gold nanospheres was performed under quite different experimental conditions [**?**]. It employed an aerosol suspension of the nanoparticles, and involved laser energies two orders of magnitude higher than the present ones. In the aerosol experiments, no LDI signal was detected at any wavelength for nanospheres with diameters of tens of nanometers. The measurements with 5 nm nanospheres led to a close correlation of the LDI yield with the plasmon absorbance spectrum. The present results corroborate the efficiency of plasmon excitation in promoting LDI reported in the aerosol experiments, extend the range of applicability of the technique to the near infrared, and show that the more conventional LDI conditions presently applied allow for a broader range of nanoparticle sizes than the aerosol approach.

For the gold nanorods and nanostars, a remarkably close correlation is found between the relative laser fluence thresholds and the optical absorbances at the four wavelengths scoped in our study (see Fig. 2.2). Hence, valence electron excitation in the UV seems to have a similar LDI efficiency as plasmon excitation in the visible and NIR (relative to absorbance). Table **??** shows that $[A(\lambda)/A(532nm)] \cdot [H_{th}(532nm)/H_{th}(\lambda)]^{-1} = 1.0 \pm 0.2$. Hence, the product laser fluence×absorbance at the LDI threshold remains roughly constant at the four wavelengths for these two types of nanoparticles. This behavior indicates that, at least under the present working conditions, the LDI mechanism induced by the nanorods and nanostars is likely to be of photothermal character, not crucially dependent on the type of electronic excitation (valence electron or plasmonic) induced on the nanoparticles. The local heating of the nanoparticles and their environment induced by the laser is directly proportional to the energy absorbed in each laser pulse: $\Delta T = H \cdot (\rho d C_P)^{-1}$, where ΔT is the increase of temperature, H the energy absorbed per unit area, ρ and C_P the density and thermal capacity of the material, and d the diffusion length of the heat in the time scale of the laser pulse duration [**?**, **?**]. Since the factor $(\rho d C_P)^{-1}$ remains constant for a given LDI sample, the heating of the substrate is proportional to the energy absorbed. It follows that, at the LDI thresholds relevant to the present study, the heating fulfills $(\Delta T)_{th} \propto A(\lambda) \cdot H_{th}(\lambda)$, which for nanorods and nanostars is found in our study to be roughly constant at the four wavelengths investigated. This latter result indicates that the threshold is reached when a similar degree of heating has been induced on the substrate, independently of the wavelength applied.

The thermal behavior of the nanorods and nanostars is likely to be a consequence of the bulky polymers employed for their stabilization. It seems plausible that the protective agents prevent the direct interaction of the PEG with the nanoparticle core. For the nanorods, the interaction of the PEG with the Au surface would in addition be screened by the strong attraction provided by the cationic sites of the CTAB. The negatively charged ether oxygens of the PEG chains can lead to attachment with multiple CTAB sites, yielding a total binding energy of several eV [36, 41]. This would also be responsible for the higher absolute fluence thresholds found for the rods in comparison to the spheres and stars. The role of the polymeric coatings in the enhancement of the thermal LDI mechanism is supported by the realization that previous investigations with an array of bare isolated nanorods grown on a non–conducting substrate [10, 11] yielded appreciably higher LDI ion yields from plasmon excitation at 532 nm, in comparison to non–plasmonic excitation at 355 nm, in a qualitatively similar to manner as found here for the nanospheres. For the nanospheres the thermal mechanism in the present experiments should still be relevant, if not dominant, but it appears that the light citrate coating allows for a partial exposure of the enhanced local field and charge effects

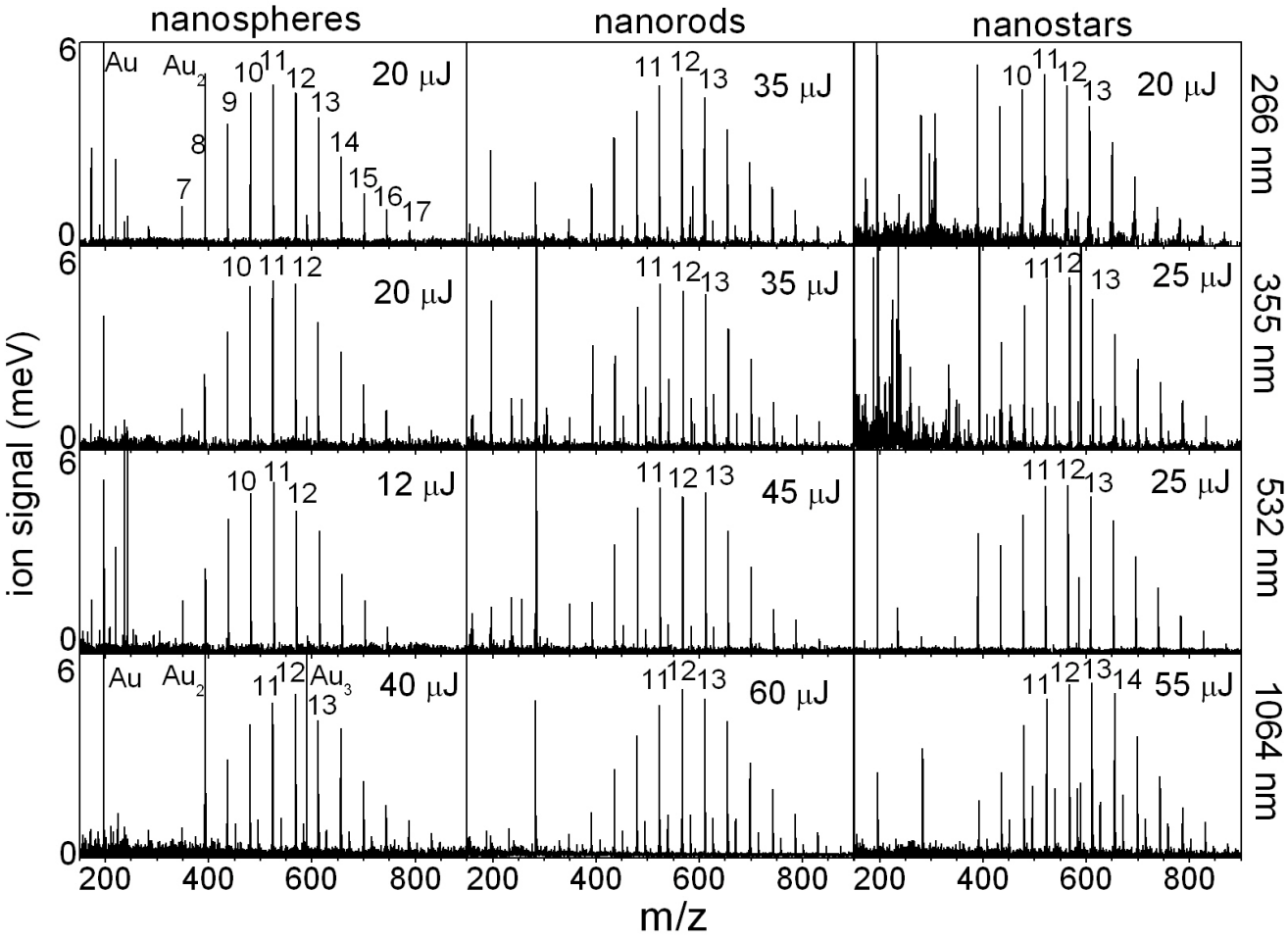

Figure 2.3: Typical LDI RETOF–MS spectra of PEG600 deposited on the gold nanospheres (left), nanorods (center) and nanostars (right), recorded at the four laser wavelengths of the present investigation (266–1064 nm, top to bottom) . The spectra have selected selected as to have ~ 5 meV signal in the main PEG600–Na^+ adduct peaks. The laser pulse fluence (H_{th}) applied and the signal/noise ratio (S/N) achieved in the spectra are indicated in each panel. The main peak distribution around m/z= 400–800 corresponds to PEG600-Na^+ adducts. The peaks are labelled according to the number of monomers n in the $HO(CCO)_nH$ polyether chain (for most panels only the most intense peaks are labelled). A weak distribution of PEG600–K^+ from residual potassium present in the sample is occasionally observed. Peaks associated to Au^+, Au_2^+ and Au_3^+ particles ablated from the nanoparticles are indicated. Several peaks from additives and protective agents are also observed at low masses ($m/z < 300$).

associated with plasmon excitation.

Fig. 2.3 displays typical LDI RETOF–MS spectra of the PEG–Na^+ adducts recorded above threshold. The spectra have been selected having ~ 5 meV signal in the main PEG600–Na^+ adduct peaks. They serve to illustrate the overall quality of the molecular weight distributions measured at moderate laser energies with the gold nanoparticles presently explored. The three types of nanoparticles yielded well resolved mass distributions of the PEG at the four wavelengths considered, although a different laser fluence had to be employed in each case to achieve similar signal/noise ratios. The number of monomers of the PEG chain corresponding to each of the PEG–Na^+ peaks detected is indicated in the spectra. Background signal from Au^+, Au_2^+ and Au_3^+ ions desorbed from the substrates and from low mass impurities ($m/z < 300$) is also observed. The use of a polydispersed PEG standard in the present study serves to evaluate the molecular weight selectivity of the LDI process and, hence, its ability to determine reliable molecular weight distributions of synthetic polymers. The most abundant chain length of the PEG600 standard is $n = 14$ ($m/z = 657$ for the PEG-Na^+ adduct; *e.g.*, see ref. [**?**]). In the LDI MS spectra with the three substrates, the most intense peaks in the PEG distribution correspond to $n = 11$–12 for the three UV–vis laser wavelengths, and to $n = 12$–13 for 1064 nm. Hence, a sizeable shift of the LDI peak distribution toward lower masses is observed with respect to the actual molecular weight distribution of the polymers. A similar decrease in detection sensitivity with growing polymer size resulted from previous LDI studies employing nanoparticles of metals other than gold [18]. The reduced LDI signal for the higher masses can be attributed to the stronger attachment of the longer polymeric chains to the nanoparticles. The spectra in Fig. 2.3 show that for the three nanoparticles, the shift of the distribution is less marked at 1064 nm

in comparison to the shorter wavelengths, likely due to the greater laser fluences required to produce the spectra. The high laser fluences applied to the nanorods to initiate the LDI process seems also to compensate for the stronger binding of the PEG polymers to the CTAB coating, leading to molecular weight distributions not too dissimilar from those of the nanostars.

2.5 Conclusions

The performance of gold nanospheres, nanorods and nanostars as substrates to assist the laser desorption/ionization of a model polydispersed synthetic polymer has been tested at four wavelengths covering the UV, visible and near infrared ranges. The present investigation extends previous studies with gold nanospheres and incorporates the randomly oriented CTAB–protected nanorods, and the PVP–protected gold nanostars as novel LDI substrates. The study has demonstrated the ability of the three types of gold nanoparticles to produce well resolved distributions of cationized adducts of a polydispersed polyether standard at the four wavelengths investigated. It can be concluded that gold nanoparticles may be employed as LDI substrates over a broad range of wavelengths, especially the nanorods and nanostars, due to the extension of their plasmonic bands to the near infrared.

For the gold nanorods and nanostars, a close correlation between the laser fluence thresholds and the optical absorbance is found both in the valence electron excitation region and throughout the plasmonic bands. This observation indicates that a similar local heating of the nanoparticle environment is required to reach the LDI threshold. Consequently, a thermal mechanism, weakly dependent on the type of electronic excitation induced by the laser radiation, is likely to dominate the LDI process assisted by the nanorods and nanostars. For the gold nanospheres, a fair correlation between LDI thresholds and absorbances is also found, although in this case plasmonic excitation of the nanoparticles with visible wavelengths leads to a sizeable increase in the efficiency of the LDI process (relative to absorbance) with respect to excitation in the UV. This trend can be attributed to the exposure of the plasmonic interaction between the PEG analytes and the Au core of the nanospheres, an effect that would be quenched in the nanorods and nanostars due to the coating with bulky protective agents.

The mass spectra recorded in our study show that the nanoparticle assisted LDI process leads to peak distributions for the polydispersed PEG600 standard that are shifted to lower masses with respect to the true molecular weight distribution. Such effect can be expected for analytes capable of attaching to the nanoparticle material through multiple attachment sites, leading to greater binding energies (and hence, reduced LDI sensitivity) with increasing molecular size.

The group is currently devoted to extend these results to platinum nanoparticles synthesized by laser ablation [43] and chemical reduction as long as rere earth nanocristalline oxydes.

Table 2.1: Laser pulse energy (E_{th}, μJ) and fluence (H_{th}, kJ m^{-2}) thresholds for the LDI detection of PEG600 with signal/noise ratio $S/N \approx 3$, obtained with the gold nanosphere, nanorod and nanostar substrates. The relative *inverse* fluence thresholds, normalized with respect to the value at 532 nm, $H_{th}(532\text{nm})/H_{th}(\lambda)$, and the relative optical absorbances of the nanoparticle substrates, $A(\lambda)/A(532\text{nm})$, are also included in the table. The degree of correlation between these two relative quantities, also illustrated in Fig. **??**, serves to evaluate the thermal character of the desorption/ionization mechanism.

Substrate		266 nm	355 nm	532 nm	1064 nm
spheres	$E_{th}(\lambda)$	7	8	5	20
	$H_{th}(\lambda)$	0.89	1.02	0.64	3.96
	$H_{th}(532\text{nm})/H_{th}(\lambda)$	0.72	0.63	1.00	0.16
	$A(\lambda)/A(532\text{nm})$	1.25	0.87	1.00	0.03
rods	$E_{th}(\lambda)$	20	22	30	40
	$H_{th}(\lambda)$	2.55	2.80	3.82	7.97
	$H_{th}(532\text{nm})/H_{th}(\lambda)$	1.50	1.36	1.00	0.48
	$A(\lambda)/A(532\text{nm})$	1.70	1.60	1.00	0.55
stars	$E_{th}(\lambda)$	6	9	9	15
	$H_{th}(\lambda)$	0.76	1.14	1.14	2.98
	$H_{th}(532\text{nm})/H_{th}(\lambda)$	1.50	1.00	1.00	0.38
	$A(\lambda)/A(532\text{nm})$	1.60	1.15	1.00	0.32

Bibliography

[1] K. Tanaka, H. Waki, Y. Ido, S. Akita, Y. Yoshida, T. Yoshida. Rapid Comm. Mass Spectrom. 2 (1988) 151.

[2] J. Sunner, E. Dratz, Y. Chen. Anal. Chem. 67 (1995) 4335.

[3] S. Owega, E. P. C. Lai, A. D. O. Bawagan. Anal. Chem. 70 (1998) 2360.

[4] M. Schürenberg, K. Dreisewerd, F. Hillenkamp Anal. Chem. 71 (1999) 221.

[5] J. A. McLean, K. A. Stumpo, D. H. Russell. J. Am. Chem. Soc. 127 (2005) 5304.

[6] Y. F. Huang, H. T. Chang. Anal. Chem. 78 (2006) 1485.

[7] B. N. Y. Vanderpuije, G. Han, V. M. Rotello, R. W. Vachet. Anal. Chem. 78 (2006) 5491.

[8] L. Hua, J. R. Chen, L. Ge, S. N. Tan. J. Nanopart. Res. 9 (2007) 1133.

[9] C. L. Su, W. L. Tseng. Anal. Chem. 79 (2007) 1626.

[10] L. C. Chen, J. Yonehama, T. Ueda, H. Hori, K. Hirakoa. J. Mass Spectrom. 42 (2007) 346.

[11] L. C. Chen, T. Ueda, M. Sagisaka, H. Hori, K. Hirakoa. J. Phys. Chem. C 111 (2007) 2409.

[12] M. T. Spencer, H. Furutani, S. J. Oldenburg, T. K. Darlington, K. A. Prather. J. Phys. Chem. C 112 (2008) 4803.

[13] E. T. Castellana, D. H. Russell. NanoLett. 7 (2007) 3023.

[14] H. Kawasaki, T. Yonezawa, T. Watanabe, R. Arakawa. J. Chem. Phys. C 11 (2007) 16278.

[15] K. Shrivas, H. F. Wu. Rapid Comm. Mass Spectrom. 22 (2008) 2863.

[16] H. Kawasaki, T. Sugitani, T. Watanabe, T. Yonezawa, H. Moriwaki, R. Arakawa. Anal. Chem. 80 (2008) 7524.

[17] L. C. Chen, K. Mori, H. Hori, K. Hirakoa. Int. J. Mass Spectrom. 279 (2009) 41.

[18] T. Yonezawa, H. Kawasaki, A. Tarui, T. Watanabe, R. Arakawa, T. Shimada, F. Mafune. Anal. Sci. 25 (2009) 339.

[19] J. Duan, M. J. Linman, Y. Chen, Q. J. Cheng. J. Am. Soc. Mass Spectrom. 20 (2009) 1530.

[20] N. Cioffi, L. Colaianni, R. Pilolli, C. D. Calvano, F. Palmisano, P. G. Zambonin. Bioanal. Chem. 394 (2009)1375.

[21] M. C. Daniel, D. Astruc. Chem. Rev. 104 (2004)293.

[22] Z. Guo, A. A. A. Ganawi, Q. Liu, L. He. Anal. Bioanal. Chem. 308 (2006) 584.

[23] J. N. Anker, W. P. Hall, O. Lyandres, N. C. Shah, J. Zhao, R. P. van Duyne. Nature Mat. 7 (2008)442.

[24] S. M. A. B. Batoy, E. Akhmetova, S. Miladinovic, J. Smeal, C. L. Wilkins. App. Spect. Rev. 43 (2008) 485.

[25] S. Link, M. A. El–Sayed. Int. Rev. Phys. Chem. 19 (2000) 409.

[26] S. Link, M. A. El–Sayed. Ann. Rev. Phys. Chem. 54 (2003) 331.

[27] A. Moores, F. Goettmann. New J. Chem. 30 (2006)1121.

[28] J. Zhao, A. O. Pinchuk, J. M. McMahon, S. Li, L. K. Ausman, A. L. Atkinson, G. C. Shatz. Acc. Chem. Res. 41 (2008)1710.

[29] M. Pelton, J. Aizpurua, G. Bryant. Rev. 2 (2008) 136.

[30] M. Hayat. *Colloidal gold: principles, methods and applications* San Diego, 1989. Academic.

[31] X. Liu, M. Atwater, J. Wang, Q. Huo. 58 (2007) 3.

[32] T. K. Sau, C. J. Murphy. Langmuir 20 (2004) 6414.

[33] D. A. Zweifel, A. Wei. Chem. Mater. 17 (2005) 4259.

[34] F. Hao, C. L. Nehl, J. H. Hafner, P. Nordlander. Nano Lett. 7 (2007) 729.

[35] C. G. Khouri,T. Vo–Dinh. J. Phys. Chem. C 112(2008) 18849.

[36] A. R. Hortal, P. Hurtado, B. Martínez–Haya, A. Arregui, L. Bañares. J. Phys. Chem. B 112 (2008) 8530.

[37] G. Montaudo, F. Samperi, M. S. Montaudo. Prog. Polym. Sci. 31 (2006) 277.

[38] W. L. Cheng, S. J. Dong, E. K. Wang. Angew. Chem. Int. Ed. 42 (2003) 449.

[39] K. A. Stumpo, D. H. Russell. J. Phys. Chem. C 113 (2009) 1641.

[40] C. L. Nehl, H. Liao, J. H. Hafner. Nano Lett. 6(2006) 683.

[41] P.B. Armentrout. Int. J. Mass Spectrom. 193 (1999) 227.

[42] E. W. Robinson, D. E. Garcia, R. D. Leib, E. R. Williams. Anal Chem. 78 (2006) 2190.

[43] M. Cueto, M. Sanz, M. Ouija, F. Gámez, B. Martínez-Haya, M. Castillejo. J. Phys.Chem. C 115 (2011) 22217.

Chapter 3

Nanoparticle TiO_2 films prepared by pulsed laser deposition: laser desorption and cationization of model adsorbates

Titanium dioxide stands as a low cost photocatalytic material in the chemical industry. This work provides an extended insight into the use of TiO_2 nanostructures in laser assisted laser desorption ionization (LDI) of small peptides and synthetic polymers. The investigation evaluates the interfacial morphologies in the nanoscale that enhance the LDI efficiency in nanoparticle–assembled TiO_2 films prepared by femtosecond and nanosecond pulsed laser deposition (PLD) at different laser wavelengths. It is shown that PLD provides robust substrates yielding LDI pulse energy thresholds and signal/noise ratios in the mass spectra for the detection of cationized adducts that can be comparable to those obtained with TiO_2 nanoparticle suspensions and with conventional organic matrices. The best LDI performance is found for nanosecond PLD crystalline substrates of the anatase polymorph and for femtosecond PLD amorphous substrates, with average nanoparticle sizes in both cases in the range 25–55 nm.

3.1 Introduction

Metal oxide nanostructures offer important advantages for photocatalytic and photovoltaic applications. Modern laser desorption mass spectrometry is also intensively exploring their use as active substrates [1, 2], with the aim to surpass the capabilities of conventional matrix assisted laser desorption/ionization (MALDI). The development of MALDI during the 1980's fueled a remarkable revolution in biochemical analysis [3, 4]. However, the use of the organic matrices in MALDI implies several limitations, such as the need for the physicochemical compatibility between matrix and analytes (solubility, proton and electron affinity, etc), what in practice makes the choice of the adequate matrix a trial-and-error procedure [5]. Matrix photochemistry also produces an interfering signal, preventing the routine detection of analytes with molecular weights below 500 g/mol. These technical concerns, together with more fundamental motivations, have stimulated the development of matrixless laser desorption/ionization (LDI) techniques. Noticeably, the pioneering work that granted Koichi Tanaka the 2002 Nobel Price in Chemistry was based on LDI assisted by metal particles rather than organic matrices [3].

Titanium dioxide, TiO_2, is a low–cost semiconductor extensively employed as a functional material in a number of applications ranging from photocatalysis, photovoltaics and sensor technology [6]. The band gap of TiO_2 lies within 3.0–3.2 eV, depending on its microscopic solid structure, making it also particularly suitable for near–ultraviolet laser desorption mass spectrometry. Surprisingly, the use of TiO_2 in this field is relatively recent, in contrast with the more developed mass spectrometric application of other semiconducting materials, such as silicon, carbon and further mesoporous materials [1, 2, 7]. Previous investigations have demonstrated the feasibility of employing TiO_2 micrometric and nanometric particles to assist the LDI detection of low molecular weight adsorbates of different polarity [2, 8, 9, 10, 11, 12, 13, 14, 15]. One main conclusion inferred from those studies is the relevance of the surface properties at the nanoscale for the efficiency of the laser desorption process. Nevertheless, the mechanistic background involved in the desorption and ionization stages is still largely unknown.

The importance of controlling the nanoscale morphology in TiO_2 substrates for specific applications is not new and has attracted numerous recent investigations [16]. In particular, pulsed laser deposition (PLD) has been widely employed to produce titanium oxide films with different morphology and crystalline phase [17, 18, 19, 20, 21, 22, 23, 24, 25, 26, 27, 28, 29, 30, 31]. The coating of sample plates with PLD TiO_2 films has been used to enhance the MALDI detection of phosphopeptides [31]. However, investigations on the application of PLD films in LDI mass spectrometry (without the addition of any organic matrix to assist desorption/ionization) are lacking.

The main aim of our study is then to explore in a systematic way the nanoscale features of TiO_2 films that enhance LDI efficiency, and to establish the PLD parameters adequate for their production. In particular, laser pulse duration and wavelength, substrate temperature and background atmospheric environment are varied to produce PLD films with crystalline or amorphous structure and surface nanostructures with sizes ranging from tens to hundreds of nanometers. Importantly, the resulting films are robust and washable, and could be used several times without deterioration.

3.2 Experimental Methods

3.3 Experimental Methods

Chemicals. The tripeptide Gly–His–Gly, polydispersed polyethylene glycol PEG600 and the MALDI matrices 2,5-Dihydroxybenzoic acid (2,5–DHB) and dithranol, were supplied by Sigma–Aldrich and used without further purification. Solvents (methanol, ethanol) of HPLC grade and nitric acid were purchased from Panreac. Water was purified using a Mili-Q (18.2 M) reagent grade water system from Millipore.

TiO_2 nanoparticle substrates. TiO_2 nanoparticles (NP) of average size 25 nm (Evonix P25; 70% anatase, 30% rutile) were used for the present study. The nanoparticles were stabilized in acidic miliQ:EtOH 1:3.25 (v/v) medium, at pH 3.5 reached by addition of diluted HNO_3. Such solution was directly employed as matrix for the LDI measurements. Alternatively, substrates of sinterized P25 TiO_2 NPs were produced by doctor-blade methods [32]. In particular, an acidic miliQ:EtOH solution of nanoparticles at concentration 0.18 g/mL was spread onto a glass slide and then dried in air. A Scotch tape of 50 micron thickness was used to achieve a TiO_2 film thickness within 10–15 micron after sintering in air at 723 K (450 ^{o}C) during 30 min.

Pulsed Laser Deposition of TiO_2 and film characterization. PLD nanostructured films were prepared by ablation of TiO_2 targets onto a Si(100) substrate under repetitive laser irradiation. The resulting films are constituted by the assembly on the substrate of the nanoparticles ejected from the target. A set of films were produced by ablation with a nanosecond Q–switched Nd:YAG laser (Quantel, Brilliant B) at 266, 355 or 532 nm (pulse duration 5 ns, repetition rate 10 Hz, fluence 3 J cm^{-2}). Deposits were grown by delivering 7200

Table 3.1: Growth conditions, crystallinity and average size of the nanoparticles and particulates formed at the interface of the TiO_2 PLD films included in the present study

Sample name	λ (nm)	Laser pulse duration	Atmosphere	Substrate temperature	Crystalline phase	Size range of particulates (nm)	Average size of nanoparticles (nm)
ns266A	266	5 ns	Vacuum	923 K	Anatase	300–500	55
ns266R	266	5 ns	Oxygen	923 K	Rutile	200-400	25
ns355R	355	5 ns	Oxygen	923 K	Rutile	200-500	45
ns532R	532	5 ns	Oxygen	923 K	Rutile	1000-1500	55
fs266	266	60 fs	Vacuum	298 K	Amorphous	100	30
fs400	400	60 fs	Vacuum	298 K	Amorphous	100–200	50
fs800	800	60 fs	Vacuum	298 K	Amorphous	150–300	50

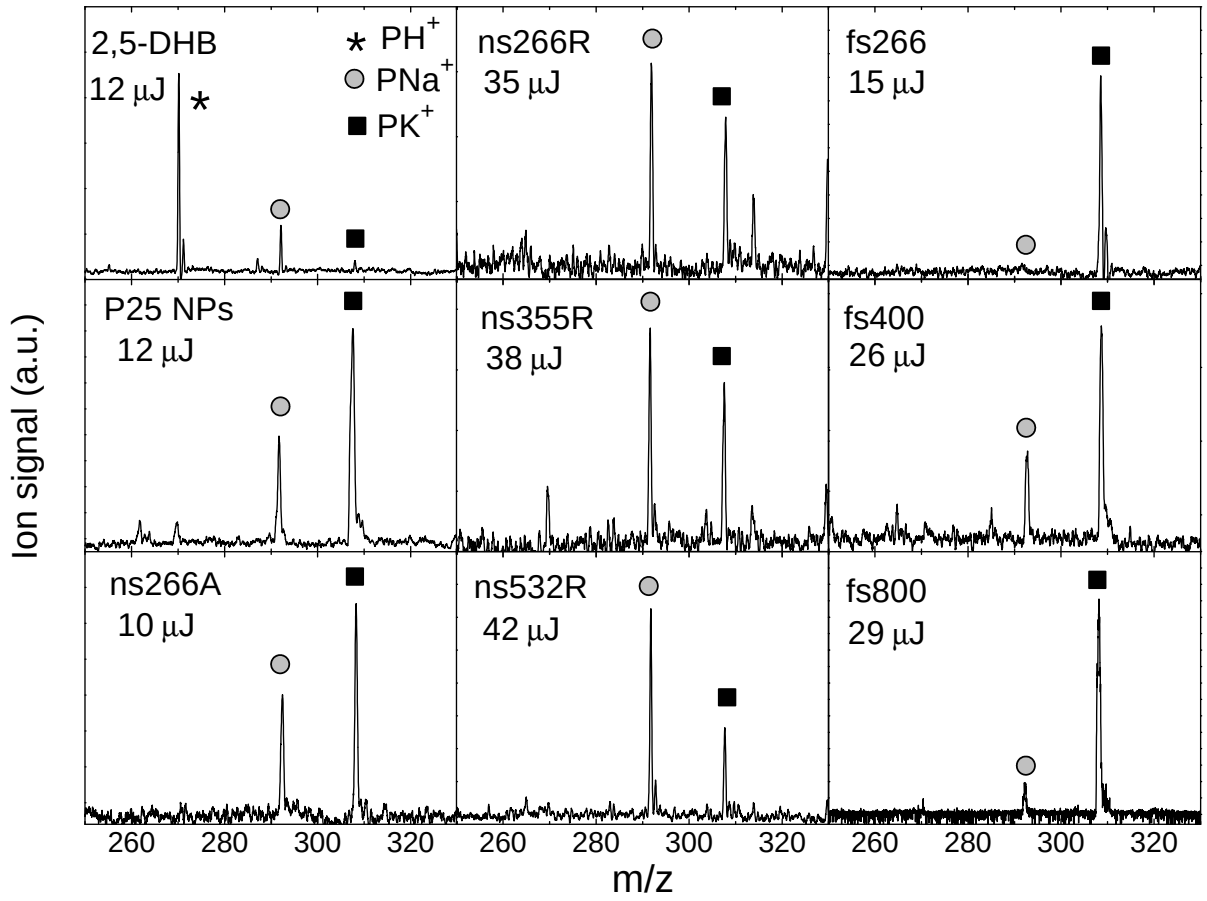

Figure 3.4: LDI RETOF–MS spectra of Gly–His–Gly recorded with the different nanoparticle TiO_2 films included in the present study at laser pulse energies roughly 30% above threshold. The peptide (P) is cationized by Na^+ (circles) and K^+ (squares) impurities present in the sample. See Table 3.1 for a description of the interfacial features of the PLD TiO_2 films. In the analogous spectrum obtained with the conventional 2,5–DHB matrix (upper–left panel), the protonated peptide adduct (asterisk) dominates the ion yield.

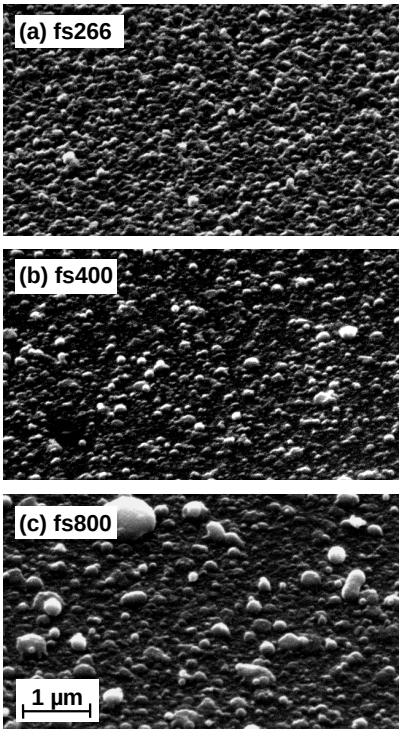

Figure 3.1: Environmental scanning electron microscopy (ESEM) images of the three TiO_2 nanoparticle films prepared by femtosecond PLD in vacuum at 298 K with laser wavelength of: a) 266 nm, b) 400 nm, and c) 800 nm. The images are representative of the interfacial nanoparticle structures considered in the present study. See Table 3.1 for a description of the PLD parameters and surface features of the complete set of TiO_2 films investigated.

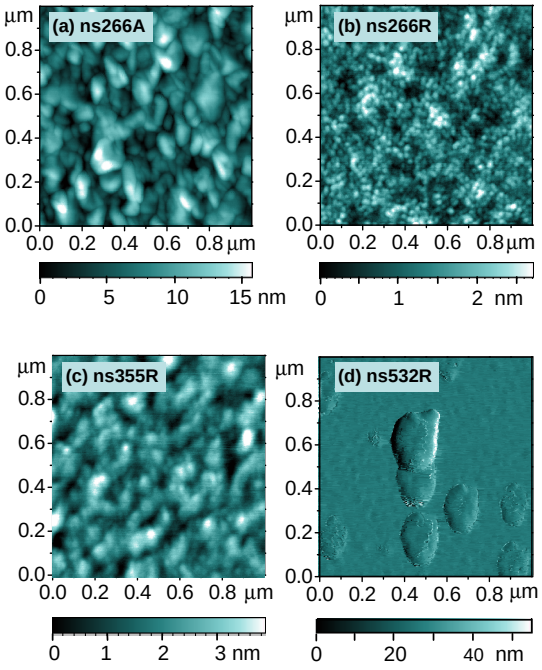

Figure 3.2: Atomic force microscopy (AFM) images of the TiO_2 nanoparticle films prepared by nanosecond PLD at 923 K with laser wavelength of: a) and b) 266 nm, c) 355 nm, and d) 532 nm. In a) deposits were grown in vacuum, leading to an anatase crystalline phase for the nanoparticles, and in b)-d) under 0.05 Pa of oxygen, leading to the rutile phase. The images are representative of the surface morphologies and topographies considered in the present study. See Table 3.1 for a description of the PLD parameters and surface features of the complete set of TiO_2 films investigated. Note the different height ranges of the color scale of each image.

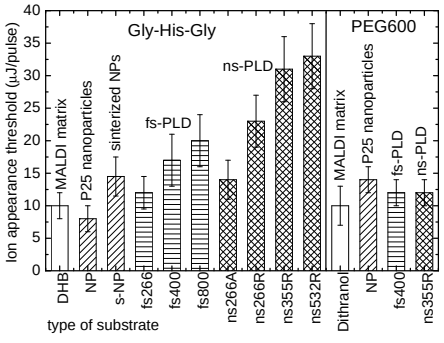

Figure 3.3: Laser pulse energy thresholds for the laser desorption ionization of Gly–His–Gly and PEG600 assisted by the different nanostructured TiO_2 substrates included in the present study. See Table 3.1 for a description of the surface features of the PLD TiO_2 films.

pulses to the target [28, 29]. The substrate was placed at 2–4 cm distance from the TiO_2 and was heated to 923 K (650 ^{o}C) during deposition by means of a Kanthal LT (a ferritic iron-chromium-aluminium alloy) resistive heater. Deposition was performed either in vacuum or in oxygen atmosphere at a pressure of 0.05 Pa. Alternatively, a femtosecond laser system was employed [30]. In this case, pulses of 60 fs were produced in a Ti:Sapphire amplified laser system (Spectra Physics) centered at 800 nm at a repetition rate of 1 kHz. Pulses of 400 nm and 266 nm were generated using a BBO–based frequency doubler/tripler. Energy control was performed using a variable neutral density filter. Ablation was carried out at laser fluences slightly above the ablation threshold, with values 0.140, 0.124, and 0.075 J cm^{-2} for 800, 400 and 266 nm, respectively. Femtosecond deposits were fabricated with 720000 pulses, while the substrate was kept at room temperature (298 K).

The crystalline phase and the surface structural features of the PLD deposits were characterized by X-Ray diffraction (XRD, Philips XPert), environmental scanning electron microscopy (ESEM, Philips XL30) and atomic force microscopy (AFM, PicoLE, Molecular Imaging). ESEM images were taken to characterize the interfacial nanoparticle structures. In addition, the surface morphology and topography was investigated in greater detail by AFM. Figs. 3.1 and 3.2 present illustrative ESEM and AFM images of the deposits created using femtosecond and nanosecond lasers, respectively. Average particle sizes and roughnesses of the substrate interfaces were evaluated by means of the digital image processing software SPIP^{TM} (Image Metrology A/S, Denmark).

A set of both relevant PLD operating conditions and film properties are provided in Table 3.1. As can be appreciated, the crystalline phase of the films depends on the deposition conditions. Anatase and rutile crystalline

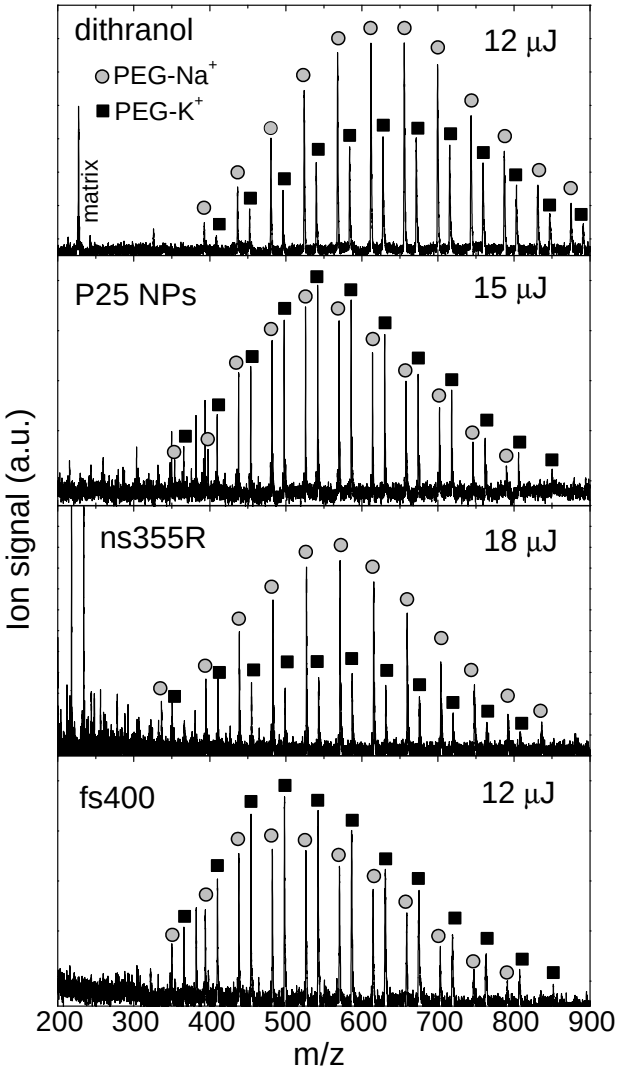

Figure 3.5: LDI RETOF–MS spectra of PEG600 recorded with a representative set of nanoparticle TiO_2 film substrates. Peak series from cationization by Na^+ (circles) and K^+ (squares) are observed in each spectrum. See Table 3.1 for a description of the interfacial features of the PLD TiO_2 films.

phases are found in the films fabricated with nanosecond pulses; femtosecond irradiation yielded amorphous films. The deposits were also analyzed by X-ray photoelectron spectroscopy [29, 30], which revealed stoichiometric composition. The fs PLD deposits consist of TiO_2 nanoparticles of 30 or 50 nm average size, with overimposed larger particulates in the 100 to 300 nm range. On the other hand, ablation with ns laser pulses yielded interfacial nanoparticle structures with average sizes in the 25–55 nm range. The formation of particulates on the surface was higher for nanosecond than for femtosecond laser pulses, reaching diameters above 200 nm and up to 1500 nm. The overall differences in the nanoparticle films produced with ns *vs*. fs lasers can be attributed to the influence of laser pulse duration on the ablation dynamics (rather than *e.g*. laser power density), as shown in previous investigations [18, 19, 20, 21, 22, 23, 24, 25, 26, 27, 28, 29, 30, 31].

MALDI Instrumentation and method. LDI mass spectrometry measurements in positive ion mode were performed in a reflectron time–of–flight mass spectrometer (RETOF–MS) already employed in a number of previous investigations, including one study on LDI assited by metallic nanoparticle substrates [33]. The equipment is described here only briefly. The sample plate is mounted on the repeller plate of the Wiley–MacLaren type ion source and receives the desorbing laser beam at 45 degree incidence. Analyte ions are accelerated through a voltage drop of 4.2 kV, applied with a 1 μs delay with respect to the laser pulse. The reflectron is operated with a 4.5 kV voltage rise to reflect the ions toward the multichannel–plate detector. Excitatrix 355 nm light was produced with a Minilite II-Continuum Nd:YAG laser and was focused on the sample with a lens of 25 cm nominal focal length. Laser pulses with 5 ns duration and energies ranging 1–100 μJ were applied. Pulse energies throughout the text refer to values on the sample, after calibration to account for losses due to optical components. Pulse–to–pulse energy stabilities were within 5 %. The mass spectra were averaged over 128 laser shots, at 10 Hz operation. The only data treatment performed on the recorded spectra was simple smoothing over adjacent TOF channels.

LDI Samples were prepared by spotting aliquots of 1 mM solutions of the analyte (Gly–His–Gly or PEG600) on the PLD substrate and subsequent air drying of the solvent. The same procedure was applied with the sinterized doctor-blade substrate. The volume of sample solution deposited on the PLD substrates (several microliter) was calculated as to provide the same number of moles of analyte per unit area of the sample plate (about 10^{-9} mol cm^{-2}). The samples with the P25 nanoparticles were prepared by air–drying 5 μL of a solution with 1:1 analyte:NP molar ratio, on a stainless–steel plate. Remarkably, no significant changes in the LDI thresholds were appreciated when the amount of analyte spotted on the PLD substrates, or the analyte/nanoparticle molar ratio were varied over more than one order of magnitude. No cationizing agents (*e.g*., alkali salts) were added to any of the samples.

LDI threshold measurements. The LDI ion appearance thresholds were conveniently defined as the laser pulse energy required to record mass spectra with a signal-to-noise ratio of S/N≈3 for the strongest adduct peak. In a typical experiment, the laser pulse energy was slowly increased until an incipient analyte ion signal was observed, corresponding to the analyte either protonated or cationized by the Na^+ or K^+ impurities of the sample. A series of LDI mass spectra were then collected up to pulse energies well above threshold. The experiments were repeated on up to five independent sample/substrate systems prepared under the same conditions. Sample–to–sample variation of the relative values of the thresholds observed on each sample was within 15% (estimated as the standard deviation of the independent experiments). In order to minimize "sweet–spot" effects, the sample plate was continuously rotated during the data collection.

3.4 Results

The tripeptide Gly–His–Gly (m/z= 269) and the polyethylene glycol PEG600 (m/z= 400–800) were chosen as low molecular weight model compounds to evaluate the LDI efficiency of the different types of TiO_2 substrates. For comparison, a similar study was carried out with conventional MALDI matrices (2,5–DHB for the peptide, dithranol for PEG). Fig. 3.3 depicts the laser pulse energy thresholds obtained for the different analyte/substrate combinations investigated in this work. Figs. 3.4 and 3.5 show representative LDI mass spectra for the different analyte/substrate combinations.

LDI of the Gly–His–Gly peptide

We discuss in the first place the results for the Gly–His–Gly peptide. For this model analyte, the threshold with the P25 NPs (7.5 μJ) was smaller than the one observed for the conventional 2,5–DHB matrix (10 μJ), corroborating the good LDI performance of TiO_2 reported in earlier works [2, 8, 9, 11, 12, 13, 14, 15]. Moreover, the 2,5–DHB matrix leads to a higher dispersion of the threshold data, as a consequence of the greater heterogeneity of the crystallized sample. Interestingly, relatively low thresholds for the Gly–His–Gly analyte were also achieved with at least two of the PLD substrates, namely with the ns266A anatase substrate deposited with 266 nm nanosecond laser pulses (14 μJ threshold), and with the fs266 amorphous substrate produced with 266 nm femtosecond laser pulses (12 μJ threshold). Noticeably also, the fs266 substrate

yields a threshold roughly 30% lower than those achieved with the fs400 (17.5 μJ) and fs800 (20 μJ) substrates, deposited with femtosecond pulses of 400 and 800 nm, respectively. This result indicates that more efficient analyte–substrate interactions leading to desorption follow from the smaller average size of the nanoparticles and the reduced presence of particulates, resulting from the PLD process with the fs laser at 266 nm in comparison to the two longer wavelenghts (see Table 3.1). A similar trend is observed if the three rutile phase PLD substrates produced with the nanosecond lasers are compared. In this case, the ns266R substrate with nanostructures of average 25 nm size leads again to roughly 30% lower thresholds than the ns355R and ns532R substrates, featuring 45 nm and 55 nm surface structures, respectively.

The crystallinity of the film constitutes an even more relevant aspect. The rutile films yield appreciably higher thresholds than the anatase ns266A film, produced with the same laser wavelength and pulse duration. This finding is remarkable, since the smaller nanoparticle and particulate sizes that characterize the ns266R *versus* the ns266A film are more favourable for LDI. A similar superiority of the anatase phase for LDI has been noticed in previous studies [13], correlating well with the better general properties of this phase of TiO_2 as photocatalyst [34]. The rutile nanocrystalline structure is less robust against electronic photoexcitation, due to oxygen vacancies and titanium interstitials (so called native defects) that weaken the crystalline structure [6, 13, 35]. In fact, background peaks from non–stoichiometric Magneli–type clusters $Ti_nO_{(2n-1)}$ (n= 2,3) were observed in the small m/z range of the LDI spectra obtained from the rutile substrates. Such peaks were absent in the spectra for the anatase and amorphous substrates. The activation of photoinduced processes competitive with desorption upon irradiation of the rutile surface is then likely to be responsible for the higher threshold values observed for the rutile phase films.

The comparatively good LDI performance of at least some of the deposits indicates that the surface nanostructures generated with the PLD method have sufficient three–dimensional topology as to yield adsorption and interactions with the analyte and subsequent energy transfer for laser desorption of similar efficiency as the bare nanoparticles. In order to further explore the relevance of the dimensionality of the surface structure, LDI threshold measurements for the same Gly–His–Gly analyte were performed with substrates prepared by sinterization of the P25 nanoparticles. Previous studies have employed films of sinterized TiO_2 nanoparticles to functionalize MALDI plates for the selective capture of phosphoproteins [11]. In our experiments, the performance of the sinterized NP films (LDI threshold of 15 μJ) was slightly higher that those of the fs266 and ns266A PLD deposits, but yielded a stronger background signal. In addition, the sinterized films were more fragile against the action of the laser, of vacuum and of washing solvents, which prevented their use more than one or two times. In contrast, the PLD deposits were robust and could be used several times without deterioration.

It seems timely to remark that whereas the LDI efficiency of the PLD substrates correlates with the average size of the nanoparticles at the interface (smaller sizes, within the range scoped in this study, lead to lower LDI thresholds), it is found to be roughly insensitive to the specific area of the substrates. In fact, all the PLD films explored in this work have specific areas differing from each other by less than 20 percent. The weak correlation of LDI performance and specific area becomes particularly apparent from the results obtained for the sinterized NP films just described. These films are highly porous and feature specific areas that are at least two orders of magnitude greater than those of the PLD films [36]. Yet, the sinterized NP films tested in this work did not provide any remarkable improvement in LDI performance. Hence, volumetric effects (*e.g.* pore depths) are of lesser relevance for the LDI process than the outermost interfacial morphology defined by the nanoparticles. This observation suggests that the analyte molecules preferentially released by the laser are those adsorbed on the nanoparticles, rather than incorporated to the deeper parts of the porous structure defined by the interface.

Fig. 3.4 depicts a representative set of LDI mass spectra for Gly–His–Gly recorded on the different TiO_2 substrates at laser energies typically 30% greater than threshold energies. A similar MALDI spectrum obtained with the 2,5–DHB matrix is also included for comparison. Whereas the most prominent peak in the MALDI mass spectrum corresponds to the protonated peptide adduct (P–H^+), the TiO_2–assisted LDI spectra are dominated by the alkali adducts, P–Na^+ and P–K^+. The high proton affinity of TiO_2 surfaces [37] apparently prevents the formation of protonated peptide adducts. In contrast, Na^+ and K^+ cations are effectively released from TiO_2. Hence, cationization occurs readily in the desorption plume, in this case by the alkali traces present in the sample (we recall that no cationizing agents were added). This finding is relevant, as it shows that the LDI ion yield observed in this type of experiments resembles the laser induced desorption efficiencies of the TiO_2 substrates, decoupled from complex secondary proton transfer ionization processes. It can be appreciated that good quality LDI mass spectra could be achieved with all of the PLD films tested. The substrates requiring a lower laser energy for analyte detection, P25 nanoparticles, fs266 and ns266A PLD deposits, also lead to greater signal/noise ratios, S/N$\sim$ 50–100 at pulse energies not far above threshold. Such value is similar to those provided by the 2,5–DHB matrix if only the P–Na^+ adducts are considered (for the main P–H^+ adduct the S/N ratio is fourfold greater). The mass resolution

attained in our equipment with the TiO_2 substrates was similar in all cases, $M/\Delta M \approx 600$. This is appreciably lower than the value of $M/\Delta M \approx 1000$ obtained with the 2,5–DHB matrix.

Na^+/K^+ adduct ratios

One noticeable effect observed in the LDI mass spectra of Fig. 3.4 arises in the intensity ratio of the peaks associated with the Gly–His–Gly peptide cationized by Na^+ and K^+. Such ratio appears to be characteristic of each type of substrate. Repetitions of the measurements with independent sample/substrate systems prepared under the same conditions confirmed this result. The three rutile phase substrates (ns266R, ns355R and ns532R) display similar adduct ratios favouring the Na^+ adducts. Opposite to this, the two anatase phase substrates (ns266A and P25 nanoparticles) yield more intense K^+ adduct peaks. A similar effect is observed when comparing previous LDI measurements of caffeine assisted by rutile and anatase substrates [13]. The three amorphous PLD substrates (fs266, fs400 and fs800) display an even more marked preference for adduct cationization by K^+; for the fs266 film the Na^+ even becomes negligible. It should be remarked that the anatase, rutile and amorphous PLD films were produced by nanosecond or femtosecond laser ablation of the same TiO_2 substrate material. In the experiments with the PEG600 polymers discussed below (Fig. 3.5) similar Na^+/K^+ cationization ratios are also observed for the substrates explored.

From these observations described above, it can be inferred that the relative yield of the Na^+ and K^+ adducts is presumably a consequence of the specific adsorption of the cations on each of the nanostructured surfaces, which would then control the release of cations to the LDI plume. It is not straightforward to provide a microscopic explanation for the selective adsorption of Na^+ and K^+ on the TiO_2 nanostructures derived from our experiments. Strong interaction with TiO_2 of small cations, such as H^+ and Li^+, mainly by intercalation have been reported [37]. Selective effects for the similar (weaker) interactions with the heavier alkali cations are less understood, in spite of the important number of works that have been devoted to their characterization [38, 39, 40, 41, 42, 43, 44]. Clearly, a more detailed analysis of the surface effects at the nanoscale would be required in order to rationalize the specificities for Na^+/K^+ cation retention on the TiO_2 substrates derived from our experiments. Such a study is outside the scope of the present investigation. Nevertheless, some tentative conclusions may be extracted from the results of the present study. First of all, the experiments show that the anatase crystalline phase of TiO_2 adsorbs Na^+ more efficiently than K^+, whereas the opposite holds for the rutile phase. This can be interpreted as the result of the different properties of the (011) and (001) crystalline faces dominant for anatase, in comparison to the (110), (100) and (101) faces dominant for rutile [41]. The different interfaces and types of defects exposed in each case may modulate the binding affinities for the two cations. On the other hand, the most marked effects are found in our LDI study of the three amorphous TiO_2 films, where Na^+ adsorption appears to be enhanced, even leading to the suppression of the GlyHisGly–Na^+ adduct peak in the fs266 substrate. Mesoscopic crystalline phases are absent in this case, although the abundance of interfacial defects can be invoked to explain absorption selectivity. On the other hand, the pronounced Na^+ absorption may also be related to the distinct film morphology of the PLD films produced with femtosecond laser pulses. Surface rearrangement during deposition was in this case limited, since the substrate was kept at room temperature. The resulting nanoporosity of these films apparently allows for the intercalation of the Na^+ cations in the TiO_2 structure, in a much more efficient way than for K^+.

LDI of the PEG600 polyether

We focus now the discussion on the results for the second class of model compounds considered in this study, the linear PEG polymers. The appreciable alkali cation affinity of the ether moieties makes PEG particularly suitable for LDI studies [45]. With PEG600 as model analyte, the dithranol MALDI matrix, the P25 nanoparticles and the fs400 and ns355R PLD substrates were compared in systematic LDI runs. Fig. 3.5 shows that good quality LDI mass spectra were obtained for PEG600 in all the substrates. The LDI spectra reflect the polydispersity of the polymer sample, and display a double distribution of peaks associated with the cationization by Na^+ and K^+. As mentioned above, the relative intensities of the PEG–Na^+/PEG–K^+ series correlates well with the intensities found for Gly–His–Gly in the same substrates: K^+ adducts are more intense for the P25 NPs and for the fs400 substrate, whereas the Na^+ adducts dominate for the ns355R substrate, as it is also the case for the dithranol matrix. These results confirm that it is the surface properties of the different titania samples the main factor that determines the performance of the substrates.

Fig. 3.3 shows that the LDI thresholds observed for PEG600 on the different substrates were similar to each other: a threshold of 12 μJ was observed for the fs400 and ns355R PLD substrates, in comparison to 14 μJ for the P25 nanoparticles and 10 μJ for the dithranol matrix. Hence, the LDI of PEG600 displays a weak dependence on the morphology of the substrate, in contrast to the behaviour described above for the Gly–His–Gly peptide. A differentiated physical property of PEG600 is that it is a viscous liquid at room temperature (298 K), so that sample preparation with the present methodology unavoidably results in a multilayer coating of the TiO_2 substrate. Under these conditions, the LDI process can be expected to proceed through a thermal mechanism, in which the TiO_2 domain excited by the laser dissipates energy by

heating several layers of PEG600. The nanometric properties of the surface would be of lesser relevance for the desorption process in this scenario. The stronger substrate dependence of the LDI of Gly–His–Gly would be the result of a more direct interaction of this adsorbate with the TiO_2 surface.

An important aspect of the LDI measurement on PEG is the evaluation of the capability of the TiO_2 substrates to characterize accurately the molecular weight distribution of polydisperse polymer samples. Similar experiments for PEG600 deposited on noble metal nanoparticle substrates showed that the weight distribution was shifted to lower masses [33]. This effect was interpreted to be a consequence of the stronger adsorption of the longer polymer chains to the nanoparticles due to the larger number of binding sites available in the polymer backbones of greater length. Fig. 3.5 shows that a similar shift is observed in the LDI assisted by the TiO_2 nanostructures. Whereas the distribution delivered by the dithranol matrix is in accord with the specifications of the model compound, the distributions obtained with the NPs and the PLD substrates are shifted to lower masses by two monomeric units. We are led to conclude that the stronger attachment of the longer chains within the polydispersed PEG600 sample to the TiO_2 substrate limits the accurate determination of the molecular weight distributions. The application of greater laser pulse energies ($> 30\,\mu$J) in an attempt to desorb more efficiently the longer polymers of the sample eventually led to appreciable fragmentation of the polymers.

3.5 Conclusions

Pulsed laser deposition constitutes an efficient technique for the production of robust nanostructured films capable of assisting laser desorption/ionization of low molecular weight analytes amenable for cationization by metals. This has been illustrated in the present study for a model tripeptide (GlyHisGly) and a polydispersed mixture of polyethylene glycol chain polymers (PEG600). Lowest LDI thresholds and best quality of mass spectra are overall obtained with nanosecond–PLD films of the anatase crystalline polymorph, and for femtosecond–PLD amorphous substrates. Smaller nanoparticle sizes (25 nm) and a reduced presence of particulates on the film interface also lead to an enhanced LDI performance.

A systematic dependence on the crystallinity and surface morphology of the relative cationization yield of the peptide and polyether analytes by Na^+ and K^+ has been observed. The greatest differences adduct intensities for the two cations are observed for the amorphous PLD substrates produced with femtosecond laser pulses at room temperature. This effect is likely to be related to the selective adsorption of the Na^+/K^+ cations on the nanostructured films, although a more systematic study would be required to draw definite conclusions to this respect.

The LDI molecular weight distributions of the PEG600 polymers produced by the PLD films is shifted to smaller masses by one or two monomer units with respect to the nominal distribution of the polymer standard. This observation can be interpreted to follow from the stronger adsorption of the longer polymer chains to the nanoparticle films, due to the larger number of binding sites present in the polymer backbones as it was commented in the previous chapter.

Bibliography

[1] Z. Guo, A. A. A. Ganawi, Q. Liu, L. He. Anal. Bioanal. Chem. 308 (2006) 584.

[2] T. Kinumi, T.Saisu, M. Takayama, H. Niwa. J. Mass Spectrom. 35 (2000) 417

[3] K. Tanaka, H. Waki, Y. Ido, S. Akita, Y. Yoshida, T. Yoshida. Rapid Comm. Mass Spectrom. 2 (1988) 151.

[4] M. Karas, D. Bachmann, U. Bahr, F. Hillemkamp. Int. J. Mass Spectrom. Ion Proc. 78 (1987) 53.

[5] S. M. A. B. Batoy et al. App. Spectrosc. Rev. 43 (2008) 485.

[6] U. Diebold. Surf. Sci. Rep. 48 (2003) 53.

[7] D. S. Peterson. Mass Spectrom. Rev. 26 (2007) 19.

[8] C. T. Chen, Y. C. Chen. Anal. Chem. 77 (2005) 5912

[9] M. Yuan. Z. Shan, B. Yan, B. Tu, P. Yang, D. Zhao. Micropor. Mesopor. Mater. 78 (2005) 37.

[10] C. T. Chen, W. Y. Chen, P. J. Tsai, K. Y. Chien, J. S. Yu,Y. C. Chen. J. Proteome Res. 6 (2007) 316.

[11] L. Qiao, C. Roussel, J. Wan, P. Yang, H. H. Girault, B. Liu. J. Proteome Res. 6 (2007) 4763.

[12] K. H. Lee et al. Rapid Comm. Mass Spectrom. 21 (2007) 2023.

[13] A. L. Castro, P. J. Amorin Madeira, M. R. Nunes, M. F. Costa, M. H. Florêncio. Rapid Commun. Mass. Spectrom. 22 (2008) 3761.

[14] T. Watanabe, K. Okumura, K. Nozaki, H. Kawasaki, R. Arakawa. Rapid Commun. Mass Spectrom. 23 (2009) 3886.

[15] M. L. Niklew, U. Hochkirch, A. Melikyan, T. Moritz, S. Kurzawski, H. Schluter, I. Ebner, M. W. Linscheid. Anal. Chem. 82 (2010) 1047.

[16] X. Chen, S. S. Mao. Chem. Rev. 107 (2007) 2891.

[17] R. Eason. *Pulsed Laser Deposition on thin films: Applications–Led Growth of functional materials* John Wiley & Sons, New Jersey, 2006. ISBN-10: 0471447099

[18] J. H. Kim. S. Lee, H. S. Im. App. Surf. Sci. 151 (1999) 6

[19] E. György,A. Pérez del Pino, G. Sauthier, A. Figueras, F. Alsina, J Pascual. J. Phys. D: Appl. Phys. 40 (2007) 5246.

[20] H. Inoue, M. Yuasa, M. Okoshi. Appl. Surf. Sci. 197 (2002) 393.

[21] S. Murugesan, P. Kuppusami, N. Parvathavarthini, E. Mohandas. Surf. Coat. Technol. 201 (2007) 7713.

[22] S. Kitazawa, Y. Choi, S. Yamamoto, T. Yamaki. Thin Solid Films. 515 (2006) 1901.

[23] A. K. Sharma, R. K. Thareja, U. Willer, W. Schade. Appl. Surf. Sci. 206 (2003) 137.

[24] N. Koshizaki, A. Narazaki, T. Sasaki. Appl. Surf. Sci. 624 (2002) 197.

[25] T. Nakamura, E. Matsubara, N. Sato, A. Muramatsu, H. Takahashi. Mater. Trans. 45 (2004) 2068.

[26] M. Fusi, V. Russo, C. S. Casari, A. LiBassi, C. E. Bottani. Appl. Surf. Sci. 225 (2009) 5334.

[27] M. Walczak, M. Oujja, J. F. Marco, M. Sanz, M. Castillejo. Appl. Phys. A. 93 (2008) 735.

[28] M. Walczak, E. L. Papadopoulou, M. Sanz, A. Manousaki, J. F. Marco, M. Castillejo. Appl. Surf. Sci. 255 (2009) 5267.

[29] M. Sanz, M. Walczak, M. Oujja, A. Cuesta, M. Castillejo. Thin Solid Films. 517 (2009) 6546.

[30] M. Sanz, M. Walczak, R. de Nalda, M. Oujja, J. F. Marco, J. Rodríguez, J. G. Izquierdo, L. Bañares, M. Castillejo. Appl. Surf. Sci. 255 (2009) 5206.

[31] F. Torta, M. Fusi, C. S. Casari, C. E. Botanni, A. Bachi. J. Proteome Res. 8 (2009) 1982.

[32] A. I. Kontos, A. G. Kontos, D. S. Tsoukleris, M. C. Bernadr, N. Spyrellis, P. Falaras. J. Mat. Process. Tech. 96 (2008) 243.

[33] F. Gámez, P. Hurtado, P.M. Castillo, C. Caro, A.R. Hortal, P. Zaderenko, B. Martínez–Haya. Plasmonics. 5 (2010) 125.

[34] A. L. Linsebigler, G. Lu, J. T. Yates Jr.. Chem. Rev. 95 (1995) 735.

[35] F. D. Brandao, M. V. B. Pinheiro, G. M. Ribeiro, G. Medeiros–Ribeiro, K. Krambrock. Phys. Rev. B. 80 (2009) 235204.

[36] N. Kopidakis, N. R. Neale, K. Zhu, J. van de Lagemaat, A. J. Frank. Appl. Phys. Lett. 87 (2005) 202106.

[37] L. A. Lyon, J. T. Hupp. J. Phys. Chem. B. 103 (1999) 4623.

[38] R. Sprycha. J. Col. Interface Sci. 102 (1984) 173.

[39] M. Kosmulski, J. B. Rosenholm. J. Phys. Chem. 100 (1996) 11681.

[40] K. Bourikas, T. Hiemstra, W. H. Van Riemsdijk. Langmuir. 17 (2001) 749.

[41] M. Kosmulski. Adv. Coll. Interf. Sci. 99 (2002) 255.

[42] M. Kosmulski, J. B. Rosenholm. J. Coll. Interf. Sci. 248 (2002) 30.

[43] W. Piasecki, W. Rudzinski, R. Charmas. J. Phys. Chem. B. 105 (2001) 9755.

[44] K. A. Venkatesan, N. Sati Sasidharan, P. K. Wattal. J. Radioanal. Nucl. Chem. 222 (1997) 223.

[45] A. R. Hortal, P. Hurtado, B. Martínez-Haya, A. Arregui, L. Bañares. J. Phys. Chem. B. 112 (2008) 8530.

Chapter 4

Conclusions and Perspectives

Previous chapters have been devoted to describe laser mass spectrometry techniques focused on 1) the study of experimental conditions favouring non-covalent supramolecular complexes of π character, and 2) on the nanoparticle-mediated laser desorption ionization for the determination of polymers and prototype analytes of biological interest. The main conclusions obtained can be summarized in the following:

• Fragmentation and aggregation studies of polyaromatic hydrocarbons (PAH) under pressure–controlled LDI mass spectrometry have been carried out. With the help of a genetic algorithm specially programmed for high resolution mass spectrometry data analysis, the relative populations of covalent and non-covalent aggregates and the main fragmentation channels can be inferred. This aggregation/fragmentation behavior upon differential pressure condition in the ion source depends on the molecular architecture (aromatic condensation and symmetry of the PAH). Island-like polyaromatics are less fragmentative than archipelago-type ones. Nevertheless, C-H cleavage is efficient in all cases and drives the in-plume covalent polymerization of the PAHs.

• Asphaltenes display a LDI response similar to that of the island PAHs and are therefore expected to have an average molecular architecture of such type.

• Gold nanoparticles performance in assisting laser desorption/ionization of a polydispersed synthetic polymer (polyethylene glycol, PEG) has been probed. Ionization thresholds as a function of the between laser wavelength and plasmonic absorption from the UV to the near infrared ranges have been characterized together with the influences of the chemical cover of the particles. The broad plasmonics band of gold nanorods and nanostars make of them perfect candidates for being employing for practical purposed in a wide range of laser emission.

• We have demonstrated that TiO_2 substrates produced by Pulsed laser deposition are robust enough films for laser desorption/ionization applications. The model tripeptide (GlyHisGly) and polydispersed mixture of PEG employed as model adsorbates demostrate that the best LDI properties are achieved with anatase PLD films fabricated under nanosecond radiation frequency and with amorphous PLD substrates obtained with femtosecond lasers due to the smaller nanoparticle sizes and a reduced presence of particulates on the surface of these samples.

• The LDI molecular weight distributions of the polymers produced by both types of nanoparticle substrates is shifted to smaller masses with respect to the nominal distribution of the polymer standard. This observation can be interpreted as following from the stronger adsorption of the longer polymer chains to the nanoparticles, due to the larger number of binding sites present in the polymer backbones.

• The group is currently devoted in the extension of these results to platinum nanoparticles synthesized by laser ablation and chemical reduction, rare earth nanocristalline oxides as well as PLD films of other type of semiconductor as ZnO.

• The MALDI apparatus at UPO described in the introduction is currently undergoing qualitative modifications. The ionization source is of own-design and can be adapted to specific spectroscopic experiments. In fact, although not included in the memory, successful results on ion detection have been obtained by coupling the LDI plume with perpendicular supersonic expansions. Such a set up will allow to control the internal temperature of the desorbed species and to modulate the fragmentation and aggregation pathways of the molecular species under study.

Part II

Molecular Spectroscopy of Gas Phase Complexes

Chapter 5

Introduction

5.1 Crown-ether and cyclodextrine as macrocycle models

A thorough comprehension of paramount model systems is of primary need for understanding events occurring in related but more complex environments. The wide energetic and conformational landscapes typical of supramolecular systems generally makes unaffordable an in-depth theoretical calculation capable of giving an explanation of molecular recognition processes from an atomistic point of view. Native crown ethers and cyclodextrines stay within the limits of usual computational resources and hence constitute a valuable reference for these phenomena. Whereas the full relevance of macrocyclic molecules belongs to aqueous media, the elucidation of gas phase properties serves to discern the intrinsic molecular interactions and conformational constraints from solvent effects. Modern experimental techniques also provide tools for constructing the conformational pathway from gas-to-solution by sequential addition of solvent molecules to a given supramolecular system.

Given the practical importance of polyethers, and in particular of crown ethers, in catalysis and separation technology and in supramoelcular science in general, their cationic complexes have been extensively investigated since the nineties with both experimental and theoretical approaches [1, 2, 3, 4, 5, 6, 7]. The complexes formed by the native crown ethers 12-crown-4, 15-crown-5 and 18-crown-6 (depicted in Fig. 5.1) with alkali metal cations have been often chosen as benchmark systems. Armentrout employed ion beam and collisional fragmentative methods and found an enhancement of the crown-cation binding energy with growing crown ether size and decreasing cation size (*i.e.*, $Li^+ > Na^+ > K^+ > Rb^+ > Cs^+$). These results were in qualitative agreement with the relative stabilities obtained in early infrared multiphoton dissociation experiments (IRMPD) by Eyler and coworkers and have been corroborated in recent FT-ICR-MS experiments by Dearden and coworkers [8]. Complementary to those studies, Bowers and coworkers explored the conformations of the crown-alkali complexes with ion mobility chromatography. They postulated that each complex displays a single type of structure, with a cross section increasing with cation size as a consequence of a less efficient inclusion of the metal inside the cavity. Contrary to the gas-phase findings, in aqueous solution the native crown ethers undergo preferential complexation with specific cations of the alkali series. For instance, the 18-crown-6 ether shows preferential binding in the order $K^+ > Rb^+ > Cs^+ > Na^+ > Li^+$.

In this thesis, the study of crown ether complexes focuses mainly on the effects introduced by cationic charges greater than unity. Hence, the complexes with the alkaline-earth series and with divalent transition metals are considered. Ion-dipole interactions largely control the coordination network built between the cation and the oxygen atoms of the ether ring. The flexibility of the ether ring itself is also of significant relevance and our investigation will show how the crown ether adopts arrangements of different symmetry to optimize the binding of the cation.

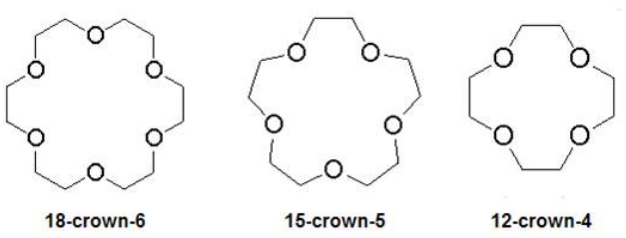

Figure 5.1: Schematic representation of the crown ethers considered in the work.

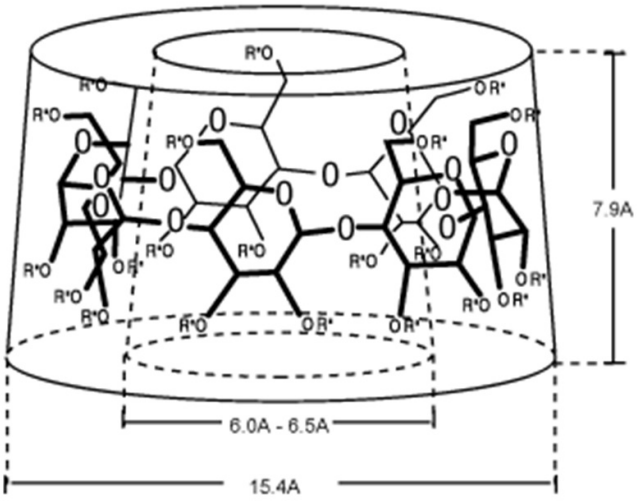

Figure 5.2: Geometrical features of native cyclodextrines from [**?**]

For his part, cyclodextrins (CD) are cyclic oligomers based on α-D-glucopyranosyl units linked with α-(1→4)-glycosidic bonds. The most common native cyclodextrines are made of six (α-CD), seven (β-CD) or eight (γ-CD) glucose units. The three-dimensional architecture of the CD macrocycle is of tronco-conical geometry, with a larger (secondary) and smaller (primary) openings dressed by one -CH_2OH or -OH hydroxylic group per glucose ring, respectively. The general structure and geometrical features of the native α–CD is depicted in Fig. 5.2 While the two outer rims of the CD are polar, in aqueous solution the inner part of its cavity provides a perfect environment to host hydrophobic moieties with appropriate steric interactions.

It will be shown that cationic guests tend to coordinate with the primary hydroxyl groups of the native

cyclodextrines. In doing so, the cation must disrupt the highly H-binding network built between hydroxyl groups in the free CD molecule [9, 10]. The present investigation intend to determine the binding location of the alkali cations as well as the rearrangement of the CD host as a function of the size of the guest cation. Gas phase studies of cyclodextrines are much more scarce than those of crown ethers. We are aware of the experimental work (combining MALDI and ion mobility approaches) on the structure of cationic complexes by Lee et al [11], of mass spectrometry experiments on equilibrium and stabilization of cationized CD in solution with both atomic and molecular guests as aminoacids [12, 13, 14], as well as theoretical work comparing alkali-CD complexes in both solvent and solution [15]. These studies are however inconclusive with respect to key aspects related to the conformation of the complexes and to the relative alkali cation affinities of the native CDs.

5.2 Gas phase spectroscopy

The rapid development of spectroscopic techniques in recent years has made possible to unveil the detailed coordination networks built in different inclusion complexes. The combination of the experiments with *ab initio* calculations allows to rationalize the roles played by the key properties of the molecules involved. The main goal of this second part of the thesis has been to provide new insights into the intrinsic features of crown ethers and cyclodextrins that determine their behavior as inclusion substrates. For this purpose, two state-of-the-art techniques have been employed, namely microwave rotational spectroscopy and infrared multiphoton dissociation vibrational spectroscopy. The experiments have been carried out in collaboration with specialized groups at Universidad de Valladolid (S. Blanco, J.C. López and J.L. Alonso) and at the dutch FOM-Rijhuizen Institute (J. Oomens).

High resolution microwave spectroscopies is probably the best route to obtain detailed structural features of small dipolar molecules. In essence, in this experiments a microwave pulse excites internally cooled isolated molecules generated in a supersonic expansion. The free induction decay is monitored and Fourier-transformed to the frequency–domain. The observed line progressions are fitted to assigned sets of rotational constants to single conformers of the species under study. In the IRMPD approach, mass-selected ions are stored in an Ionic Cyclotron Resonance (ICR) The IRMPD spectrum reflects the fragmentation yield induced upon laser irradiation of the ions. Typically high laser energy fluxes (from optical parametric oscillators or from a free electron laser) interact with the ions leading to the sequential and noncoherent absorption of multiple photons mediated by a rapid intramolecular vibrational redistribution of the excitation energy. Experimental details of both techniques are given in the following sections.

5.2.1 Molecular–Beam Fourier Transform Microwave Spectrometer.

EXPERIMENTAL

The present microwave spectroscopy (MW) measurements were performed in the laboratory of the group of molecular spectroscopy at Universidad de Valladolid led by prof. J.L. Alonso. A photograph of the equipment is provided in Fig. 5.3 . The development of the MW technique has followed a long history. Flygare introduced the microwave pulse excitation techniques in the time domain [16]. Molecular beams used in pulsed heatable nozzles were the next step in the overall improvement of the resolution and sensitivity [17]. Later on, Dreizler brought the technique to sub-Doppler resolution [18] by incorporating a coaxial arrangement of the molecular beam and the Fabry–Perot resonator axis. This configuration leads to the observation of a Doppler doublet for each transitions so that the central transition frequency is determined from the half-sum of the two doppler components. The overall measurement cycle proceeds as follows. The supersonic expansion cools the internal energy of the molecules and brings them into to the Fabry-Perot resonator under high vacuum. The molecular cooling achieved depends on the adiabatic constant of the gas, on the difference of pressure along the nozzle and on the nozzle temperature. While the different conformers tend to relax to low rotational states and to the lowest vibrational level, conformational relaxation itself is much less efficient. Consequently, very often the conformers roughly retain the equilibrium relative populations associated with the nozzle temperature.

By the time that the molecules enter the MW resonator, collisions have ceased and a beam of virtually isolated molecules has been formed [19]. At this point, the spectroscopic procedure begins. One of the mirrors of the resonator is mobile, and permits to control the polarization frequency. It has an antenna connected to a Fourier–transform spectrometer that both polarizes the jet and detects the free induction decay (FID). This spectrometer consists basically in a microwave synthesizer that can be alternatively directed to the polarization and detection branches. Once the excitation pulse polarizes the jet, a time delay is allowed before detection branch is opened to permits extinction of the stored energy of the cavity. The weak FID emission is amplified and superheterodinally down-converted to detectable radiofrequency signal. The FID if finally Fourier–transformed to frequency domain.

ANALYSIS OF THE ROTATIONAL LINE

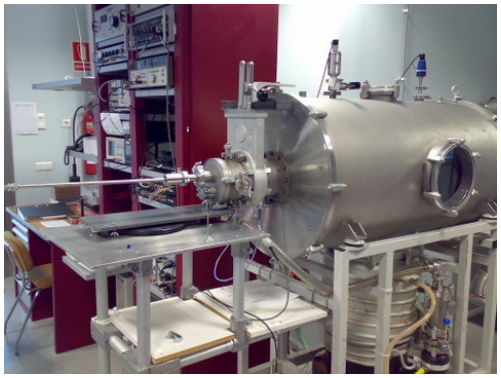

Figure 5.3: The Molecular Beam Fourier Transform Mass Spectrometer employed in the present investigation

PROGRESSIONS

The solution of the Schrödinger equation for the rigid symmetric rotor is based on the commutative properties of the rotational hamiltoninan with the set of angular momentum operators $(\widehat{\mathbf{J}}^2, \widehat{\mathbf{J}}_z)$. The quantum numbers (J, M) are the relevant parameters for the rotational transitions for the spherical rotor. As this type of rotational spectroscopy is a single-photon process, the usual selection rules apply: $\Delta J = \pm 1$ and $\Delta M = 0, \pm 1$.

For a general tridimensional rotor, one can write the rotational hamiltoninan in terms of both laboratory frame and molecular frame axis. Let us follow the second choice and label the principal moments of inertia with the following convention: $I_a \leq I_b \leq I_c$ The rotational hamiltonian for the asymmetric rotor commutes with $(\widehat{\mathbf{J}}^2, \widehat{\mathbf{J}}_z)$ but in general not with $\widehat{\mathbf{J}}_c$. For an asymmetric top, two general types of limiting mass distributions are possible, namely the oblate rotor ($I_a = I_b < I_c$ and the prolate rotor ($I_a < I_b = I_c$). A proper choice of the hamiltonian leads to a complete set $(\widehat{\mathbf{J}}^2, \widehat{\mathbf{J}}_{b,c})$ of operators that permits to solve the energy levels from the Shrödinger equation as a function of a new quantum number K. This number is indexed as K_{-1} and K_{+1} for the oblate and prolate tops, respectively. This formalism does not longer hold for the general case where $I_a \neq I_b \neq I_c$, and the variational method is usually employed to determine the energy levels. This method expands the assymetric wavefunction in terms of test symmetric wavefunctions. The energy levels are always between the limits of the prolate and oblate asymmetric tops. Thus, it is common to label the rotational transitions with the corresponding quantum numbers K_{-1} and K_{+1} of the associated asymmetric tops. The asymmetry Ray parameter $\kappa = \frac{2B-A-C}{A-C}$ gives and idea of how far are we from the oblate ($\kappa = 1$) or prolate ($\kappa = -1$) limits. Within this framework, the selection rules for the tridimensional rotor also depend on the value of the electric dipole moment components μ_i along the principal axis of inertia:

- For all transitions $\Delta J = 0, \pm 1$ for the Q, P and R branches respectively.
- For μ_a type transitions $\Delta K_{+1} = 0, \pm 2, \pm 4...$ and $\Delta K_{-1} = \pm 1, \pm 3, \pm 5...$
- For μ_b type transitions $\Delta K_{+1} = \pm 1, \pm 3, \pm 5...$ and $\Delta K_{-1} = \pm 1, \pm 3, \pm 5...$
- For μ_c type transitions $\Delta K_{+1} = \pm 1, \pm 3, \pm 5...$ and $\Delta K_{-1} = 0, \pm 2, \pm 4...$

The set of rotational transitions are fitted using a numerical iterative procedure based on Levenberg–Marquardt algorithm [20]. Besides the principal rotational constants, centrifugal distortion coefficients must also be included to match the experimental line progressions [21, 22]. The common Watson's hamiltonian for a asymmetric rotor is chosen to represent the rotational energies [22]. It consists in an expansion in terms of the angular momentum operator set in the laboratory frame $(\widehat{\mathbf{J}}^2, \widehat{\mathbf{J}}_z^2, \widehat{\mathbf{J}}_\pm)$ with $\widehat{\mathbf{J}}_\pm = \widehat{\mathbf{J}}_x \pm \widehat{\mathbf{J}}_y$. In the present work, the asymmetric reduction of Watson´s hamiltoninan has been employed, which leads to the following expression for the rotational energies, up to quartic order in centrifugal distortion coefficients (greek symbols):

$$\widehat{H}^A = B_x^A \widehat{\mathbf{J}}_x^2 + B_y^A \widehat{\mathbf{J}}_y^2 + B_z^A \widehat{\mathbf{J}}_z^2 - \Delta_J (\widehat{\mathbf{J}}^2)^2 - \Delta_{JK} \widehat{\mathbf{J}}^2 \widehat{\mathbf{J}}_z^2 - \\ - \Delta_K \widehat{\mathbf{J}}_z^4 - \frac{1}{2}\left(\delta_J \widehat{\mathbf{J}}^2 + \delta_K \widehat{\mathbf{J}}_z^2 \widehat{\mathbf{J}}_+^2 + \widehat{\mathbf{J}}_-^2\right) \quad (5.1)$$

Moreover, the fitting of the experimental lines can be performed in six different representations, according to the identification between the cartesian coordinates and the principal molecular axii $(x, y, z) \leftrightarrow (a, b, c)$. In this work, the I^r (with $(x, y, z) \leftrightarrow (b, c, a)$) and the III^l (with $(x, y, z) \leftrightarrow (a, c, b)$). The best choice of the hamiltonian reduction and representation for a given system is not always predictable. Nevertheless, a general rule is that I^r works well for prolate conformations while III^l seems to perform better for oblate conformers [23].

5.2.2 Infrared Multiple Photon Dissociation Spectrometry (IRMPD)

EXPERIMENTAL SETUP

The IRMPD experiments of this thesis were performed at the Free-electron laser facility (FELIX) of the FOM Rijhuizen Institute in Nieuwegein (Holland), in collaboration with the principal investigator of the ion FT-ICR beamline, Jos Oomens. Our group had access to this facility through several competitive projects that granted us a total of about fifteen eight-hour shifts for measurements.

In the FT-ICR beamline the ions are generated in a electrospray source using salt/host solutions in water/methanol 1:1 solvent. Molecular ions coming out

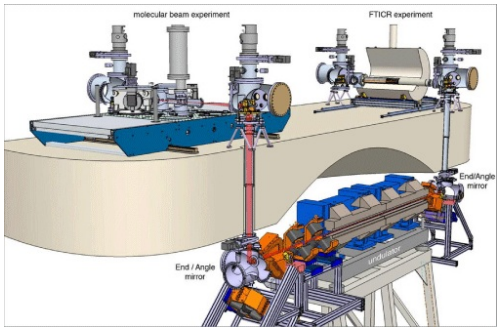

Figure 5.4: Schematic view of the FELIX setup for IRMPD experiments.

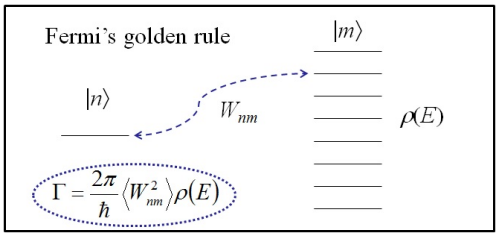

Figure 5.5: Schematic view of the Intramolecular Vibrational Redistribution. See text for details

of the ESI source are accumulated in an hexapole trap in order to inject them in pulses into the ICR cell where they will interact with the laser light. The ICR cell is essentially a Penning-like trap operated under a high magnetic field and a specially homogeneous electric field that excites the ions inducing a cyclotron trajectory. The free induction decay signal is recorded as the image current caused by the charges moving in such trajectories and is finally Fourier-transformed to obtained the useful mass spectrum. Once the ions are stored in the ICR, an Stored waveform inverse Fourier transform (SWIFT) is applied to select a desired precursor mass. The isolated ions are then excited with the infrared laser, in our case the free electron laser FELIX. The general setup of the FELIX facility is sketched in Fig. 5.4 [24].

In a free-electron lase, packets of unbound electrons of a few picoseconds duration are accelerated up to relativistic speeds through radiofrequency generators and injected into a periodic magnetic wiggler. The oscillatory trajectories of the electrons in the wiggler leads to the generation of weak synchrotron radiation. This radiation is converted into strong laser pulses in a resonator cavity. The emission wavelength is tuneable by means of changes in the magnetic field in the wriggler.

A BRIEF BACKGROUND ON IRMPD SPECTROSCOPY

IRMPD is a form of action spectroscopy in which resonant photon absorption leads to fragmentation of the ionic species. Hence, an IRMPD spectrum is recorded by monitoring the yield of ionic fragments as the laser wavelength is scanned through the vibrational mode transitions of the species of interest. The IRMPD mechanism is based on the non-coherent absorption of multiple photons by a molecular ion. In between the absorption of consecutive, the vibrational energy initially stored in the single mode excited by the laser (or in a few modes if a combination band is excited) is rapidly redistributed through anharmonic coupling among the rest of modes of the molecule. This general process is known as intramolecular vibrational redistribution (IVR)[25]. For molecules of moderate size, the time scale for IVR is much smaller than the duration of the laser excitation pulse, so that many photons may be sequentially absorbed [26]. Fragmentation occurs when the total internal energy stored by the chemical species becomes high enough as to break any of the covalent or non-covalent bonds present in the system.

Because of the short time scale of the IVR process, it is possible to apply Fermi's Golden rule to determine the transition rate from the excited vibrational state to the continuum of states provided by the rest of the vibrational modes as shown in Fig. 5.5. This rate is then given by $\Gamma = \frac{2\pi}{\hbar}\langle W_{nm}^2 \rangle \rho(E)$, and depends on the density of states, $\rho(E)$, and the squared anharmonic coupling matrix elements W_{nm}. Although the density of states can be modelled with reasonable accuracy [27], the knowledge of the matrix coupling elements requires the calculation of the intramolecular potential energy surface (PES) to search for intermediate resonant states [28] and large amplitude [29] and extreme motions [30]. The use of different approximations in this latter procedure can modify the predictions for Γ by several orders of magnitude.

5.3 Quantum chemistry calculations.

Quantum chemical calculations are required in order to take full advantage of the information provided by the vibrational IRMPD spectrum. The computations provide a rank of low energy conformers whose IR spectra should be compared to experiment in order to determine their relative population. In this section, a brief description of the computational methodology employed in this work is outlined.

1) Firstly, simulated annealing (SA) runs are performed to obtain an ensemble of low energy conformers. This method achieves an efficient sampling of stable molecular conformations by means of random geometrical changes (bonds and angles) that are accepted or neglected depending of their energy changes and the

system temperature. Heating and cooling cycles are performed in order to avoid the trapping of the system in local energy minima.

2) The minimum energy structures obtained in the SA step are reoptimized with a proper quantum method and electronic basis set. Methods employed in this work include *ab initio* Hartree–Fock and Density Functional Theory and also MØller–Plesset perturbation theory. A brief summary of these methods is given in the following.

Hartree–Fock method simplifies the non-relativistic electronic hamiltonian given by the kinetic term $-\frac{h^2}{2m}\sum_i \nabla_i$, interelectronic and electron–nucleus (denoted as α) as

$$\widehat{H} = -\frac{h^2}{2m}\sum_i \nabla_i - \sum_\alpha \sum_i \frac{Z_\alpha e^2}{r_{i\alpha}} + \sum_i \sum_{j>i} \frac{e^2}{r_{ij}} \quad (5.2)$$

by means of neglect the last term corresponding to interelectronic interaction. The second approximation is to suppose that the shape of electronic molecular wavefunction would be similar as if this term were not taken into account. Then, the spin orbitals are chosen to be given by a simple Slater determinant built from a product of monoelectronic wavefunctions [31]

$$\Psi = \frac{1}{N!}\left|\psi_1(1), \psi_2(2)...\psi_n(n)\right| \quad (5.3)$$

The expression of the hamiltonian contains two kinds of terms. The first two terms correspond to one-electron energies (kinetic plus electrostatic electron-nucleus attraction), while the second one is the interelectronic interaction. Applying the properties of expectation values of mono- and bielectronic operators it is possible to demonstrate that these terms can be split in a direct or Hartree-Fock or Coulomb (J) energy and a exchange energy (K) given by:

$$J\left[\psi_1...\psi_N\right] = -\frac{e^2}{2}\sum_{i,j=1}^{N}\left\langle\psi_i\psi_j\left|\frac{1}{r_{ij}}\right|\psi_i\psi_j\right\rangle \quad (5.4)$$

$$K\left[\psi_1...\psi_N\right] = -\frac{e^2}{2}\sum_{i,j=1}^{N}\left\langle\psi_i\psi_j\left|\frac{1}{r_{ij}}\right|\psi_j\psi_i\right\rangle \quad (5.5)$$

Applying Lagrange multipliers method to the Hartree-Fock energy so obtained, it is possible to demonstrate that

$$\widehat{F}_i\psi_i(i) = \varepsilon_i\psi_i(i) \quad (5.6)$$

which are known as Hartree–Fock equations, where the Fock operator contains both one- and two-electron energies (including exchange corrections) and ε_i is the energy of the spin orbital. Correlation among electrons can be taken into account in two main manners:

1).- The Kohn-Sham method maps the multilelectron interacting problem to an equivalent system of noninteracting electron with the same electron density, whose wavefunction would be a Slater function [32]. Basically, a correlation energy appears and the corresponding spin orbitals that fulfill the abovementioned condition are called Kohn-Sham orbitals. However, as Coulomb, exchange and correlation operators can be rewritten in term of the electron density

$$n(\mathbf{r}') = N\sum_i^N \int d^3r_2... \int d^3r_N \Psi^*\delta(\widehat{\mathbf{r}}_i - \mathbf{r})(\mathbf{r})\Psi(\mathbf{r}) \quad (5.7)$$

which is a three dimensional function more handle than the wavefunction itself (that depends on 3 times the number of electrons in the system), the problem becomes a little bit simplified. The main problem is now to obtained a tractable expression for the correlation functional. Many functionals and hybrid functionals that construct the molecular energy by mixing Hartree–Fock functionals and DFT theory are available in common software packages and their description is beyond of the scope of the present section [33]. We mention in passing that the usual strategy to obtain such functionals is to calculate the correlation and exchange energy per electron in a homogeneous electron gas of density n employing Monte Carlo methods and then obtained the energy of the overall system by integration over the whole space. This is the case of the hybrid three parameters of Becke (B3LYP) in which the energy functional is corrected local spin density approximation (LSDA) [34].

2).- Employing perturbation theory as Møller-Plesset theory (MP) or other post-Hartree-Fock methods. In MP theory the zeroth-order wave function is an exact eigenfunction of the Fock operator, which thus serves as the unperturbed operator. The added perturbation serves to correct the HF energy.

Up to now, we have sketched some possibilities to outlined the energy of a molecular system. But a question still raise. What is the shape and number of wavefunctions needed for such calculations (the so-called basis-set)? In the historical linear combination of atomic orbitals-molecular orbitals (LCAO-MO) the molecular wavefunction is ocnsidered as a linear combination of atomic orbitals. The simpler choice due to the similutude with hydrogen-type orbitals are the Slater orbitals:

$$\phi_{nlm}^{STO}(r,\theta,\varphi) = \sqrt{\frac{(2\zeta)^{2n+1}}{4\pi(2n)!}}r^{n-1}\exp\left(-\zeta r\right)Y_{lm}\left(\theta,\varphi\right) \quad (5.8)$$

with Y_{lm} being a spherical harmonic and ζ is a constant related to the screening charge of the nucleus. However, the use of Slater functions have the problem that the integrals involved in calculations become lengthy. The use of gaussian functions would solve this problem by the price of a non realistic treatment of at short distances. This can be overcome with the use of contracted gaussian function which are of the form:

$$\psi_{lm} = r^l Y_{lm}(\theta, \phi) \sum_{\mu} a_{\mu l} \exp\left(-\beta_\mu r^2\right) \tag{5.9}$$

with $a_{\mu l}$ the contraction coefficients selected to give a correct near-origin behavior and β_μ is an element–tabulated parameter of the primitive gaussians . Additional diffuse and polarization functions can be added. The first ones are simply GTO with small exponent that decay slowly with the distance from the center. The second ones are GTOs of higher angular momentum than those present in occupied atomic orbitals for the corresponding atom. It means that it includes vacant-like orbitals which is important to describe chemical bonding. With all this in mind, Pople's notation indicates the basis set as n-ijk+(+)G** where n indicates de number of primitives employed for the inner shell, ij(k) the sets of double (triple) zeta schemes (i.e. two or three primitives per orbital) and *(*) or +(+) the use of polarization and diffuse functions in heavy (or all) atoms. In some cases and in order to reduce computational cost, effective core potentials (ECP)are used in heavy atoms to take into account relativistic effects. When dealing with ECP, only the valence electrons are treated with Pople's basis-set.

Once a minimum energy structure has been established, the infrared spectrum is calculated as -numerical or analytical- second derivatives of the energy respect nuclear coordinates. The resulting spectra is the result of the convolution of the ensemble of normal modes centered in ω_0.

Bibliography

[1] M.B. More, D. Ray, P.B. Armentrout, J. Am. Chem. Soc. 121 (1999) 417.

[2] P.B. Armentrout, Int. J. Mass Spectrom. 193 (1999) 227.

[3] D. Feller, J. Phys. Chem. A 101 (1997) 2723.

[4] D.M. Peiris, Y. Yang, R. Ramanathan, K.R. Williams, C. Watson, J.R. Eyler, , Int. J. Mass Spectrom. Ion Processes 157/158 (1996) 365

[5] J.D. Anderson, E.S. Paulsen, D. Dearden, Int. J. Mass Spectrometry 227 (2003) 63.

[6] S. Lee, T. Wyttenbach, G. von Helden, M.T. Bowers, J. Am. Chem. Soc. 117 (1995) 10159.

[7] T. Wyttenbach, G. von Helden, M.T. Bowers, Int. J. Mass Spectrom. Ion Processes 165/166 (1997) 377.

[8] D. Anderson, E.S. Paulsen, D. Dearden. Int. J. Mass Spectrom. 227 (2003) 63.

[9] C. P. A. Anconi, C. S. Nascimento, J. Fedoce-Lopes, H. F. Dos Santos, W. B. De Almeida, J. Phys. Chem. A. 111 (2007) 12127.

[10] A. Karpfen, E. Liedl, W. Snor, P. Weiss-Greiler, H. Viernstein, P. Wolschan. J. Incl. Phenom. Macrocycl. Chem. 57 (2007) 38.

[11] S. Lee, T. Wyttenbach, M. T. Bowers. Int. J. Mass Spectrom. Ion Process. 167/168 (1997) 605.

[12] L. C. Ngoka, J. Gal, C. B. Lebrilla. Anal. Chem. 66 (1994) 692.

[13] S. Reale, E. Texeidò, F. de Angelis. Annali di Chimica. 95 (2005) 375.

[14] K. P. Madhusudanan. J. Mass Spectrom. 38 (2003)409.

[15] Y. Fu, L. Liu, Q. Guo. J. Incl. Phen. Mac. Chem. 43 (2002)223.

[16] a) T. J. Balle, W. H. flygare. Rev. Sci. Instrum. 52(1) (1981) 33; b) E. J. Campbell, L. W. Buxton, T. J. Balle, M. R. Keenan, W. H. Flygare. Rev. Sci. Instrum. 74(2) (1981) 829.

[17] M. D.Harmony, K. A. Beran, D. M. Angst, K. L. Ratzlaff. Rev. Sci. Instrum. 66 (1995) 5196.

[18] J. U. Grabow, W. Stahl, H. Dreizler. Rev. Sci. Instrum. 67(12) (1996) 4072.

[19] D. H. Levy. Science 214-4518 (1981) 263.

[20] http://www.ifpan.edu.pl/ kisiel/prospe.htm

[21] a) E. B. Wilson, Jr. und J. B. Howard. J. Chem. Phys. 4 (1936) 260; b) E. B. Wilson, Jr. J. Chem. Phys., 4 (1936) 526; c) E. B. Wilson, Jr. J. Chem. Phys. 5 (1937) 617; d) D. Kivelson, E. B. Wilson. J. Chem. Phys. 20(10) (1952) 1575; e) D. Kivelson, E. B. Wilson, Jr. J. Chem. Phys. 21 (1953) 1229.

[22] a) J. K. G. Watson. J. Chem. Phys. 46(5) (1967) 1935; b) J. K. G. Watson, J. Chem. Phys. 48 (1968) 4517; c)J. K. G. Watson, "Aspects of Quartic and Sextic Centrifugal Effects on Rotational Energy Levels" in "Vibrational Spectra and Structure", J. R. Durig (Ed.), Vol. 6, Elsevier, Amsterdam, 1977.

[23] L. Margulès, R. A. Motiyenko, E. A. Aleksev, J. Demalson. J. mol. Spectrosc. 260 (2010) 23.

[24] http://www.differ.nl/en/research/guthz/felice.

[25] K.K.Lehmann, G. Scoles, B. H. Pate, annu. Rev. Phys. Chem 45 (1994) 241.

[26] M. Bixon, J. Jortner. J. Chem. Phys. 48 (1986) 715.

[27] D. Romanini, K. K. Lehmann. J. Chem. Phys. 98 (1993) 6437.

[28] A. A. Stuchebrukhov, R. A. Marcus. J. Chem. Phys. 98(9) (1993) 6004.

[29] G. A. Bethardy, X. Wang, D. S. Perry. Can. J. Chem. 72 (1994) 652.

[30] J. E. Gambogi, J. T. Timmermans, K. K. Lehmann, G. Scoles. J. Chem. Phys. 99 (1993) 9314.

[31] J. C. Slater. J. Chem. Phys. 1 (1933) 687.

[32] W. Kohn, L. J. Sham. Phys. rev. 140 (1957) 364.

[33] a) D. E. Woon, T. H. Dunning. J. Chem. Phys. 100 (1994) 2975; b) R. M Dreizler, E. K. U. Gross. Density Functional Theory: an approach to the quantum many body problem. Springler, Berlin, 1990; c) W. Koch, M. C. Holthausen. A Chemist‘s guide to Density Functional Theory. Wiley, Heidelberg, 2001; C. Fiolhais, F. Nogueira, M. Marques. A primer density functional theory Springer, Berlin; New York, 2003.

[34] a) A.D. Becke. J. Chem. Phys. 98 (1993) 1372; b)A.D. Becke. J. Chem. Phys. 98 (1993) 5648;A.D. Becke. Phys. Rev. A. 38 (1988) 3098.

Chapter 6

Microwave Spectroscopy and Quantum Chemical investigation of eight low energy conformers of the 15–crown–5 ether

Crown ether macrocyles constitute a central class of selective substrates in Supramolecular Chemistry. The backbone of crown ethers is particularly flexible which makes the spectroscopic and computational investigations challenging. In this chapter, we present a systematic investigation of the low energy conformational landscape of the benchmark macrocycle 15–crown–5 ether (15c5) under isolated conditions. Molecular beam Fourier transform microwave spectroscopy is employed to measure a broad ensemble of rotational transitions within the range 4-11 GHz. The recorded spectra allows to determine the rotational constants of eight individual 15c5 rotamers which are identified among the nine lowest energy conformers predicted by the *ab initio* MP2 computation. The results illustrate well the variety of conformers of prolate and oblate character that the 15c5 molecule displays within a narrow range of energies. Implications for the supramolecular behavior of 15c5 are discussed.

6.1 Introduction

The Supramolecular Chemistry of inclusion complexes has largely developed around distinct classes of macrocycles and cryptands, such as crown ethers, cyclophanes, calixarenes, cyclodextrins or cucurbiturils [1]. Among them, crown ethers display one of the simplest cavity structure, which is made of a polyether ring with eventual substituents [2]. The basic backbone of the crown ether ring is also particularly floppy in comparison with other types of macrocycles. This leads to a conformational potential energy hypersurface with numerous low energy wells that is challenging for both experimental and computational studies. This scenario demands for experimental methods that elucidate the relevant molecular structures with sufficient accuracy.

In order to face this problem from first principles, different groups have probed the most stable conformers of isolated crown ethers and their cationic complexes by means of gas–phase spectroscopic techniques [3, 4, 5, 6, 7, 8, 9, 10, 11, 12, 13, 14, 15, 16, 17]. Gas phase studies have the fundamental advantage of leading to benchmark structural information that can be put into direct relation with quantum chemical computations [18]. This approach provides a valuable insight into the interplay between the intra– and intermolecular interactions, the intrinsic flexibility of the ether ring and potential solvent effects. In this way, the study of the conformational features of isolated crown ethers also constitutes a valuable step towards the elucidation of the microscopic mechanism governing molecular recognition by these macrocycles.

Our groups have recently initiated a collaborative effort aimed at a systematic investigation of the conformational properties of isolated crown ethers by means of high resolution microwave rotational spectroscopy of jet-cooled molecules [19]. Molecular Spectroscopy in the microwave region provides a highly sensitive tool for the assessment of the molecular structure of individual rotamers through the accurate determination of their rotational constants (*e.g.*, see [20, 21]). For flexible molecules such as crown ethers, internal cooling is essential for spectroscopy in order to confine the rotational population in an ensemble of states as reduced as possible. The use of supersonic expansions provides the required cooling and also leads to a terminal environment of virtual isolation for the molecules in which Doppler and collisional band broadening effects are minimized [**?**]. Also importantly, the conformer distribution before the expansion is to a large extent preserved in the free jet [23], which allows for the spectroscopic interrogation of a broad range of low energy conformers.

In this chapter, we present an extensive rotational spectroscopy investigation of the 15–crown–5 ether. As many as eight conformers are unequivocally assigned to structures predicted by *ab initio* MP2 computations, which constitutes an appreciable extension of our preliminary report on this topic in which the three lowest energy conformations were elucidated. This investigation serves to update the comprehension of the conformational landscape of 15–crown–5 provided by previous studies throughout the fifteen years, employing theoretical [24, **?**, 26] and crystallographic [27] techniques.

6.2 Methods

6.2.1 Molecular Beam Fourier Transform Microwave Spectroscopy

The molecular-beam Fourier transform microwave spectrometer employed in this study has been described in detail elsewhere [28]. Briefly, a free molecular jet is formed by heating the 15-crown-5 (Aldrich, 98% purity) at 120°C and producing a supersonic expansion with a Ne seeding gas at high pressure (1.5 bar). The 15c5 molecules are rovibrational cooled in the expansion and fly into the differentially pumped region of the microwave Fabry-Perot resonator defined by two 55 cm confocal spherical mirrors. A short microwave pulse (typically 0.3 μs, 10–300 mW) polarizes the species in the jet and the subsequent coherent transient emission due to molecular decay to equilibrium is then recorded in the time domain. Typically a ca. 400 μs long spectrum is recorded in 40–100 ns intervals. Finally, the frequency domain spectrum is reconstructed with a Fourier transformation of the free-induction decay. For these experiments, the equipment was operated in the frequency range 4-11 GHz.

In a typical experiment, rotational progressions are sought in the microwave spectrum in order to identify signatures for individual conformers. As discussed below in detail, the ensemble of transitions measured within the scope of this investigation has served to characterize as many as eight 15–crown–5 conformers. A list of all those transitions, probing rotational states in the range $J = 4$–16, is provided as Supporting Information in this chapter. Figure 10.4 depicts some illustrative lines of the microwave spectrum of the 15-crown-5 molecule, showing characteristic K_{+1} and K_{-1} doublet patterns. Note that each rotational transition is split into two Doppler components, which due to the collinear arrangement of the jet and the resonator axis in our equipment. The resonant transition frequencies are determined from the half–sum of both components with an accuracy better than 5 kHz. The doublets assigned to conformers II and IX in Figure 10.4 (roman number labels are in order of increasing energy, see below) are well resolved, with only partial overlap between the Doppler line components.

Similar spectral patterns for conformers I and III were represented in ref. [19]. In contrast, the doublet for conformer VI, involving the same quantum numbers as one shown for conformer IX, is degenerated and is observed as a merged Doppler structure. Such degeneration is particularly characteristic of the oblate conformers II, V and VI.

The assignment of the experimental lines to rotational transitions of a specific conformer is performed through a recurrent fit based on Watson's A–reduced semirigid rotor hamiltonian in the I^r representation for the energy levels [30, 29], as implemented in Pickett's software package [31]. This is the usual framework employed for the rotational analysis of prolate or moderate oblate asymmetric tops [29]. Only one out of the eight experimental rotamers considered in this work (the one assigned to conformer II [19], see below) was fitted within the III^l representation due to its marked oblate character [32]. The fit of the experimental lines assigned to each given conformer provides its rotational constants (A, B, C) and quartic centrifugal distortion coefficients (Δ_J, Δ_{JK}, Δ_K, δ_J, δ_K). The related asymmetry parameter (κ= (2B–A–C)/(A–C)) and the planar inertial moments (P_{aa}=(I_b+I_c-I_a)/2, P_{bb}=(I_a+I_c-I_b)/2, P_{cc}=(I_a+I_b-I_c)/2) are commonly employed to characterize the conformers. The asymmetry parameter κ takes positive values for overall prolate structures and negative values for oblate ones. The planar inertial moments P_{aa}, P_{bb} and P_{cc} provide a measure of the mass distribution out of the *bc*, *ac* and *ab* planes, respectively.

6.2.2 Quantum Chemistry calculations

Candidate structures for the isolated 15–crown–5 were generated by exploration of the conformational space via simulated annealing with the Universal Force Field as implemented in the Materials Studio platform [33]. The fifty 15c5 structures of lowest energy were optimized employing Density Functional Theory (DFT) with the functionals B3LYP [34] and M06 [35] and the basis set 6-311++G(d,p). Incidentally, this ensemble of conformers included the most stable structures proposed in previous computational studies [24, 25, 26], as well as two structures derived from crystallography measurements [27]. Finally, the *ab initio* second–order Møller–Plesset MP2 method and the same 6-311++G(d,p) basis set was applied to reoptimize the fifteen most stable conformers, encompassing energy differences within 8 kJ mol^{-1}. In order to check for basis set effects, the three MP2 lowest energy conformers were reoptimized with DFT employing the B3LYP and M06 functionals and the polarized triple Zeta basis set aug–cc–pVTZ. For all these calculations the Gaussian 09 code was used [36].

6.3 Results

Figure 6.2 represents the nine most stable conformers predicted by the MP2/6-311++G(d,p) computation. Table 6.1 lists their corresponding principal rotational constants, asymmetry parameter, dipole moments and relative energies. Roman numerals I–IX are employed as labels in order of increasing MP2 energy. These conformers illustrate well the broad range of prolate and oblate structures that the 15–crown–5 ether can adopt within a narrow range of energies. In fact, the nine conformers considered here span MP2 free energies up to only 3.4 kJ mol^{-1} (287 cm^{-1}).

It is interesting to note that at least four of those conformers, namely conformers III, V, VI and VII had not been described previously. On the other hand, conformers I, II, VII, VIII and IX correspond to conformers 1, 11, 4, 3, and 2 of ref. [**?**], respectively. Furthermore, conformer IV resembles one of the crystalline structures from ref. [27] and is also coincident with conformer 9 of ref. [26].

The overall microwave spectrum recorded for the 15–crown–5 molecule in this study identifies eight individual rotameric structures of the ring. Our recent preliminary report focused on conformers I, II and III [19]. Here, the best–fit rotational constants for all eight experimental rotamers are listed together in Table 6.2. From those constants, the rotamers can be unequivocally related to eight out the nine *ab initio* MP2 conformers of Fig. 6.2, with the exception of conformer VII. No signature for this latter conformer was found in the experiment and possible reasons for this are discussed below. The assignment was also corroborated by the fact that the type and relative intensities of the observed lines for each conformer were fully consistent with the components of the dipole moment predicted by the computation that are given in Table 6.1. Hence, the transitions dominant in intensity in the microwave spectrum were of type–*a* for conformers II and V and of type–*b* for the rest of conformers. Type–*c* transitions were only measured in our survey for conformers I, III, IV and VIII.

A general feature common to all the 15–crown–5 conformers is a stretched backbone structure associated with a large moment of inertia with respect to the principal axis perpendicular to the ring. This reflects itself as a correspondingly small value for the rotational constant C of all the conformers. In addition, the small values of the planar moment of inertia P_{cc}, giving the mass extension out of the *ab* inertial plane, indicate that the heavy atoms lie at positions not far from that plane.

The stretched open ring conformations adopted by the free crown ether can be related to a demand imposed by

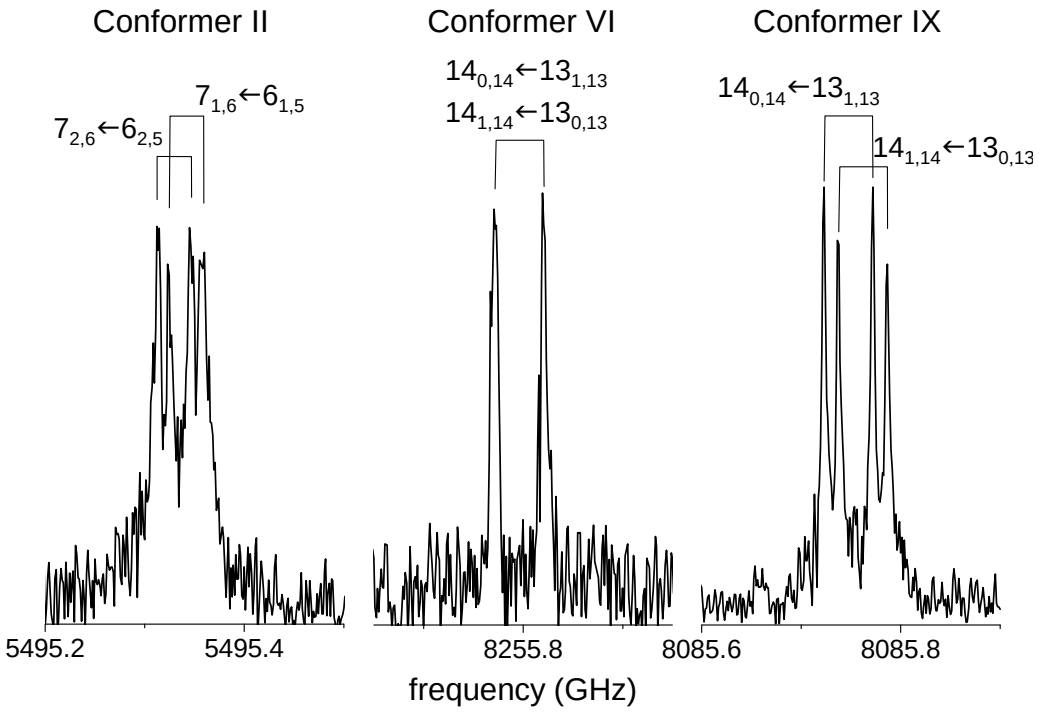

Figure 6.1: Typical rotational lines observed in the microwave spectrum of the 15-crown-5 molecule.

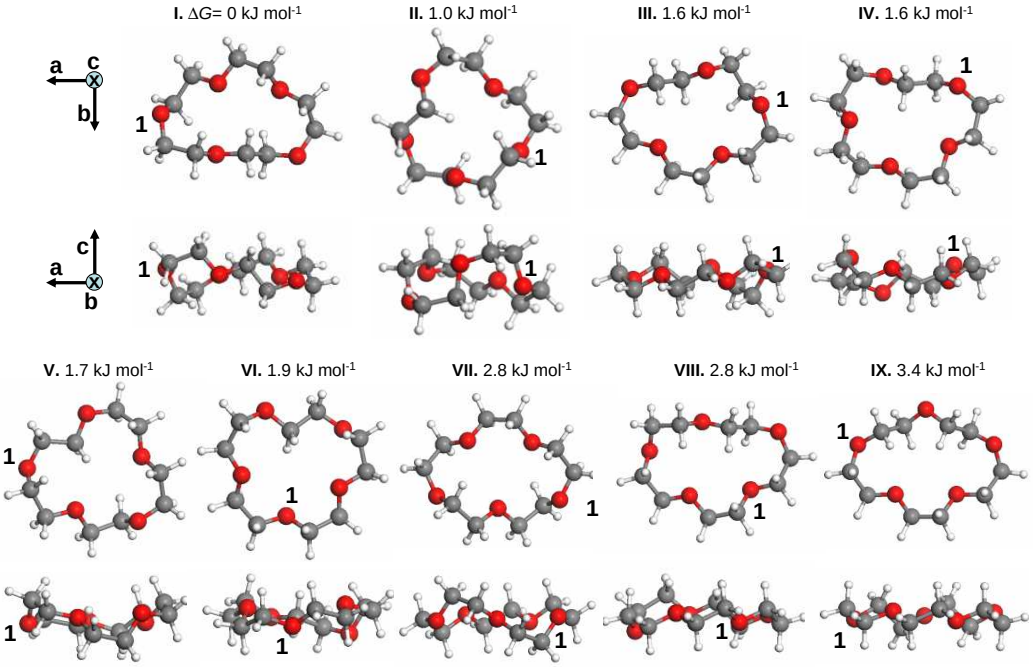

Figure 6.2: Lowest free energy conformers of the isolated 15–crown–5 molecule predicted by the MP2/6-311++G(d,p) computation. The molecular structures are depicted in the *ab* and *ac* planes (see the principal axis vectors shown in the upper part). The conformers are ranked I through IX according to the indicated values of their relative Gibbs free energies. The oxygen atom labelled as 1 in each conformer is taken as reference for the list of structural parameters provided in Table 6.3.

Table 6.1: Computational *ab initio* MP2/6-311++G(d,p) structural parameters for the low energy conformers of 15c5: effective rotational constants A, B, C (in MHz), asymmetry parameter κ and components of the dipole moment $|\mu_i|$ (in D). The relative MP2 electronic and Gibbs free energies of the conformers are indicated (in kJ mol^{-1}) together with the free energy values obtained from the DFT computations at the B3LYP/6-311++G(d,p), B3LYP/aug-cc-pVTZ, M06/6-311++G(d,p) and M06/aug-cc-pVTZ levels of theory (denoted B3LYPa, B3LYPb, M06a and M06b, respectively). Further structural parameters of the conformers (interatomic distances and bond angles) are provided in Table 6.3.

	I	II	III	IV	V	VI	VII	VIII	IX
A	829	603	725	693	618	607	728	792	758
B	417	566	433	452	500	495	445	412	414
C	308	348	289	294	298	288	303	289	281
κ	-0.58	0.71	-0.34	-0.21	0.26	0.30	-0.33	-0.51	-0.44
$\lvert\mu_a\rvert$	0.91	3.6	0.0	0.7	2.4	0.6	0	0.5	0
$\lvert\mu_b\rvert$	2.3	0.5	4.2	3.4	0.9	2.9	2.1	3.6	5.6
$\lvert\mu_c\rvert$	0.6	0.8	1.6	1.3	0.3	1.2	0	2.1	0
ΔE_{MP2}	0	2.3	2.9	4.2	4.5	6.3	6.2	4.1	7.4
ΔG_{MP2}	0	1.0	1.6	1.6	1.7	1.9	2.8	2.8	3.4
ΔG_{B3LYPa}	0	3.5	–1.3	–1.2	–0.1	–0.4	–0.1	0.8	3.0
ΔG_{B3LYPb}	0	2.6	–3.0						
ΔG_{M06a}	0	–1.4	–0.7	0.7	–0.5	1.0	4.3	0.7	2.5
ΔG_{M06b}	0	0.1	–2.4						

the mutual repulsion exerted by the lone-pair orbitals of the oxygen atoms. Consequently, the most stable arrangements are achieved by orienting some of the oxygen atoms toward the outer part of the backbone so that the negative charge density inside the ring is reduced. In this way, weak C-H$\cdots$O hydrogen bonds are also allowed to form across the ring [**?**]. Noticeably, this type of conformation is markedly different from the typical structure of the crown ether in its complexes with cationic species. Upon complexation, a negatively charged cavity must be recovered by a suitable reorientation of the oxygen atoms toward the inside of the ring [3]. The characterization of the isolated crown ether performed in this work should contribute to determine the magnitude of such a "conformational switch" required for the formation of the complex [19].

The atomic distances and bond angles listed in Table 6.3 provide illustrate some of the key features of the low energy conformers of 15-crown–5. First of all, most of the conformers place one of the oxygens at a particularly large distance from its nearest neighbours (≈3.6 Å). That oxygen is part of a cuasiplanar O–C–C–O backbone segment with associated dihedral angle close to 180^o. The remaining O–O distances are of the order 2.8–3.0 Å, still about 10 percent higher in average than *e.g.* in the 15c5–K$^+$ complex [4]. The free 15c5 ether also displays a greater dispersion in the C–O–C bond angles and in the backbone dihedral angles in comparison to its complexes with the alkali cations.

Among the low energy conformers I–IX, structures of both prolate and oblate character are found. The prolate conformations (I, III, IV, VII, VIII, IX) display a backbone that is asymmetrically stretched along the a and b axes. This leads to a marked difference between the rotational constants A and B and to a correspondingly positive value of κ. In contrast, the oblate structures (II, V and VI) are characterized by a roughly round projection of the ether backbone in the *ab* plane. Conformer II features the largest value of the rotational constant B, leading to the most marked oblate character (the largest positive value of κ). It is interesting to notice that conformer II is also unique in the sense that it displays the most significant degree of folding among the conformers scoped in this study. This results in the largest values for the C constant and for the planar moment of inertia P_{cc}. Such folded structures, so characteristic of the crown–metal complexes, are however apparently scarce for the free ether. In Conformer II, the greater proximity between the oxygen atoms is compensated by their alternate orientation and by the formation of tighter CH$\cdots$O cross ring attractive interactions made possible by the folding [**?**].

One intriguing aspect of the present study is the absence of conformer VII in the experimental microwave spectrum. In our survey, some tens of lines remained unassigned but none of them could be adscribed to a trace of that conformer. Those lines plausibly belong to conformers lying higher in energy than the ones considered here, although no progression within them could be associated to a single rotamer. Conformer VII was expected to be detected since its MP2 Gibbs free energy is roughly the same as that of conformer VIII (2.8 kJ mol^{-1}). The relative electronic energy is much larger (6.2 kJ mol^{-1}), but again this is also the case for conformers VI and IX. One should consider the possibility that conformer VII could lie significantly higher

Table 6.2: Experimental effective rotational constants (A, B, C, in MHz) and Quartic centrifugal distortion coefficients (in kHz) for the eight rotamers identified in the microwave spectrum. The spectral analysis was performed in the A–reduced I^r representation for all conformers, except for the oblate conformer II for which the III^l reprentation was employed. The number of experimental lines and the standard deviation of the fit, σ_{FIT} (in kHz), are indicated in the bottom entries. Further structural parmeters listed are the asymmetry parameter, κ, and the planar moments of inertia, P_{aa}, P_{bb} and P_{cc} (in amuÅ^2).

	I	II	III	IV
A	806.82516(19)[1]	595.89572(45)	710.44967(14)	675.53597(102)
B	417.16283(22)	560.83329(32)	434.54680(15)	452.96086(57)
C	303.779894(42)	342.00682(13)	287.053113(37)	289.871689(147)
κ	-0.549214(1)	0.723797(6)	-0.303284(1)	-0.154243(6)
P_{aa}/uÅ^2	1124.36137(51)	765.35444(86)	1106.11416(38)	1055.5323(17)
P_{bb}	539.27417(51)	712.33255(86)	654.46255(38)	687.9250(17)
P_{cc}	87.10570(51)	135.76723(86)	56.88837(38)	60.1907(17)
Δ_J	0.0103(10)	0.0820(37)	0.01017(571)	-0.0321(41)
Δ_{JK}	0.0608(48)	-0.1345(90)	0.0435(25)	0.2122(25)
Δ_K	0.1212(43)	0.0663(51)	0.0731(318)	[0.0]
δ_J	0.00147(47)	[0.0][2]	0.00352(28)	-0.01887(205)
δ_K	0.0534(58)	[0.0]	0.0426(21)	[0.0]
number of lines	55	46	61	49
σ_{FIT}	1.3	1.7	1.3	4.9
	V	VI	VIII	IX
A	616.32858(37)	600.21(35)	774.8203(10)	753.07198(82)
B	493.0480(80)	493.54(24)	413.55036(189)	412.42586(17)
C	295.03735(43)	285.71987(7)	279.824057(91)	279.824057(61)
κ	0.23259(5)	0.322(3)	-0.459688(9)	-0.439609(2)
P_{aa}	958.9795(98)	975.39(49)	1187.9281(35)	1180.17578(81)
P_{bb}	753.9528(98)	793.40(49)	618.1318(35)	625.88419(81)
P_{cc}	66.0303(98)	48.60(49)	34.1214(35)	45.20575(81)
Δ_J	-0.260(21)	0.000405(11)	[0.0]	0.002120(14)
Δ_{JK}	[0.0]	[0.0]	[0.0]	[0.0]
Δ_K	0.270(21)	[0.0]	2.153(171)	[0.0]
δ_J	0.948(81)	[0.0]	[0.0]	[0.0]
δ_K	[0.0]	[0.0]	[0.0]	[0.0]
number of lines	35	21	16	26
σ_{FIT}	5.7	0.8	3.7	1.6

Table 6.3: Selected geometrical parameters for the three 15c5 conformers studied in this work at the MP2/6-311++G(d,p) level of theory (distances in Å, angles in degrees). The distances between adjacent oxygens (first data column) constitute a measure of the peripheral dimension of the crown cavity. The bond and dihedral angles describe the conformation and distortion of the ether backbone along the ring. The first oxygen atom ($j = 1$) is the one labelled in Fig. 6.2 and the sequence proceeds anticlockwise.

conformer	O_j–O_{j+1} $j = 1 - 5$ **distances**	**C–O_j–C** $j = 1 - 5$ **bond angles**	**O_j–C–C–O_{j+1}** $j = 1 - 5$ **dihedral angles**	**Full sequence of dihedral angles**[a]
I[b]	2.89, 2.77, 3.02, 3.63, 3.05	115.1, 111.9, 113.1, 115.7, 111.2	70.5, 64.1, -76.9, -175.6, -78.6	+00 +0+ −00 0−+ −00
II[b]	3.05, 3.05, 2.95, 3.08, 2.89	113.3, 114.1, 114.8, 113.4, 111.5	-77.2, 76.9, 71.9, -80.1, 65.4	−+0 +−+ +0+ −00 +−0
III[b]	2.94, 2.94, 2.99, 3.61, 2.96	113.4, 110.9, 111.7, 115.5, 112.5	68.1, –75.9, 72.6, 172.1, –71.0	+00 −00 +−+ 00− −0−
IV	2.89, 2.90,2.86, 2.98,3.60	112.2, 112.1, 113.1, 114.4, 114.8	65.7, –75.0, 63.4, 73.8,173.05	+00 −00 ++0 +−0 00−
V	3.64 , 3.14, 2.94, 2.86 ,2.89	115.0,113.5, 111.1, 113.4, 113.4	176.4, 85.2, –68.6, 72.2, 70.6	00− +00 −+0 +00 +−+
VI	2.82, 3.07,3.62, 2.90, 2.83	112.8, 113.3,114.7 114.6, 112.7	–69.5,82.3,170.2, –74.5,67.9	−00 +−0 −00 −00 +00
VII	2.90, 2.90, 2.95, 3.00, 2.95	115.7, 112.8, 114.2, 112.8, 114.2	76.5, 76.5 , –69.9, 82.6, -69.8	+00 +0+ −00 +00 −+0
VIII	2.93,2.96 , 2.90, 3.62 ,3.03	110.7,114.2 , 111.7, 114.9 ,111.7	–74.9,75.6 ,67.3 179.2, 75.0	−00 +0+ +00 0+− +00
IX	3.65, 3.65, 2.98 2.95,2.98	113.2 ,115.7,110.7 110.7, 115.4	171.4 171.3, 71.7, 71.6, -74.5	000 00− +00 −00 +−+

[a] full sequence of dihedral angles α around consecutive C–C, C–O and C–O bonds; notation: + for $0 \leq \alpha < 2\pi/3$; 0 for $2\pi/3 \leq \alpha < 4\pi/3$ and − for $4\pi/3 \leq \alpha < 2\pi$.

[b] reproduced from [19]

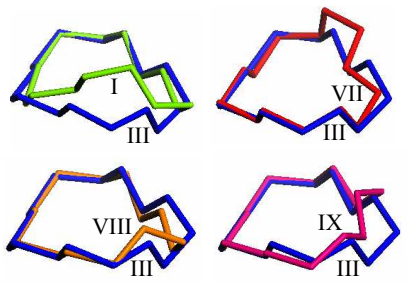

Figure 6.3: Comparison of backbones of pairs of 15–crown–5 conformers related to each other by a small number of dihedral backbone torsions. The hydrogen atoms are not shown for clarity. Conformer III (blue) is taken as reference in the comparisons.

in energy than predicted by the MP2/6-311++G(d,p) computation, and would therefore not be significantly populated in our experiment. Table 6.1 shows that the relative energy of conformers I–IX is quite sensitive to the computational approach employed. Changes in the range of $\pm 3\,\mathrm{kJ\,mol^{-1}}$ are typically found when comparing the MP2 energies with those from the density functional methods or when changing the basis set. It can be appreciated that none of the B3LYP and M06 methods (whether with the 6-311++G(d,p) or the aug–cc–pVTZ basis sets) converges to the qualitative energetic ordering predicted by the MP2 computation.

At this point, the question arises of whether conformer VII may be kinetically connected to lower energy structures through particularly small conformational barriers. In that case, it could undergo conformational relaxation through collisions during the supersonic expansion stage employed in our experiments. Otherwise, the thermal population of conformers prior to the supersonic expansion (correlating to the Gibbs free energies) would largely be retained. The 15c5 ether ring is quite floppy and, in fact, several of the conformers considered here are interconnected with each other by a limited number of dihedral turns in the backbone. This aspect may be not be entirely appreciated from a visual inspection of Fig. 6.2, and is therefore illustrated explicitly in Fig. 6.3 by means of several pairs of overlaid backbones. The low energy structure closest to conformer VII is that of conformer III and it is shown that both conformers are connected by essentially a single dihedral torsion is required. Hence, a leak of population from conformer VII to conformer III during the collisional cooling of the molecules would in principle be plausible. Fig. 6.3 also shows that conformers VIII and IX are also similarly close to conformer III and therefore would also relax and lose population during the supersonic expansion. It can also be appreciated that conformer III would be more kinetically stable as its conformation differs by more than one dihedral turn from that of conformer I.

A distinct property of conformer VII is that its dipole moment takes the smallest value among the nine conformers considered here. Its relatively high energy and its potential collisional relaxation to lower lying conformers may be responsible for a population too low to be detected in our experiments. While conformers VIII and IX may display a similarly low population, their dipole moments are much higher which results in a significant enhancement of the detection sensitivity for both of these conformers. It can also be appreciated that conformer III would be more kinetically stable as its conformation differs by more than one dihedral turn from that of conformer I.

6.4 Conclusions

Microwave spectroscopy in the Gigahertz region, coupled to supersonic jet molecular cooling, has demonstrated a great potential for the experimental description of the conformational landscape of small macrocycles. The exploration of an ether ring as flexible as 15c5 is challenging due to the plethora of low energy backbone structures that may be present in experiment. Within the present study, eight individual rotamers of the 15c5 molecule have been characterized through their rotational constants and quartic centrifugal coefficients. All rotamers are successfully identified among the low energy conformers predicted by quantum computations at the DFT and MP2 levels. The investigation shows that the 15c5 ring can display a range of qualitatively different prolate and oblate structures, some of which are connected with each other by a single dihedral torsion of the backbone. Each stable structure provides an appropriate balance between the intramolecular O$\cdots$O repulsions, the CH$\cdots$O attractions and the conformational stress allowed by the flexibility of the polyether ring backbone. As a consequence, most of the conformers have a stretched ring architecture in which some of the oxygen atoms are oriented towards the outside of the ring. Interestingly, one usual feature is a roughly planar O–C–C–O dihedral segment that pushes one of the oxygen atoms to a particularly large distance away from the rest of oxygen atoms. Nevertheless, the experiments also confirm the existence of a uniquely folded structure (conformer II), of marked oblate character, that had been predicted in an earlier computational study [25]. In this case, the enhanced O$\cdots$O repulsions induced by the folding of the ring are compensated by tighter CH$\cdots$O cross-ring attractions. It must be remarked that the conformations observed in this study for the free 15c5 molecule present qualitative differences with those described in previous studies for this crown ether in its complexes with cationic guests. Cation inclusion demands that a high electron density builds up in the inner region of the ether ring. Hence, the formation of the complex requires concerted dihedral torsions of the ether backbone

that bring the lone-pair orbitals of the oxygen atoms to the coordination shell of the cation. The present study should serve to describe the magnitude of these changes, which define the "conformational switch" that the ether backbone must undergo in a supramolecular complexation process.

SUPPLEMENTARY MATERIAL

Table S1: List of experimental lines measured for the 15c5 rotamer assigned to the MP2 conformer I. The table indicates the assigned rotational transition, the experimental line, ν_{exp}, and the difference with respect to the best–fit of the line, ν_{fit}, provided by the rotational constants given in Table 6.2.

J'	K'_{-1}	K'_{+1}	J''	K''_{-1}	K''_{+1}	ν_{exp} (MHz)	$\nu_{fit} - \nu_{exp}$ (MHz)
4	4	1	3	3	0	6010.1052	-0.0001
4	4	0	3	3	1	6012.9261	-0.0001
5	5	1	4	4	0	7625.1454	0.0014
5	5	0	4	4	1	7625.4237	0.0019
5	4	1	4	3	2	6747.0762	-0.0006
6	5	2	5	4	1	8350.9341	-0.0004
6	5	1	5	4	2	8353.4449	-0.0015
6	6	0	5	5	0	9238.9225	-0.0015
6	6	1	5	5	1	9238.9461	0.0012
6	4	3	5	3	2	7417.7035	-0.0016
7	1	7	6	0	6	4513.6140	-0.0017
7	0	7	6	1	6	4473.0895	-0.0004
7	0	7	6	0	6	4500.9325	0.0007
7	1	7	6	1	6	4485.7739	0.0001
7	2	6	6	1	5	5301.5903	0.0019
8	0	8	7	0	7	5104.0055	-0.0005
8	1	8	7	1	7	5096.8983	0.0001
8	0	8	7	1	7	5091.3219	-0.0002
8	1	8	7	0	7	5109.5817	-0.0005
8	2	7	7	2	6	5532.3342	0.0009
8	2	6	7	2	5	6125.1673	0.0008
8	2	7	7	1	6	5782.4952	-0.0021
8	1	7	7	1	6	5643.7574	0.0001
8	3	6	7	3	5	5812.5452	0.0003
8	3	5	7	3	4	6168.0091	-0.0020
8	1	7	7	2	6	5393.5958	0.0025
9	0	9	8	0	8	5709.2847	0.0003
9	1	9	8	1	8	5706.0953	-0.0004
9	0	9	8	1	8	5703.7083	0.0001
9	1	9	8	0	8	5711.6717	-0.0002
9	1	8	8	1	7	6229.1923	0.0012
9	2	8	8	1	7	6300.8751	-0.0009
9	2	8	8	2	7	6162.1376	0.0015
9	2	7	8	2	6	6792.1825	-0.0002
9	3	7	8	3	6	6500.9554	-0.0015
9	3	6	8	3	5	6983.6178	0.0051
10	0	10	9	1	9	6313.3414	0.0008
10	1	10	9	1	9	6314.3423	0.0001
10	0	10	9	0	9	6315.7261	-0.0020
10	1	10	9	0	9	6316.7296	-0.0001
10	2	8	9	3	7	6760.6166	-0.0039
10	1	9	9	2	8	6747.4564	0.0012
10	1	9	9	1	8	6819.1394	-0.0007
11	0	11	10	1	10	6921.7387	0.0003
11	1	11	10	1	10	6922.1514	-0.0004
11	0	11	10	0	10	6922.7404	0.0004
11	1	11	10	0	10	6923.1535	0.0001
12	0	12	11	1	11	7529.6052	-0.0002
12	1	12	11	0	11	7530.1879	0.0008
13	0	13	12	1	12	8137.2529	0.0001
13	1	13	12	0	12	8137.4891	0.0001
14	0	14	13	1	13	8744.8135	-0.0001
14	1	14	13	0	13	8744.9082	-0.0002
16	0	16	15	1	15	9959.8602	0.0008
16	1	16	15	0	15	9959.8736	-0.0007

Table S2: Same as Table S1 for the 15c5 rotamer assigned to the MP2 conformer 2.

J'	K'_{-1}	K'_{+1}	J''	K''_{-1}	K''_{+1}	ν_{exp} (MHz)	$\nu_{fit} - \nu_{exp}$ (MHz)
6	3	4	5	3	3	5281.2264	0.0018
6	2	4	5	2	3	5287.9597	-0.0006
6	4	2	5	4	1	6268.1025	0.0003
7	0	7	6	0	6	5023.7934	0.0002
7	1	7	6	1	6	5023.7934	0.0002
7	1	6	6	1	5	5495.3424	0.0029
7	2	6	6	2	5	5495.3298	-0.0013
7	3	5	6	3	4	5967.2515	- 0.0018
7	2	5	6	2	4	5967.8945	-0.0015
7	4	4	6	4	3	6433.9002	-0.0009
7	3	4	6	3	3	6453.1305	0.0007
7	5	3	6	5	2	6833.6985	-0.0001
8	0	8	7	0	7	5707.7940	-0.0002
8	1	8	7	1	7	5707.7940	-0.0002
8	1	7	7	1	6	6179.2885	-0.0004
8	2	7	7	2	6	6179.2885	0.0001
8	3	5	7	3	4	7125.8347	0.0003
8	3	6	7	3	5	6651.1501	0.0001
8	2	6	7	2	5	6651.2017	0.0019
8	4	4	7	4	3	7627.8764	-0.0001
8	4	5	7	4	4	7123.5435	-0.0006
9	1	9	8	1	8	6391.7930	-0.0007
9	0	9	8	0	8	6391.7930	-0.0007
9	1	8	8	1	7	6863.2613	0.0007
9	2	8	8	2	7	6863.2613	0.0007
9	2	7	8	2	6	7334.9777	0.0008
9	3	7	8	3	6	7334.9777	-0.0044
9	3	6	8	3	5	7807.6744	0.0007
10	0	10	9	0	9	7075.7899	-0.0009
10	1	10	9	1	9	7075.7899	-0.0009
10	1	9	9	1	8	7547.2418	0.0018
10	2	9	9	2	8	7547.2418	0.0018
10	2	8	9	2	7	8018.8577	-0.0007
10	3	8	9	3	7	8018.8577	-0.0005
10	4	7	9	4	6	8491.0088	-0.0003
10	3	7	9	3	6	8491.0278	0.0020
11	0	11	10	0	10	7759.7856	0.0007
11	1	11	10	1	10	7759.7856	0.0007
11	1	10	10	1	9	8231.2229	0.0011
11	2	10	10	2	9	8231.2229	0.0011
11	2	9	10	2	8	8702.7789	-0.0010
11	3	9	10	3	8	8702.7789	-0.0010
11	4	8	10	4	7	9174.7003	0.0003
11	3	8	10	3	7	9174.7003	-0.0009
12	0	12	11	0	11	8443.7750	-0.0006
12	1	12	11	1	11	8443.7750	-0.0006

Table S3: Same as Table S1 for the 15c5 rotamer assigned to the MP2 conformer 3.

J'	K'_{-1}	K'_{+1}	J''	K''_{-1}	K''_{+1}	ν_{exp} (MHz)	$\nu_{fit} - \nu_{exp}$ (MHz)
4	4	0	3	3	1	5346.4460	-0.0004
4	4	1	3	3	0	5335.7571	-0.0009
4	4	0	3	3	0	5337.2848	-0.0004
4	4	1	3	3	1	5344.9181	-0.0010
5	5	0	4	4	0	6761.6678	0.0010
5	5	1	4	4	1	6762.9635	-0.0010
5	5	1	4	4	0	6761.4379	0.0007
5	5	0	4	4	1	6763.1947	0.0007
6	1	5	5	2	4	4021.9427	0.0011
6	5	2	5	4	1	7488.9079	0.0006
6	5	1	5	4	2	7504.5680	0.0008
6	6	1	5	5	0	8183.1829	-0.0016
6	6	0	5	5	1	8183.4468	0.0004
6	3	4	5	2	4	6470.6382	0.0022
7	6	2	6	5	1	8917.5112	-0.0001
7	6	1	6	5	2	8920.3704	0.0002
7	3	5	6	2	5	7427.6298	-0.0022
7	4	3	6	3	3	7367.2253	0.0020
8	1	7	7	2	6	5315.7932	0.0001
8	2	7	7	1	6	5383.7239	-0.0004
9	0	9	8	1	8	5416.9082	-0.0011
9	1	9	8	0	8	5417.5164	0.0012
9	1	8	8	2	7	5908.7258	-0.0006
9	2	8	8	1	7	5934.5497	-0.0006
9	4	5	8	3	5	8831.5494	-0.0020
9	3	6	8	2	6	8946.2481	0.0001
10	0	10	9	1	9	5991.1354	-0.0006
10	1	10	9	0	9	5991.3211	-0.0012
10	1	9	9	2	8	6489.6933	0.0008
10	2	9	9	1	8	6498.9853	-0.0014
10	3	8	9	2	7	7097.9467	0.0014
11	0	11	10	1	10	6565.2453	0.0012
11	1	11	10	0	10	6565.3002	-0.0001
11	1	10	10	2	9	7065.9506	0.0010
11	2	10	10	1	9	7069.1610	-0.0006
11	3	9	10	2	8	7616.1342	0.0029
11	3	8	10	4	7	7763.5649	0.0013
12	0	12	11	1	11	7139.3188	-0.0040
12	1	12	11	0	11	7139.3416	0.0021
12	1	11	11	2	10	7640.5280	0.0005
12	2	11	11	1	10	7641.6029	-0.0003
13	0	13	12	1	12	7713.4011	0.0010
13	1	13	12	0	12	7713.4011	0.0010
13	1	12	12	2	11	8214.5747	0.0004
13	2	12	12	1	11	8214.9228	-0.0028
14	0	14	13	1	13	8287.4770	0.0015
14	1	14	13	0	13	8287.4770	0.0015
14	1	13	13	2	12	8788.4872	-0.0017
14	2	13	13	1	12	8788.6008	-0.0005
14	2	12	13	3	11	9292.2054	-0.0019
14	3	12	13	2	11	9295.9363	-0.0005
15	0	15	14	1	14	8861.5553	0.0002
15	1	15	14	0	14	8861.5553	0.0002
15	1	14	14	2	13	9362.3965	0.0006
15	2	14	14	1	13	9362.4325	0.0013
15	2	13	14	3	12	9866.1911	-0.0011
15	3	13	14	2	12	9867.4947	0.0017
16	0	16	15	1	15	9435.6370	-0.0003
16	1	16	15	0	15	9435.6370	-0.0003

Table S4: Same as Table S1 for the 15c5 rotamer assigned to the MP2 conformer IV.

J'	K'_{-1}	K'_{+1}	J''	K''_{-1}	K''_{+1}	ν_{exp} (MHz)	$\nu_{fit} - \nu_{exp}$ (MHz)
4	4	0	3	3	1	5120.1989	-0.0026
5	5	1	4	4	0	6459.7137	-0.0039
5	5	0	4	4	1	6463.8746	-0.0035
5	3	2	4	2	3	5846.3385	-0.0076
5	4	2	4	3	1	5803.0265	-0.0052
5	4	1	4	3	2	5935.3048	0.0158
6	5	1	5	4	2	7240.8168	0.0055
6	5	2	5	4	2	7233.7848	0.0009
7	4	3	6	3	3	7233.4849	-0.0004
8	0	8	7	1	7	4888.8009	-0.0037
8	1	8	7	0	7	4889.283	-0.0008
8	2	7	7	1	6	5405.5537	0.0027
9	0	9	8	0	8	5468.7377	-0.0007
9	1	9	8	0	8	5468.7609	-0.0025
9	1	9	8	1	8	5468.6686	0.0040
9	0	9	8	1	8	5468.6362	-0.0033
9	1	8	8	1	7	5974.9019	0.0028
9	2	8	8	2	7	5971.2628	0.0053
9	2	7	8	2	6	6520.8234	-0.0042
9	2	7	8	3	6	6424.377	0.0053
10	0	10	9	0	9	6048.3831	-0.0120
10	1	10	9	1	9	6048.3831	0.0068
10	0	10	9	1	9	6048.3831	0.0131
10	1	10	9	0	9	6048.3831	-0.0183
10	1	9	9	2	8	6551.0146	0.0050
10	2	9	9	1	8	6552.993	0.0035
10	3	8	9	2	7	7088.4745	-0.0078
10	2	8	9	3	7	7040.3941	-0.0001
10	3	8	9	2	7	7088.4817	-0.0006
11	0	11	10	1	10	6628.0824	0.0013
11	1	11	10	0	10	6628.0824	-0.0065
11	1	10	10	2	9	7130.9368	0.0020
11	2	10	10	1	9	7131.4969	0.0013
12	1	12	11	0	11	7207.7892	-0.0049
12	0	12	11	1	11	7207.7892	-0.0030
12	1	11	11	2	10	7710.5171	-0.0025
12	2	11	11	1	10	7710.6737	0.0001
13	1	12	12	2	11	8290.0702	0.0126
13	2	12	12	1	11	8290.0864	-0.0125
13	2	11	12	3	10	8795.2702	0.0001
13	3	11	12	2	10	8796.8322	-0.0001
13	0	13	12	0	12	7787.5087	0.0021
13	1	13	12	1	12	7787.5087	0.0024
14	0	14	13	1	13	8367.2237	0.0011
14	1	14	13	0	13	8367.2238	0.0011
14	2	12	13	3	11	9374.4827	-0.0007
14	3	12	13	2	11	9374.9415	-0.0008
14	0	14	13	1	13	8367.2232	0.0006
14	1	14	13	0	13	8367.2232	0.0005

Table S5: Same as Table S1 for the 15c5 rotamer assigned to the MP2 conformer V.

J'	K'_{-1}	K'_{+1}	J''	K''_{-1}	K''_{+1}	ν_{exp} (MHz)	$\nu_{fit} - \nu_{exp}$ (MHz)
8	0	8	7	1	7	4972.9013	0.0002
8	1	8	7	0	7	4972.9013	-0.0085
8	3	5	7	3	4	6591.4177	0.0001
9	1	9	8	1	8	5562.9493	-0.0022
9	0	9	8	0	8	5562.9493	-0.0031
9	2	8	8	2	7	6068.1234	0.0056
9	1	8	8	1	7	6068.1924	-0.0177
10	1	10	9	1	9	6153.0145	0.0099
10	0	10	9	0	9	6153.0145	0.0098
10	2	9	9	2	8	6658.0169	0.0038
10	1	9	9	1	8	6658.0329	0.0041
11	1	11	10	1	10	6743.0569	-0.0032
11	0	11	10	0	10	6743.0569	-0.0032
12	0	12	11	0	11	7333.1138	-0.0026
12	1	12	11	1	11	7333.1138	-0.0026
12	2	11	11	2	10	7837.9294	0.00778
12	1	11	11	1	10	7837.9294	0.00737
13	0	13	12	0	12	7923.1694	-0.0030
13	1	13	12	1	12	7923.1694	-0.0030
13	1	12	12	1	11	8427.9236	0.0044
13	2	12	12	2	11	8427.9236	0.0045
12	3	10	11	3	9	8343.8344	0.0030
12	2	10	11	2	9	8343.8521	-0.0038
14	0	14	13	0	13	8513.2251	-0.0020
14	1	14	13	1	13	8513.2251	-0.0020
14	1	13	13	1	12	9017.935	0.0022
14	2	13	13	2	12	9017.935	0.0022
15	0	15	14	0	14	9103.2816	0.0017
15	1	15	14	1	14	9103.2816	0.0017
15	1	14	14	1	13	9607.9535	-0.0035
15	2	14	14	2	13	9607.9535	-0.0035
16	0	16	15	0	15	9693.3334	0.0030
16	1	16	15	1	15	9693.3334	0.0030
16	1	15	15	1	14	10197.9834	-0.0043
16	2	15	15	2	14	10197.9834	-0.0043

Table SVI: Same as Table S1 for the 15c5 rotamer assigned to the MP2 conformer VI.

J'	K'_{-1}	K'_{+1}	J''	K''_{-1}	K''_{+1}	ν_{exp} (MHz)	$\nu_{fit} - \nu_{exp}$ (MHz)
8	0	8	7	1	7	4827.2339	0.0028
8	1	8	7	0	7	4827.2339	-0.0001
9	0	9	8	1	8	5398.6527	0.0010
9	1	9	8	0	8	5398.6527	0.00065
10	0	10	9	1	9	5970.0766	0.00065
10	1	10	9	0	9	5970.0766	0.0006
11	0	11	10	1	10	6541.5014	-0.001
11	1	11	10	0	10	6541.5014	-0.001
11	1	10	10	2	9	7053.1369	0.0001
11	2	10	10	1	9	7053.1369	-0.0007
12	0	12	11	1	11	7112.9292	-0.0009
12	1	12	11	0	11	7112.9292	-0.0009
13	0	13	12	1	12	7684.3569	-0.0011
13	1	13	12	0	12	7684.3569	-0.0011
13	1	12	12	2	11	8195.8793	0.0001
14	0	14	13	0	13	8255.7854	-0.0002
14	1	14	13	1	13	8255.7854	-0.0002
15	0	15	14	0	14	8827.2131	0.0006
15	1	15	14	1	14	8827.2131	0.0006
16	0	16	15	0	15	9398.6391	0.0006
16	1	16	15	1	15	9398.6391	0.0006

Table S7: Same as Table S1 for the 15c5 rotamer assigned to the MP2 conformer VII.

J'	K'_{-1}	K'_{+1}	J''	K''_{-1}	K''_{+1}	ν_{exp} (MHz)	$\nu_{fit} - \nu_{exp}$ (MHz)
6	6	0	5	5	0	8876.4626	-0.0043
6	6	1	5	5	1	8876.5151	0.0044
9	0	9	8	1	8	5413.5383	0.0062
9	1	9	8	0	8	5417.502	0.0014
10	0	10	9	1	9	5988.6335	0.0055
10	1	10	9	0	9	5990.1733	0.0045
11	0	11	10	1	10	6563.0417	0.0018
11	1	11	10	0	10	6563.6285	0.0016
11	1	10	10	2	9	7052.6752	-0.0009
11	2	10	10	1	9	7077.2823	-0.0027
12	0	12	11	1	11	7137.1919	0.0016
12	1	12	11	0	11	7137.4128	0.0022
13	1	13	12	0	12	7711.3279	-0.0011
13	0	13	12	1	12	7711.2446	-0.0028
14	1	14	13	0	13	8285.2987	-0.0061
14	0	14	13	1	13	8285.2696	-0.0053

Table S8: Same as Table S1 for the 15c5 rotamer assigned to the MP2 conformer VIII.

J'	K'_{-1}	K'_{+1}	J''	K''_{-1}	K''_{+1}	ν_{exp} (MHz)	$\nu_{fit} - \nu_{exp}$ (MHz)
7	0	7	6	1	6	4160.421	0.0016
7	1	7	6	0	6	4177.9751	0.0025
8	0	8	7	1	7	4725.0798	-0.0020
8	1	8	7	0	7	4731.9004	0.00032
9	0	9	8	1	8	5286.6342	-0.0026
9	1	9	8	0	8	5289.2043	0.0018
10	0	10	9	1	9	5846.9525	-0.0020
10	1	10	9	0	9	5847.8965	-0.0005
10	1	9	9	2	8	6335.4152	-0.0008
10	2	9	9	1	8	6372.5247	0.0035
11	0	11	10	1	10	6406.8078	0.0013
11	1	11	10	0	10	6407.1473	0.0010
11	3	8	10	4	7	7075.7899	0.0002
12	0	12	11	1	11	6966.4922	-0.0014
12	1	12	11	0	11	6966.6148	0.0005
12	1	11	11	2	10	7467.6384	-0.0011
12	2	11	11	1	10	7473.8215	-0.0008
13	0	13	12	1	12	7526.1279	0.0005
13	1	13	12	0	12	7526.1701	0.0004
13	1	12	12	2	11	8028.4676	-0.0017
14	0	14	13	1	13	8085.7459	-0.0012
14	1	14	13	0	13	8085.7603	-0.0015
15	0	15	14	1	14	8645.3646	-0.0009
15	1	15	14	0	14	8645.3734	0.0029
16	0	16	15	1	15	9204.9878	0.0018
16	1	16	15	0	15	9204.9878	0.0001

Bibliography

[1] F. Davis, S. Higson, *Macrocycles: Construction, Chemistry and Nanotechnology Applications*, John Wiley & Sons 2011, ISBN 978-0-470-71462-1

[2] G. W. Gokel, *Crown ethers and cryptands*, Royal Society of Chemistry (1994), ISBN-13: 978-0851867045

[3] B. Martínez–Haya, P. Hurtado, A. R. Hortal, S. Hamad, J. D. Steill, J. Oomens. J. Phys. Chem. A. 114 (2010) 7048.

[4] P. Hurtado, A. R. Hortal, F. Gámez, S. Hamad, B. Martínez–Haya. Phys. Chem. Chem. Phys. 12 (2010) 13752.

[5] P. Hurtado, F. Gámez, S. Hamad, B. Martínez–Haya, J. D. Steill, J. Oomens. J. Phys. Chem. A. 115 (2011) 7275.

[6] F. Gámez, P. Hurtado, B. Martínez–Haya, G. Berden, J. Oomens. Int. J. Mass Spectrom. 308 (2011) 217.

[7] F. Gámez, P. Hurtado, S. Hamad, B. Martínez–Haya, G. Berden, J. Oomens. ChemPlusChem. 77(2) (2012) 118.

[8] P. Hurtado, F. Gámez, S. Hamad, B. Martínez–Haya, J. D. Steill, J. Oomens. J. Chem. Phys. 136 (2012) 114301(1).

[9] J.D. Rodriguez, J.M. Lisy. Int. J. Mass Spectrom. 283 (2009) 135.

[10] J.D. Rodriguez, T.D. Vaden, J.M. Lisy. J. Am. Chem. Soc. 131 (2009) 17277.

[11] J.D. Rodriguez, D. Kim, P. Tarakeshbar, J.M. Lisy. J. Phys. Chem. A. 114 (2010) 1514.

[12] J. D. Rodriguez, J. M. Lisy. J. Am. Chem. Soc. 133 (2011) 11136.

[13] Y. Inokuchi, O. V. Boyarkin, R. Kusaka, T. Haino, T. Ebata, T. R. Rizzo. J. Am. Chem. Soc. 133 (2011) 12256.

[14] V. A. Shubert, W. H. 3^{rd} James, T. S. Zwier. J. Phys. Chem. A. 113 (2009) 8055.

[15] V. A. Shubert, C. W. Müller, T. S. Zwier. J. Phys. Chem. A. 113 (2009) 8067.

[16] R. Kusaka, Y. Inokuchi, T. Ebata T. Phys. Chem. Chem. Phys. 10 (2008) 6238.

[17] R. Kusaka, S. Kokubu, Y. Inokuchi, T. Haino, T. Ebata. Phys. Chem. Chem. Phys. 13 (2011) 6827.

[18] J. P. Schermann. *Spectroscopy and Modelling of Biomolecular Building Blocks* Elsevier, Amsterdam 2008. ISBN: 978-0-444-52708-0

[19] F. Gámez, B. Martínez–Haya, S. Blanco, J.C. López, J.L. Alonso. J. Phys. Chem. Lett. 3 (2012) 482.

[20] J. L. Alonso, C. Perez, M. E. Sanz, J. C. López, S. Blanco. Phys. Chem. Chem. Phys. 11 (2009) 617 .

[21] S. Blanco, J. C. Lopez, S. Mata, J. L. Alonso. Angew. Chem.-Int. Ed. 49 (2010) 9187.

[22] G. Scoles. Ed *Atomic, Molecular Beam Methods* **1992** Oxford University, Oxford, Vol 2.

[23] R. S. Ruoff, T. D. Klots, T. Emilsson, H. S. Gutowsky. J. Chem. Phys. 93 (1990) 3142.

[24] M.D. Paulsen, J.R. Rustad, B.P. Hay. J. Mol. Struct. (Theochem) 397 (1997) 1.

[25] S. E. Hill, D. Feller. Int. J. Mass Spectrom. 201 (2000) 41.

[26] B. Jagannadh, K.R.D. Priya, L.Ch. Devi, G.K. Sri, J. Mol. Model. 16 (2010) 285.

[27] S. Parsons. Acta Cryst. A, Section E: Structure Reports Online (2007). E63, o3130

[28] J. L. Alonso, F. J. Lorenzo, J. C. Lopez, A. Lesarri, S. Mata, H. Dreizler. Chem. Phys. 218 (1997) 267.

[29] J. K. G. Watson, in: Durig, J.R. (ed.) *Vibrational Spectra and Structure: a Series of Advances Vol. 6*, Elsevier, New York/Amsterdam (1977), 189

[30] J. K. G. Watson. J. Chem. Phys. 46 (1967) 1935.

[31] Pickett's package

[32] R. A. Motiyenko, L. Margulès, E. A. Alekseev, J. C. Guillemin, J. Demaison. J. Mol. Spectrom. 264 (2010) 94.

[33] Accelrys Materials Studio 4.4. Accelrys, Inc. San Diego CA, USA.

[34] a) A.D. Becke. J.Chem.Phys. 98 (1993) 5648.; b) P.J. Stephens, F.J. Devlin, C.F. Chabalowski, M.J. Frisch. J.Phys.Chem. 98 (1994) 11623.

[35] Y. Zhao, D. G. Truhlar. Theor. Chem. Account. 120 (2008) 215.

[36] Gaussian 09, Revision A.1, M.J. Frisch, G.W. Trucks, H.B. Schlegel, G.E. Scuseria, M.A. Robb, J.R. Cheeseman, G. Scalmani, V. Barone, B. Mennucci, G.A. Petersson, H. Nakatsuji, M. Caricato, X. Li, H. P. Hratchian, A.F. Izmaylov, J. Bloino, G. Zheng, J.L. Sonnenberg, M. Hada, M. Ehara, K. Toyota, R. Fukuda, J. Hasegawa, M. Ishida, T. Nakajima, Y. Honda, O. Kitao, H. Nakai, T. Vreven, J.A. Montgomery, Jr., J.E. Peralta,F. Ogliaro, M. Bearpark, J.J. Heyd, E. Brothers, K.N. Kudin, V.N. Staroverov, R. Kobayashi, J. Normand, K. Raghavachari, A. Rendell, J.C. Burant, S.S. Iyengar, J. Tomasi, M. Cossi, N. Rega, J.M. Millam, M. Klene, J.E. Knox, J. B. Cross, V. Bakken, C. Adamo, J. Jaramillo, R. Gomperts, R.E. Stratmann, O. Yazyev, A.J. Austin, R. Cammi, C. Pomelli, J.W. Ochterski, R.L. Martin, K. Morokuma, V.G. Zakrzewski, G.A. Voth, P. Salvador, J.J. Dannenberg, S. Dapprich, A.D. Daniels, ¨ O. Farkas, J.B. Foresman, J.V. Ortiz, J. Cioslowski, D.J. Fox, Gaussian, Inc., Wallingford CT, 2009.

Chapter 7

Proton localization and proton bridges in crown–ether rings

The $O\cdots H^{+}\cdots O$ proton bridge leads to paradigmatic examples of quantum intermolecular interactions stabilizing dimers of oxygen containing molecules, such as alcohols, ethers and related compounds. The cavities of crown ethers provide a quite interesting environment for the study of these phenomena, as they combine confinement in a well defined volume, with the tunnelling and delocalization effects typical of the proton bonded systems. We have measured the IRMPD spectra of protonated native and N-substituted crown-ethers of different size. Whereas the N-substituted ethers (1-aza- and 2-aza-18-crown-6) present well defined and relatively narrow vibrational bands, the native crown ethers (12-crown-4, 15-crown-5, 18-crown-6) display broadened spectra with ill-defined bands. Such broadening is attributed to to delocalization of the proton due to a dynamic bridge formed between two oxygen atoms of the ring. This interpretation is confirmed by *ab initio* Molecular Dynamics computations performed for these systems. When one or two of the oxygen atoms are substituted by nitrogen atoms, the proton becomes localized on one of the nitrogen sites which explains the narrow bans observed in the IRMPD spectra. In particular, no trace of sharing between the two opposed nitrogen atoms is found for the 2-aza-18-crown-6.

7.1 Introduction

The aqueous proton displays a dicoordinated structure with both solvent and/or base molecules [1]. This trend remains in the gas phase, as it has been observed in the Zundel cation $H_5O_2^+$ [2]. However, the lack of stabilization by solvent interactions lead to cyclation in terminal dibasic groups as in diammines or chalcones [3]. So, in cyclic ethers, gas phase studies allow to establish the possibility of a multiple coordination when more than two non-cyclable basic groups are presented. This is precisely the case of crown ethers, which 18-crown-6 ether as the leading basic crown–ether member [4]. The complexes formed by macrocycles with the proton, along with those with the hydronium and ammonium cations and further protonated guests, are of key relevance for the understanding of supramolecular behavior in acidic environments [5, 6]. The oxygen–shared proton bridge constitutes an examples of quantum interactions stabilizing dimers of oxygen containing molecules, such as alcohols, ethers and orelated compounds. In fact, One particularly active topic of research has been the formation of intermolecular proton bridges capable of stabilizing dimeric complexes [7, 8]. From a more fundamental viewpoint, they combined effect of proton confinentment within the intermolecular force field in the cavity volume with the quantum properties typical of the proton itself, like delocalization and tunelling.

Hence, the determination of proton affinities of ethers and polyethers has received considerable attention [4, 9, 10, 11]. Nevertheless, in spite of the rapid development of the chemistry of crown ethers, the basic conformational aspects of protonated crown complexes remain a matter of debate. In fact, gas-phase studies of protonated crown ethers are relatively scarce [12, 13]. With the aim of fill this gap, in this chapter we present preliminary results on the complexation of native crown ethers and related aza-substituted ethers with H^+. Fot this purpose, we employ a combination of infrared action spectroscopy (IRMPD) with computations. The study is aimed at the rationalization of the role played in the stabilization of these complexes by quantum delocalization effects of the proton within the interior of the ether ring. We hope to provide new insights into the structural and dynamic properties of the proton–crown complex in the absence of solvent and ion pairing effects. However, the features of experimental IRMPD spectra containing strong hydrogen bonds is of broadly and noisy appearence because of the anharmonic character of proton vibrations in the quasi–continuous potential well provided by the basis–host chemical species [14].

In this chapter we present preliminary results on complexation of crown ethers and related aza–substituted ethers with H^+. The combination of infrared spectroscopy in the gas phase with Density Functional Theory and *ab initio* molecular dynamics computation would help in the rationalization of the role played by the quantum character of proton-bridge in dicoordinated arrange of crown ethers and the localization presented in aza–crown ether as observed in experimental data.

7.2 Methods

7.2.1 Infrared Multiphoton Dissociation Spectroscopy (IRMPD).

The IRMPD spectroscopy was carried out using a Fourier transform ion cyclotron resonance beamline of the infrared free-electron laser FELIX (see previous chapters). The proton complexes are formed in 1 mM solutions of the crown ether in an acidic water/methanol mixture (1:1 v/v). The solution is electrosprayed into an hexapole trap where the ions are stored and then pulse-injected into the ICR cell. After isolation of the precursor mass, the ions are irradiated with the tunable IR light from FELIX source. Some five to ten IR laser macropulses (trains of pulses of frequency 1 GHz with a duration of about 5 μs and and energy of 35 mJ) were applied to induce the multiphoton dissociation of the complexes leading to protonated ring fragments. Monitorization of the ratio of the fragment ion signal to the total ion signal while scanning the laser wavelength constitutes the IRMPD spectra. The reported intensities have been normalized to account for the power spectrum of the FELIX laser.

7.2.2 Quantum Chemistry Calculations.

A large number of *abinitio* Molecular Dynamics simulations within the frame of atom-centered density matrix propagation ADMP [15] have been carried out. These simulations utilize the HF-CEP/4G method/basis–set, a fictitious mass tensor scaling value of 0.1 amu $Bohr^2$, which is small enough to allow the integration of the equations of motion without using a thermostat to achieve good energy conservation. The time step was set to 0.2 fs. The total number of steps of each simulation was 50000, so that the total simulation time was 10 ps. The dipole moment and atomic velocities of the system were printed at every time step.

7.3 Results

Fig. 7.1 shows the IRMPD spectra of the protonated N-substituted crown ethers 1-aza-18c6 and 2-aza-18c6. The spectra of these two complexes displays a strong

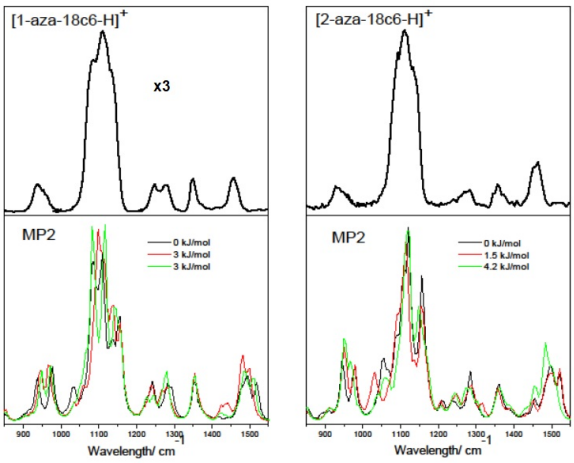

Figure 7.1: Experimental IRMPD spectra of the aza-crown ethers complexes with H^+. The harmonic appearance of the spectra is a consequence of the proton localization on a N atom of the ether ring. Computed MP2 harmonic spectra are shown for comparison.

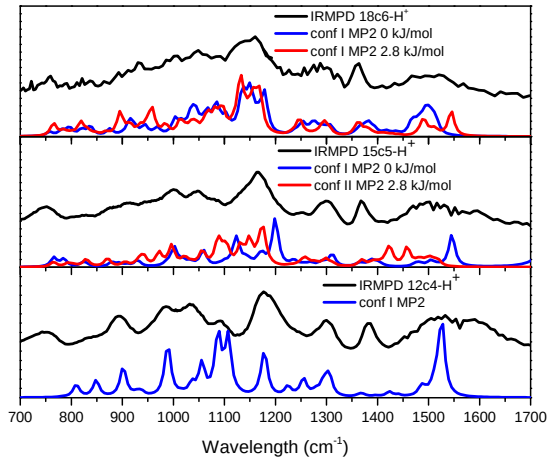

Figure 7.2: Experimental IRMPD spectra of the 18c6 complexes with H^+. Appreciable proton delocalization is observed as a broaded spectra. Computed MP2 harmonic spectra are shown for comparison.

C–O stretching band around 1100 cm^{-1} and less intense side bands within the range 700–1500 cm^{-1}. The position, shape and relative intensities of the different bands are qualitatively similar to those observed for the metal cation complexes of crown ethers and will be described in the following chapters. In the same Figure the corresponding harmonic IR spectra predicted by the MP2 computation, employing the conformers found in the conformational searching within 4.5 kJ/mol, is shown. It can be appreciated that the protonated 1-aza-18c6 and 2-aza-18c6 are in fair agreement with the experimental spectra.

Fig. 7.2 shows the analogous spectra recorded for the protonated native crown ethers 12c4, 15c5 and 18c6 and those obtained from MP2 conformers. Significant qualitative changes are observed in the vibrational structures of these spectra with respect to the N–substituted crown ethers. The IRMPD spectra of the three native crown ethers show a sequence of broadened bands that partially overlap with each other. The shape of the bands was reproducible as demonstrated in several repetitions of the experiments on different days and with different sample solutions. As we will see, the broadening of the IRMPD spectra is related to the formation of a proton bridge in the interior of the crown ring. Hence, the proton becomes delocalized in–between two oxygen atoms inducing a dynamic anharmonic coupling with the vibrational modes of the crown ether backbone. This is contrast to the situation in the aza-crowns in which the proton binds tightly to a single nitrogen atom.

Fig. 7.3 depicts the most stable molecular conformations predicted by the B3LYP computations for the whole set of protonated crown ethers considered in this study. It can be readily observed that in the native crown ether the proton forms a bridge connecting two oxygen atoms form opposite sides of the ring. In contrast, in the aza-crowns the proton is localized in a -(NH_2^+) group. The aza-crown backbone then adopts a folded conformation to facilitate the linear weak H-bonding of the a -(NH_2^+) group with two oxygen atoms from the ring as shown in that figure.

In the protonated native 12c4 ether, the most stable conformer is of C_s symmetry and displays a nearly linear coordination of the proton ($\widehat{OHO} \sim 164°$) with two opposing oxygens at O–H^+ distances between 1.0-1.5 Å. The remaining two oxygens of the ring stay at a larger distance from the proton (at about 2.4 Å) and orient the C-O-C dipoles perpendicular to the crown ring, hence weakly contributing to proton binding. In the 15c5 ether a similar proton bridge is formed (O-H^+ distances in the bridge between 1.10-1.35 Å), and the greater ring flexibility permits more favourable dipolar orientations of the non-bridged COC groups for moderate interaction with the proton (although from distances not smaller than 2.7 Å). The additional ether unit introduced when moving to the 18c6 ring leads to a further increase in backbone flexibility. Consequently, the 18c6 backbone has a significantly higher freedom than the 15c5 and 12c4 ones to accommodate the proton. The B3LYP two equilibrium conformations lowest energy, shown in Fig. 7.3, have the proton bridge between oxygen atoms either two or three monomers apart in the ring sequence (the latter case being more stable). The O–H^+ bridge distances lie within 1.0-1.5 Å and at least two adjacent COC groups

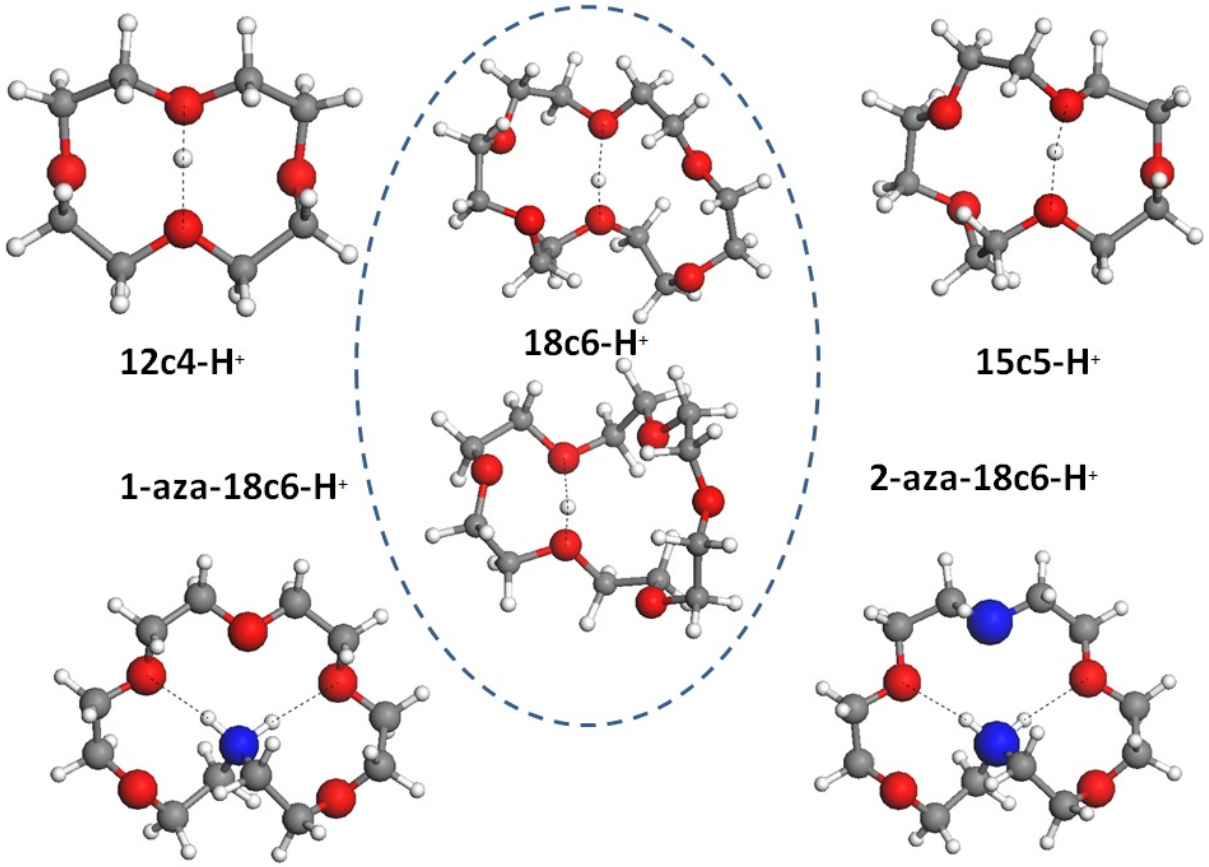

Figure 7.3: Lowest energy conformer obtained within harmonic DFT calculations. The proton bridge is marked as dashed lines in the crown ethers complexes. In the aza-crown ethers, the H-bonds formed between the protonated $-(NH_2^+)$ group and the oxygens atoms of the ring is also indicated by dashed lines.

orient their dipoles towards the proton from a distance of less than 3 Å away. It is interesting to note that the overall O-H$^+$-O bridge length in the three native crown ethers is of about 2.5 Å. The balance in the intramolecular charge-dipole interactions, together with the greater flexibility of the ether ring implying less conformational stress should be responsible for the increase in proton affinity observed for the native crown ethers with growing ring size [13, 4]. It seems needless to say that the N-substituted crowns here considered have a significantly higher proton affinity than the native ones.

The quantum nature of the proton bridge involves the delocalization of the proton via tunnelling in the region between the two oxygen atoms. In order to expose this dynamic behaviour, which is not captured in the equilibrium computations, we have carried out *ab initio* Molecular Dynamics calculations (AIMD) for the five protonated crown ether systems under study. The methodology of this approach has been described above and we will focus on the spatial distribution of the proton with respect to the oxygen and nitrogen atoms (if any) of the ring. Fig. 7.4 and Fig. 7.5 depict radial distributions representing i) the probability $F(r)$ of finding an O or N atom at a given distance from the proton (including the $2\pi r^2$ Jacobi factor), and ii) the cumulative distribution $n(r)$ obtained from direct integration of $F(r)dr$, reflecting the total number of O or N atoms found in average up to a certain distance form the proton. The narrow peak found for the N-substituted ethers in the $n(r)$ for N–H$^+$ indicates that the proton is localized at a distance of ca. 1 Å from the N atom to which it is bound. Consequently, $n(r)$ rises rapidly to 1 and, for the 2-aza-18c6 it proceeds to the asymptotic value of 2 only for distances greater than 3 Å. In contrast, the presence of a proton bridge in the native crown ethers reflects itself as a broad peak in $F(r)$ within the range 1–2 Å, and a rapid growth of $n(r)$ from 0 to 2. The $n(r)$ distribution then proceeds up to the total number of oxygens at a slower pace. The dynamic delocalization of the proton between the oxygen atoms was indeed visually obvious in the animations of the AIMD computations.

The dynamic coupling of the proton with the crown ether leads to a complex scenario in which the vibrational modes of the ring are strongly distorted. Harmonic computations of the vibrational spectrum are therefore not expected to be accurate. In fact, the IR spectrum predicted for any given equilibrium conformer was very much dependent on the level of theory employed. Furthermore, relatively small conformational changes led to substantial changes in the computational IR spectrum. This is indicative of a high sensitivity of the vibrational behavior of the crown ring with respect to the precise features of the proton bridge. At the room temperature of the present experiments, the ether backbone wanders among different low energy conformations due to the proton motion in the ring. At least for the protonated 18c6

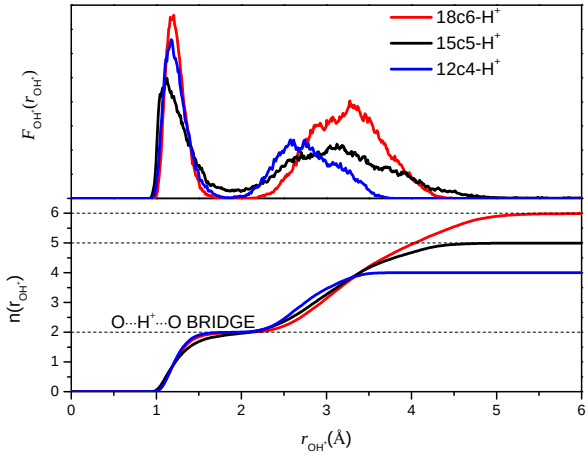

Figure 7.4: Radial distribution $F(r)$ and cumulative functions $n(r)$ of O-H$^+$ for the different crown ether systems studied in this work. The proton bridge is clearly observed in the cumulative function as a plateau in $n(r)$=2.

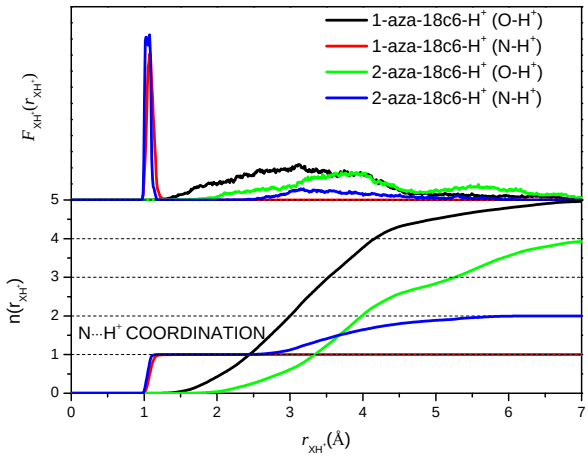

Figure 7.5: Radial distribution $F(r)$ and cumulative functions $n(r)$ of O-H$^+$ and N-H$^+$ for 18c6 and aza-derivatives ether systems considered in this study. The proton localization is clearly observed in the cumulative function as a plateau in $n(r)$=1.

ether, the combination of several low energy conformers reproduces fairly well the features of the IRMPD spectrum. This is however not the case for the smaller ethers, where de quantum effects of the proton bridge are expected to be ubiquotous in the whole ether cavity because of simple size effects. The Fig. 7.2 exposes the commented feaures for the protonated 18c6 model. it is observed that the combination of the MP2 conformers captured the more prominent features of the experimental IRMPD espectra. Although not shown, B3LYP calculations have also been performed and it should be noticed the strong influence of the method on the calculated IR spectra.

A proper description of the vibrational modes of the protonated crown ethers can in principle be obtained from sufficiently accurate and extensive AIMD computations. The atomic motions can be followed to compute velocity and dipole moment autocorrelation functions. The Fourier transform of those functions yields then the IR spectrum of the system. This approach has been employed in the past for proton bridged ethers and related systems and current work in our group is being devoted to perform the required computations. Whereas results are expected in the near term, such an advanced analysis falls outside the aim and time scope of this thesis work.

7.4 Conclusions

Experimental and theoretical methods have been combined in order tho shed light into the complexation of cyclic ethers with protons. This complexation process is relevant in protic solvents, and the elucidation of intramolecular forces in the whole phenomena is of relevant by itself. The preliminary results presented in this chapter permit to establish a different behavior for the native crown ethers in comparison to the aza-crowns variants derived from the substitution of one or two oxygen atoms for nitrogen atoms. Wile, the native crown ethers display a broadened IRMPD spectrum, the aza-crown ethers show narrower harmonic-like vibrational bands. Such spectroscopic features have been ascribed to proton localization in the later case and proton delocalization through bridge formation in the latter case. This behaviour can be expected to be relevant for the supramolecular properties of crown ethers in acidic environments. The proton affinities proposed in previous studies have been discussed in the light of the resulting intramolecular interactions. Future efforts should revisit these systems to provide a more quantitative microscopic rationalization based on systematic *ab initio* Molecular Dynamic simulations.

Bibliography

[1] a) J. O. Olovson. I. Acta Crystallogr. 23 (1967) 966; b) J. O. Olovson. I. Acta Crystallogr. B26 (1970) 1893.

[2] E. F. Valeev, H. F. Schaefer III. J. Chem. Phys. 108 (1998) 7197.

[3] M. George, V. S. Sebastian, P. Nagi Reddy, R. Srinivas, D. Giblin, M. L. Gross. J. Am. Soc. Mass Spectrom. 20(5) (2009) 805.

[4] H. Wasada, Y. Tsutsui, S. Yamabe. J. Phys. Chem. 100 (1996) 7367.

[5] P. Hurtado, F. Gámez, S. Hamad, B. Martínez-Haya, J.D. Steill, J. Oomens. J. Phys. Chem. A. 115 (2011) 7275.

[6] D. Adötoledo, V. Aviyente, J. M. L. Martin, C. Lifshitz. J. Phys. Chem. A. 102 (1998) 6357.

[7] T. D. Fridgen, L. MacAleese, T. B. McMahon, J. Lemaire, P. Maitre. Phys. Chem. Chem. Phys. 8 (2006) 955;

[8] W. Y. Feng, M. Goldenberg, C. Lifshitz. J. Am. Soc. Mass. Spectrom. 5 (1994) 695.

[9] A. Vila, R. A. Mosquera. Tetrahedron 57 (2001) 9415.

[10] M. Esseffar, M. Elmouhtadi, J. L. M. Abboud,J. Elguero, D. Liotard. Canadian J. Chem-Rev. 69 (1991) 1970.

[11] J. L. M. Abboud, J. Elguero, D. Liotard *et al*. J. Chem. Soc. Perkin Trans. 2 (1990) 565.

[12] C. Zhu, Y. Ling, W. Y. Feng, C. Lifshitz. Int. J. Mass Spectrom. 194 (2000) 93.

[13] R. B. Sharma, A. T. Blades, P. Kebarle. J. Am. Chem. Soc. 106 (1984) 510.

[14] a).- X. Li, J. Oomens, J. R. Eyler, D. T. Moore, S. S. Iyengar. J. Chem. Phys. 132 (2010) 1; b).- D. T. Moore, J. Oomens, L. van der Meer, G. von Helden, G. Meijer, J. Valle, A. G. Marshall, J. R. Eyler. ChemPhysChem. 5 (2004) 740.

[15] a) H. B. Schlegel, J. M. Millam, S. S. Iyengar, G. A. Voth, A. D. Daniels, G. E. Scuseria, M. J. Frisch. J. Chem. Phys. 114 (2001) 9758; b) S. S. Iyengar, H. B. Schlegel, J. M. Millam, G. A. Voth, G. E. Scuseria, M. J. J. Frisch. J. Chem. Phys. 115 (2001) 10291; H. B. Schlegel, S. S. Iyengar, X. Li, J. M. Millam, G. A. Voth, G. E. Scuseria, M. J Frisch. J. Chem. Phys. 117 (2002) 8694; (19) Iyengar, S. S.; Schlegel, H. B.; Voth, G. A.; Millam, J. M.; Scuseria, G. E.; M. J. Frisch. Israeli J. Chem. 42 (2002) 191.

Chapter 8

Vibrational study of isolated 18–crown–6 ether complexes with alkaline–earth metal cations

Laser infrared multiple photon dissociation (IRMPD) spectroscopy has been employed to probe the C–O and C–C stretching vibrational modes of 18–crown–6 ether (18c6) complexes with alkaline–earth metals (Mg^{2+}, Ca^{2+}, Sr^{2+} and Ba^{2+}) stored in the cell of a Fourier Transform Ion Cyclotron Resonance mass spectrometer. Computations at the B3LYP/6-311++G(2d,2p) and B3LYP/aug-cc-pVDZ levels of theory agree well with the most salient features of the experimental spectra and allow to characterize the lower energy conformers for each type of complex. A pronounced shift of the C–O stretching band, but not of the C–C band, is found in comparison to the similar IRMPD spectra reported previously for the 18c6 complexes with alkali metals. This is attributed to the tighter coordination and stronger binding of the divalent alkaline–earth cations to the oxygen sites, and to the degree of folding of the crown ether backbone. Nevertheless, the conformational landscape and symmetry constraints of the complexes follow a pattern similar to that found for the alkali metal cations. The most stable conformers evolve from compact D_2 geometries for the smaller cations, Mg^{2+} and Ca^{2+}, to more open C_2 configurations for Sr^{2+} and to a planar D_{3d} structure for Ba^{2+}.

8.1 Introduction

Crown ethers constitute one of the most prominent synthetic polymer models in guest–host chemistry, and are the building blocks for a broad range of modern materials [1, 2, 3]. Among the most salient properties of crown ethers stands their specific binding of cationic species. Binding selectivity is to a large extent dictated by the size of the cationic guest and the capability of the cyclic ether backbone to build a coordination shell optimizing the interaction of its electron donor oxygen sites with the cation [4, 5]. In this sense, crown ethers can be regarded as one of the simplest benchmark substrates resembling the general features of "key–pocket" inclusion complexes.

The ability of crown ethers to form charged complexes has also made them important characters in the development of mass spectrometric (MS) techniques. Early fragmentative MS/MS methods via laser excitation [6] or collisions [7, 8], as well as ion mobility methods [9], chose crown ethers as reference systems. In particular, infrared multiple photon dissociation (IRMPD) spectroscopy of crown-ether complexes as presented here follows up on some of the important contributions of John Eyler and his group, who studied crown ether cation complexes about two decades ago [6], and later became one of the pioneers in the use of free–electron laser (FEL) based IRMPD spectroscopy for structural analysis in mass spectrometry [10].

Most studies of crown ethers complexes have been devoted to singly charged guest species, primarily alkali metal cations [4, 5, 6, 7, 8, 9, 11, 12, 13, 14, 15, 16, 17, 18, 19, 20, 21, 22, 23, 24] and small molecular cations, such as oxonium, ammonium and protonated amines [25, 26, 27]. The complexation with multiply charged guest species, though less extensively investigated, has also been the subject of considerable attention since the early discovery of crown ethers [28, 29, 30, 31, 32, 33, 34, 35, 36, 37, 38, 39, 40]. In the mean time, crown ether moieties have been applied to the development of remarkably specific optical sensors of divalent cations [39, 40, 41].

Previous experimental studies of crown ether multivalent cationic complexes have been performed in solution, by means of calorimetry [28, 29], conductimetry [29, 30, 31], and nuclear magnetic resonance [32] techniques. Those studies have served to establish the relative stabilities of the complexes formed by crown ethers and cations of different sizes. For the alkaline–earth series Mg^{2+}–Ba^{2+}, a general trend of increasing stability with cation size was observed in solvents of different polarity (propylene carbonate, acetonitrile, nitromethane). This trend is exactly opposite to that followed by the corresponding isolated solvent–free complexes, for which crown–Mg^{2+} is most stable. This remarkable behavior has been rationalized from *ab initio* calculations by Glendening and Feller, in terms of the balance between the crown–cation–solvent non-covalent interactions [37]. The situation is, in fact, qualitatively similar to what is found for the alkali cation series Li^{+}–Cs^{+} [14, 15, 16]. In short, the heavier cations lead to complexes with more open crown ring structures for which solvation is facilitated without significant alteration of the coordination network built by the crown ether around the cation. On the other hand, the optimum cage-like arrangement formed by the crown with the lighter cations in the gas phase, is distorted in solution as the solvent gains access to the charge centre, thereby weakening the crown-metal binding. The results of recent experiments, employing state–of–the–art mass spectrometry and laser spectroscopy techniques to characterize gas–phase complexes, are consistent with such scenario. Those experiments have scoped isolated [4, 5, 22, 24] and hydrated [23] alkali metal cation complexes, as well as one benchmark divalent complex, namely (18–crown–6)–Mn^{2+} solvated by up to three methanol molecules [34].

In this study, we report on IRMPD laser vibrational spectroscopy of the alkaline–earth (Mg^{2+}–Ba^{2+}) complexes of 18–crown–6 crown ether (18c6) isolated in an ion cyclotron resonance mass spectrometer. The strategy of the investigation mimics that applied for the alkali cation series in previous works [4, 5, 21]. The mid–infrared radiation of a free–electron laser is employed to probe the C–O and C–C stretching modes of the complexes. Details of the experimental method are provided in Sect. 8.2, together with a description of the computational approach employed to characterize the molecular structures. The results are then discussed and summarized in the subsequent Sects. 8.3 and 8.4.

8.2 Methods

8.2.1 ESI-FTICR IRMPD spectroscopy

Infrared multiple photon dissociation spectra were recorded using a Fourier transform ion cyclotron resonance (FT—ICR) mass spectrometer [42], coupled to the beamline of the free electron laser FELIX [43, 44]. The ionic complexes are produced by electrospray ionization of 1 mM solutions of crown ether and alkaline–earth salt in a water/methanol mixture. Ions are accumulated in a hexapole ion trap and then pulse injected into the ICR cell, where they are mass isolated and irradiated with typically 10 FELIX macro–pulses. Each macro–pulse is approximately 5 microsecond long, has an energy of about 35 mJ, and consists of trains of micro–pulses with a repetition frequency of 1 GHz. The spectral bandwidth of the radiation amounts to 0.5% of the central wavelength. Further description of typical experimental

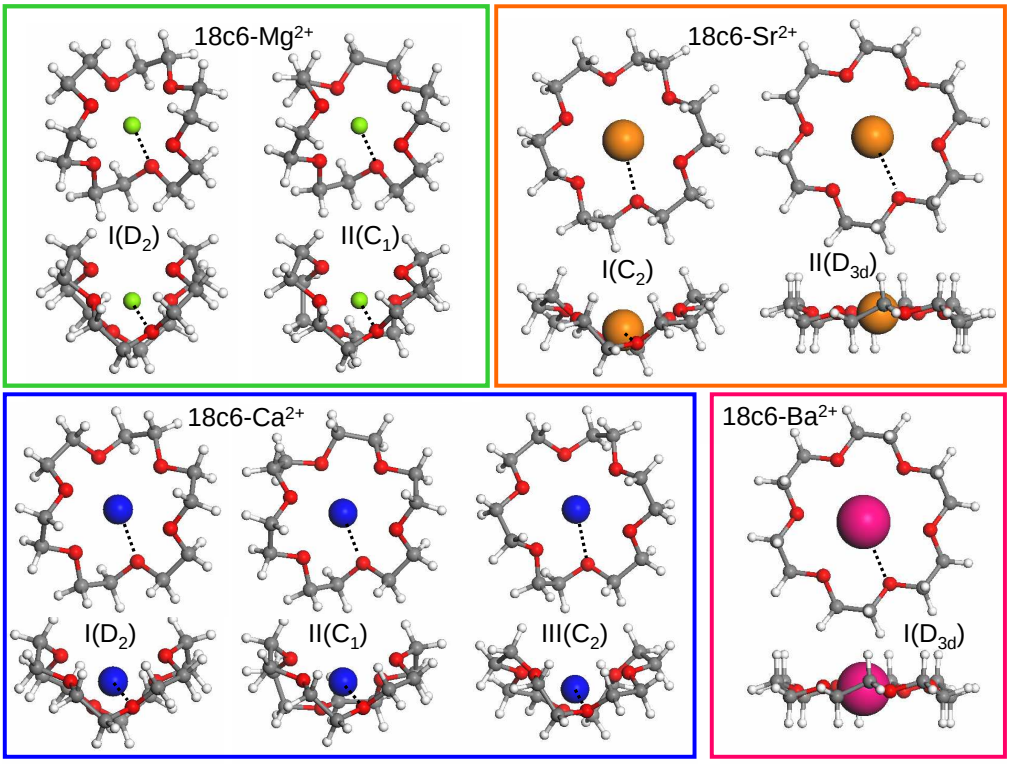

Figure 8.2: Representation of the most stable B3LYP conformers of the 18c6–M^{2+} complexes included in this study. See Table 8.2 for the relative energies of the conformers. The oxygen atom marked with a dashed binding line to the cation serves as starting point for the (clockwise) sequence of geometrical parameters listed in Table 8.3 for each conformer.

procedures can be found in ref. [45].

When the infrared wavelength of the laser is in resonance with a vibrational mode of the complex, sequential multiple photon absorption occurs eventually leading to dissociation of the parent ion. The IRMPD spectrum is constructed by monitoring the total fragment yield, as a function of the wavenumber of the radiation. The intense C–O stretching band was repeatedly probed at several attenuated laser powers in order to avoid potential saturation effects due to depletion of complexes in the laser beam path. The recorded spectra were linearly corrected for the changes in laser pulse energy, in consonance with the non–coherent multiple photon dissociation mechanism driving IRMPD [46].

Table 8.1 lists the dominant IRMPD fragment ions observed at the maxima of the C–O and C–C stretching bands of each of the alkaline–earth complexes. The relative abundances are obtained from the ratios between the observed intensities for the given fragment and for the parent ion in the mass spectra. Products of three types are observed, namely X-M^{2+}, X–M^{+} and X^{+}, where M denotes the alkaline–earth metal and X an ether fragment. The assignment of 2+ or 1+ charges are consistently supported by the isotopic spacings in the mass spectra.

The $(CH_2CH_2O)_n$–M^{2+} IRMPD products are related to the loss of CH_2CH_2O units through C–O bond cleavages in the crown ring of the parent complex:

$$(CH_2CH_2O)_6\text{–}M^{2+} \longrightarrow (CH_2CH_2O)_k + (CH_2CH_2O)_{6-k}\text{–}M^{2+} \qquad (8.1)$$

On the other hand, the X–M^{+} and X^{+} products must arise from a charge transfer mechanism, involving the reduction of the guest cation to a 1+ charge state. All four alkaline–earth complexes display products of the form $[HO\text{–}(CH_2CH_2O)_{n=2,1,0}]\text{–}M^{+}$, and have in common the three ionic ether fragments $[(CH_2CH_2O)\text{–}CH_2CH]^{+}$ (m/z= 71), $[CH_2CH_2OH]^{+}$ (m/z= 45) and $[OCH_2CH]^{+}$ (m/z= 43). The observation of these common products lends support to a common fragmentative route for the four complexes, in which the initial step would be C–O bond cleavage, concerted with reduction of the divalent cation and with the transfer of one H atom from the $\text{–}CH_2\text{–}CH_2\text{–}$ moiety to the O–end of the

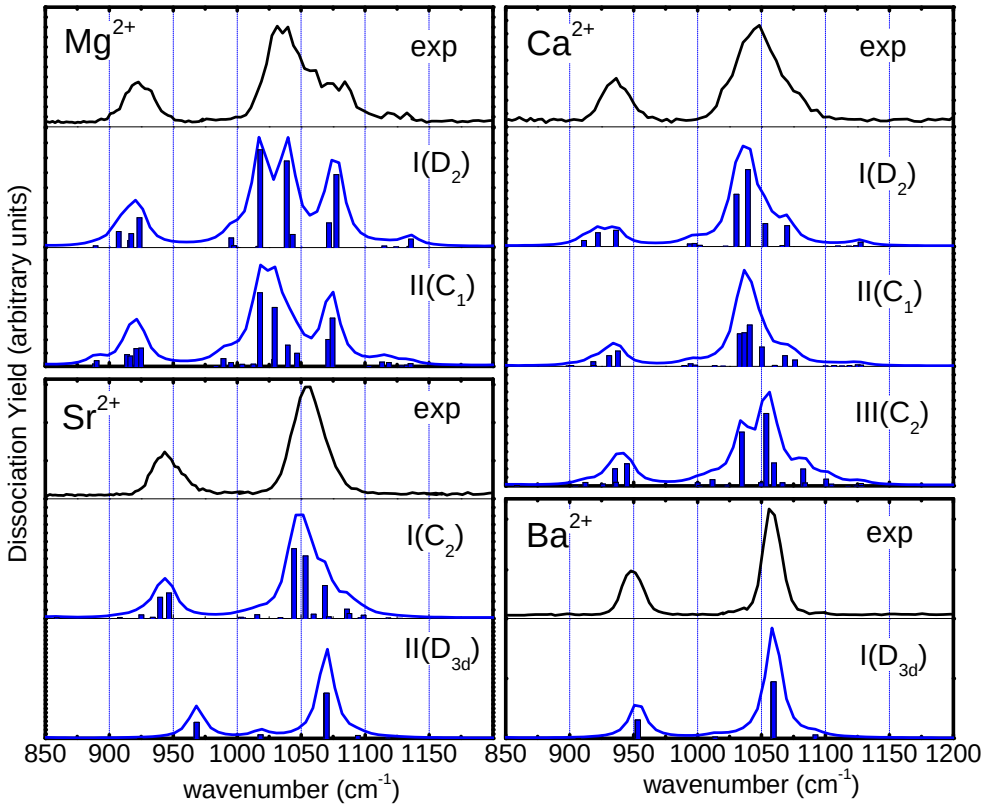

Figure 8.3: Comparison of the experimental IRMPD spectra with the harmonic IR spectra predicted by the B3LYP/6-311++G(2d,2p) computation for the low lying conformers of the 18c6–M^+ complexes. See Table 8.2 for the notation and relative energies between the different conformers. The nominal computed vibrational frequencies (scaled by a factor 0.98) are indicated as histograms. The simulated B3LYP spectra are built via convolution with a lorentzian broadening of 8 cm^{-1} (full–with–half–maximum).

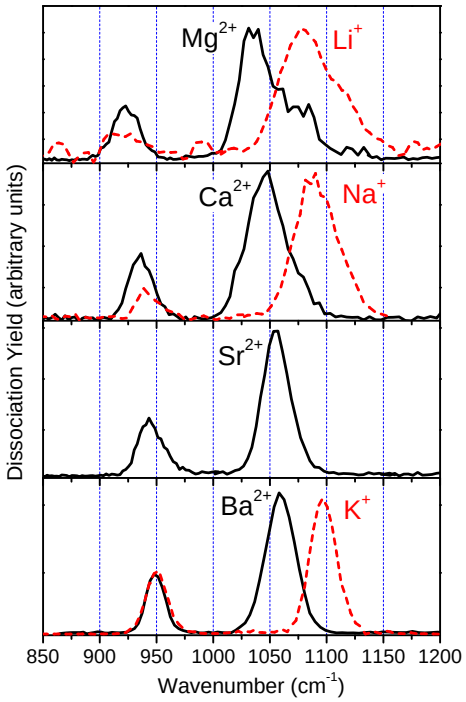

Figure 8.1: Experimental IRMPD spectra of the 18c6 complexes with the four alkaline–earth cations included in this study (solid lines). The spectra of the corresponding 18c6 complexes with the alkali cations of similar ionic radius from ref. [4] are included for comparison (dashed lines). Note the significant red shift of the C–O band (but not of the C–C band) of the alkaline–earth complexes in comparison to their alkali analogs.

nascent fragment:

$$(CH_2CH_2O)_6\text{–}M^{2+} \longrightarrow [(CH_2CH_2O)_{k-1}\text{–}CH_2CH]^+ + HO\text{–}(CH_2CH_2O)_{6-k}\text{–}M^+ \quad (8.2)$$

According to the relative fragment abundances listed in Table 8.1, this latter type of dissociation mechanism dominates the IRMPD process.

Fig. 8.1 shows the IRMPD spectra measured for 18c6—M^{2+} (M = Mg, Ca, Sr, Ba). The spectra of the four complexes feature two differentiated bands associated with vibrational modes dominated by C-–C (900—1000 cm^{-1}) and C-–O (1000—1150 cm^{-1}) stretching. Weaker bands related to COC angle bending and to CH_2 wagging, torsions and bending, that were visible within 600–1800 cm^{-1} in the similar experiments for the alkali cation complexes of 18c6 [4], could not be detected in the present case. The lack of sensitivity to these latter bands is due to the high binding energy of the alkaline–earth complexes, leading to a roughly three–fold greater endothermicity for dissociation in comparison to the alkali metal counterparts [16, 37]. Nevertheless, it will be shown that the C–C and C–O bands provide valuable information about the conformational geometry of the complexes, and serve to validate the predictions of the B3LYP computations.

8.2.2 Quantum Chemistry calculations

A conformational survey of the 18c6–M^{2+} complexes was performed by means of simulated annealing with the Universal force–field [47]. In addition, the complete set of low energy conformers found for the 18c6 complexes with the alkali cation series in our previous study [4] was considered for reoptimization with the alkaline–earth cations as guests.

Geometry optimizations of the structures were performed using Density Functional Theory (DFT) with the B3LYP hybrid functional [48]. For the heavier alkaline–earth cations (Sr^{2+} and Ba^{2+}) the core electrons were treated with the Stuttgart/Dresden effective core potentials [49], whereas Gaussian-type orbitals were used for the valence shells. The C, O, H and lighter alkaline–earth atoms were modelled with the all–electron 6-311++G(2d,2p) or aug–cc–pVDZ basis sets. In order to reduce the basis set superposition error, the counterpoise method [50] was applied. The calculations were carried out with the Gaussian 09 code [51].

All the energies reported are free energies, calculated as the sum of electronic energies plus corrections due to

Table 8.1: IRMPD products observed for the 18–crown–6 alkaline–earth complexes scoped in this study. The first line for each cation corresponds to the parent complex. The relative product abundances are obtained from the ratio of the intensity of each fragment to the intensity of the parent complex ion recorded on the maxima of the C–O and C–C stretching bands. Fragment intensities with the laser off resonance were negligible in all cases. For each alkaline–earth cation, the fragments are ordered from top to bottom according to their charge and metal cation content.

m/z	assignment	relative abundances C–O band	C–C band
18c6-Mg^{2+}			
144	$[(CH_2CH_2O)_6]$–Mg^{2+}	1.00	1.00
122	$[(CH_2CH_2O)_5]$–Mg^{2+}	0.21	0.25
129	$[HO–(CH_2CH_2O)_2]$–Mg^{+}	0.16	0.11
85	$[HO–(CH_2CH_2O)]$–Mg^{+}	0.63	0.14
41	$[HO]$–Mg^{+}	0.12	0.03
71	$[(CH_2CH_2O)–CH_2CH]^{+}$	0.37	0.12
45	$[CH_2CH_2OH]^{+}$	0.41	0.09
43	$[OCH_2CH]^{+}$	0.38	0.10
18c6-Ca^{2+}			
152	$[(CH_2CH_2O)_6]$–Ca^{2+}	1.00	1.00
130	$[(CH_2CH_2O)_5]$–Ca^{2+}	0.08	0.07
145	$[HO–(CH_2CH_2O)_2]$–Ca^{+}	0.18	0.10
101	$[HO–(CH_2CH_2O)]$–Ca^{+}	0.33	0.07
57	$[HO]$–Ca^{+}	0.27	0.03
71	$[(CH_2CH_2O)–CH_2CH]^{+}$	0.24	0.09
45	$[CH_2CH_2OH]^{+}$	0.10	0.02
43	$[OCH_2CH]^{+}$	0.20	0.05
18c6-Sr^{2+}			
176	$[(CH_2CH_2O)_6]$–Sr^{2+}	1.00	1.00
66	$[CH_2CH_2O]$–Sr^{2+}	0.14	0.02
193	$[HO–(CH_2CH_2O)_2]$–Sr^{+}	0.33	0.18
149	$[HO–(CH_2CH_2O)]$–Sr^{+}	0.49	0.11
105	$[HO]$–Sr^{+}	0.54	0.04
71	$[(CH_2CH_2O)–CH_2CH]^{+}$	0.49	0.14
45	$[CH_2CH_2OH]^{+}$	0.18	0.04
43	$[OCH_2CH]^{+}$	0.35	0.09
18c6-Ba^{2+}			
201	$[(CH_2CH_2O)_6]$–Ba^{2+}	1.00	1.00
91	$[CH_2CH_2O]$–Ba^{2+}	0.19	0.05
287	$[HO–(CH_2CH_2O)_3]$–Ba^{+}	0.09	0.10
243	$[HO–(CH_2CH_2O)_2]$–Ba^{+}	0.31	0.19
199	$[HO–(CH_2CH_2O)]$–Ba^{+}	0.31	0.05
155	$[HO]$–Ba^{+}	0.54	0.00
71	$[(CH_2CH_2O)–CH_2CH]^{+}$	0.67	0.17
45	$[CH_2CH_2OH]^{+}$	0.14	0.04
43	$[OCH_2CH]^{+}$	0.33	0.08

the vibrational zero–point energies and thermal entropy contributions. The B3LYP/6-311++G(2d,2p) harmonic IR spectra shown in the chapter were calculated from the convolution of the normal modes of vibration of the optimized structures, with a line broadening of 8 cm^{-1}. The computed vibrational frequencies for all the complexes were scaled for comparison with experiment by a factor 0.98, in line with the scaling recommended in previous studies [52].

Table 8.2 lists the B3LYP free energies of the most stable conformers found in our conformational search for the 18c6–M^{2+} complexes. In addition, Fig. 10.5 and Table 8.3 describe the molecular geometries of the lowest lying conformers that presumably contribute to the IRMPD signal in the present experiments. Finally, Fig. 8.3 depicts the harmonic IR spectra predicted by the B3LYP/6-311++G(2d,2p) computation for these latter conformers and compares them with the recorded IRMPD spectra.

8.3 Results

Fig. 8.1 compares the IRMPD spectra recorded here for the alkaline–earth complexes with the corresponding spectra of their alkali analogs from ref. [4]. The ionic radii of the alkaline earth cations Mg^{2+}, Ca^{2+}, Sr^{2+} and Ba^{2+} are 0.72, 1.00, 1.18 and 1.35 Å, respectively. Those of the alkali cations Li^+, Na^+, K^+ and Cs^+ are 0.76, 1.02, 1.38 and 1.67 Å. Hence, Mg^{2+}, Ca^{2+} and Ba^{2+} are roughly similar in size to Li^+, Na^+ and K^+, respectively, and the IRMPD spectra for these cations are compared in Fig. 8.1. Note that the 18c6–Sr^{2+} complex is not included in the comparison, since the size of Sr^{2+} lies in between Na^+ and K^+.

The tighter binding of the divalent alkaline–earth cations leads to a red shift by *ca.* 40 cm^{-1} of the C–O stretching band with respect to the corresponding band of the complex involving the alkali cation of similar size. Noticeably, the C–C bands are not affected by any appreciable shift when the alkaline–earth and alkali cations are interchanged. This observation was not necessarily expected, as the dragging of charge to the oxygen sites induced by the divalent also affects the bond strength of the C–C moieties. As it turns out, the frequency of the C–C stretching modes rather seems to be primarily driven by the degree of folding and dihedral distortion of the ether backbone. The similarity of the position of the C–C stretching bands when increasing the cation charge from 1+ to 2+, while keeping the cation size constant, can then be taken as a hint for similar molecular conformations in the complexes. It can be noted that the C–C band shifts by *ca.* 40 cm^{-1} to the blue in going from the Mg^{2+} complex to the Ba^{2+} complex, and this behavior can be foreseen to follow from the transition from a folded cage–like conformation for Mg^{2+} to a less distorted quasi–planar one for Ba^{2+}. Note also that the C–O band shifts less markedly, by *ca.* 20 cm^{-1}, in going from Mg^{2+} to Ba^{2+}, in this case as a consequence of the decrease in binding interaction with cation size.

The detailed shape of the C–O stretching band in the IRMPD spectra constitutes a key feature in this study which provides further support to the considerations outlined above. The C–O band of the 18c6–Mg^{2+} complex is particular broad and structured, suggesting the contribution of several distinct vibrational modes and/or of various conformers. As the size of the cation increases, the C–O band becomes progressively narrower, reaching a full-width-at-half-maximum as small as 18 cm^{-1} in the 18c6–Ba^{2+} complex. This particularly narrow band plausibly arises from a highly symmetric backbone conformation with identical oxygens, in which the C–O stretching modes are merged into a single degenerate mode. A qualitatively similar overall trend was found in the IRMPD spectra of the alkali cation complexes of 18c6 (see Fig. 8.1), which suggests that 18c6–Ba^{2+} presumably stabilizes in a D_{3d} configuration similar to that of 18c6–K^+ [4]. It will be shown below that the B3LYP computations are in agreement with this expectation.

We incorporate at this point the computational study to the discussion in order to obtain a more involved insight into the experimental results. Table 8.2 shows that the conformational landscape of the complexes is governed by symmetric molecular arrangements. With decreasing cation size, the geometry of the complex evolves from a planar D_{3d} conformation for 18c6—Ba^{2+}, to a folded C_2 structure for 18c6—Sr^{2+}, and to progressively more folded cage–like D_2 structures for 18c6—Ca^{2+} and 18c6—Mg^{2+}. The relevance of symmetric conformations in the complexation of 18c6 with metal cations was already a central theme in previous studies [4, 35, 36]. Remarkably, the D_2 and C_2 geometries are chiral, thereby rendering atropoisomerism as a key feature to the conformational landscape of the system. The term atropoisomerism refers to chirality as an emerging property, arising upon complexation of the crown ether with the cation [53].

The detailed analysis of the IRMPD spectra serves to asset the contribution of the low lying conformers predicted by the B3LYP computations. We begin with the discussion of the 18c6-–Ba^{2+} complex, for which the planar D_{3d} conformer fully accounts for the narrow C–C and C–O bands observed experimentally (see Fig. 8.3). The computed stretching modes involved in these bands essentially merge into a single degenerate vibrational line, due to the equivalence of the ether groups in this highly symmetric arrangement. According to the present computations, the next excited conformer is a C_2 structure that lies more than 12 $kJ\,mol^{-1}$ higher and is not

expected to have a relevant population in the experiments. In comparison to the similar D_{3d} conformer for the 18c6–K^+ complex [4], the crown cavity is slightly more stretched toward the cation in 18c6-–Ba^{2+} (the O–M distance is smaller by 0.05 Å), due to the higher charge of guest cation. As already mentioned, the open configuration of the quasi–planar D_{3d} conformer is quite relevant for the behavior of the complex in solution, as it facilitates the solvation of the cation guest. For this reason, in polar solvents 18c6-–Ba^{2+} and 18c6–K^+ turn out to be the most stable complexes among the alkaline–earth and alkali cation series, respectively [37].

For the 18c6-–Sr^{2+} complex, the B3LYP computation leads to a C_2 ground state conformer, whereas the planar D_{3d} conformer is predicted to lie within one k_BT thermal unit higher in energy. The comparison of the B3LYP IR spectra for these two conformers with the IRMPD measurements confirms that the C_2 complex alone reproduces the position and overall envelope of the experimental C–C and C–O stretching bands. In fact, the IRMPD spectrum rules out a relevant contribution from the D_{3d} conformer. Only a small contribution (of less than 20 % in relative weight) from this latter conformer to the blue flank of the bands would still be compatible with experiment. However, the B3LYP computations predict a free energy within 2–3 kJ mol^{-1} for the D_{3d} conformer, which corresponds to Boltzmann weights of 30–45 %. Hence, it appears that the B3LYP computation overestimates the stability of the D_{3d} conformer against the folded configurations; it seems timely to remark this finding since a similar overestimation was found for the 18c6–Na^+ complex in our previous work [4].

The 18c6—Ca^{2+} complex is predicted to be most stable in a symmetric folded D_2 conformation, and in two close lying conformers of C_1 and C_2 symmetry. The C_2 conformer III is qualitatively similar to the most stable 18c6-–Sr^{2+} structure, although it becomes more folded with the reduced size of the Ca^{2+} cation. Fig. 8.3 shows that the experiment is consistent with a joint contribution from these three conformers. Whereas the B3LYP IR spectrum of the D_2 conformer accounts for the main features of the experimental IRMPD spectrum, it however underestimates the signal observed on the blue flank of the C–C and C–O bands, in particular above 950 and 1050 cm^{-1}, respectively. The expected contribution of the C_1 conformer does not solve this problem, as the predicted IR spectrum is similar to the one of the D_2 conformer. The C_2 conformer does provide the required intensity so that an appreciable contribution from this conformer, not smaller than 50 percent in relative abundance, is required in order to reproduce the IRMPD spectrum.

Finally, the 18c6—Mg^{2+} complex displays the broadest and most structured bands of the series. The B3LYP computations predict folded D_2 and C_1 conformers as most stable. These two conformers resemble those with the same symmetries found for the 18c6—Ca^{2+} complex. However, for the 18c6—Mg^{2+} system the folding of the crown ring is almost complete, so that the ether chain virtually cages the cation and isolates it from the outer environment. The next higher conformer lies more than 7 kJ mol^{-1} above the D_2 conformer and should not contribute to the experiment. The related cage–like conformer of S_6 symmetry investigated by Glendening and Feller for this system [37] lies more than 50 kJ mol^{-1} higher in energy. The B3LYP IR spectra of the D_2 and C_1 conformers shown in Fig. 8.3 readily relate the structure of the C–O band to a marked splitting of the C–O stretching modes into three main components in the folded arrangements. In fact, the experimental IRMPD spectrum correlates well with a 1:1 combination of the spectra of the two conformers.

Overall, the optimum molecular arrangement of the different complexes results from the balance between the oxygen–metal attractions, the oxygen–oxygen repulsions and the flexibility of the crown ring. Taking the lowest energy conformers for each cation as reference, the average O–M^{2+} distances in alkaline–earth complexes are of 2.13, 2.40, 2.61 and 2.77 Å for M = Mg, Ca, Sr and Ba, respectively (see Table 8.3). Such average distances are remarkably close to the optimum O–M^{2+} coordination distances of the hydrated alkaline–earth cations, namely lying within 1.94–2.11, 2.30–2.44, 2.46–2.61 and 2.66–2.83 Å for Mg, Ca, Sr and Ba, respectively [37, 54, 55].

A noticeable difference between the alkaline–earth and alkali cation complexes arises in the stability of the cage–like D_2 conformer. The tighter bonding induced by the divalent guests works in favour of the D_2 conformation. Indeed, whereas the D_2 conformer constitutes the most stable arrangement for 18c6—Mg^{2+}, 18c6—Ca^{2+} and 18c6—Li^+, this is not the case for 18c6—Na^+. This latter complex displays a C_1 partially folded conformer, followed in stability by the planar D_{3d} structure [4]. Hence, in spite of Na^+ having a similar ionic radius as Ca^{2+}, its single charge does not manage to stabilize the symmetric folding of the crown ether backbone.

8.4 Conclusions

FT–ICR mass spectrometry and FEL–based IRMPD spectroscopy have been employed to provide new insights into the conformational characteristics of the gas–phase complexes formed by 18–crown–6 with the alkaline–earth cations Mg^{2+}, Ca^{2+}, Sr^{2+} and Ba^{2+}. The position and structure of the C–C and C–O stretching bands observed in the IRMPD spectra, in combination with B3LYP computations have served to support a conformational landscape dominated by symmetric molec-

ular arrangements in the complexes. The most stable conformers evolve from compact D_2 geometries for the smaller cations, Mg^{2+} and Ca^{2+}, to a more open C_2 configuration for Sr^{2+} and to a planar D_{3d} structure for Ba^{2+}. Further low lying conformers of C_2 and C_1 symmetry contribute to the present room temperature experiments.

Such trends and symmetry constraints are similar to those found in previous studies for the analogous complexes of 18c6 with the alkali cations [4]. When comparing the IRMPD spectra of the 18c6 complexes with alkaline–earth and alkali cations of similar ionic radius, coincidence is found for the position and width of the C–C stretching band, which can be related to the similar degree of folding undergone by the crown backbone. On the other hand, a pronounced red shift is found for the C–O stretching band of the alkaline–earth spectra with respect to the alkali counterparts, as a natural consequence of the tighter binding of the divalent alkaline–earth cations to the oxygen sites of the ether. The C–O and C–C stretching band positions are well reproduced by the B3LYP computations. The higher charge state of the alkaline–earth cations also enhances the stability of the folded D_2 arrangement, as follows from the comparison of the 18c6–Ca^{2+} (most stable D_2 conformer) and 18c6–Na^{+} (most stable C_1 conformer) complexes.

The open configuration of the quasi–planar D_{3d} conformer found for 18c6-–Ba^{2+} is similar to the one displayed by the 18c6-–K^{+} complex [4]. Such conformation is of key relevance for the behavior of these complexes in solution, as it leads to a facile solvation of the cation. In contrast, the folded conformations adopted by the complexes of the lighter cations must be significantly distorted in order to provide access of the solvent to the cation. As a consequence, 18c6-–Ba^{2+} and 18c6–K^{+} are the most stable complexes among the alkaline–earth and alkali cation series in polar solvents [15, 37]. We note in closing that the open ether ring structures are as well suitable for the formation of selective ternary complexes, in which two crown ethers are bridged by one guest cation [21, 33, 56, 57].

Table 8.2: Free energies (kJ mol^{-1}) of the 18c6–M^{2+} conformers relevant to the present study. B3LYP/6–311++G(2d,2p) and B3LYP/aug–cc–pVDZ levels of theory are compared. The point symmetry group to which each conformer belongs is indicated. See Fig. 10.5 and Table 8.3 for a description of the molecular structure of the most stable conformers. Note that at the room temperature of the present experiments, one k_BT thermal unit equals ~ 2.5 kJ mol^{-1}.

Conformer	Symmetry Group	B3LYP 6–311++G(2d,2p)	B3LYP aug–cc–pVDZ
18c6-Mg^{2+}			
I	D_2	0	0
II	C_1	2.0	1.5
III	C_2	8.2	7.4
18c6-Ca^{2+}			
I	D_2	0	0
II	C_1	2.8	2.1
III	C_2	3.3	1.5
IV	C_2	8.0	8.2
18c6-Sr^{2+}			
I	C_2	0	0
II	D_{3d}	2.1	2.8
III	C_2	6.2	5.0
18c6-Ba^{2+}			
I	D_{3d}	0	0
II	C_2	14.2	12.6

Table 8.3: Selected geometrical parameters of the most stable 18c6–M^{2+} conformers (M= Mg, Ca, Sr, Ba) predicted by the B3LYP/6-311++G(2d,2p) computations. See Table 8.2 for the relative energies of the different conformers, and Fig. 10.5 for a representation of their structure. The set of distances (in Å) and angles (in degrees) starts with the oxygen atom marked with a dashed O–M binding line in Fig. 10.5, and proceeds clockwise.

Conformer	**O–M distances**	**O–O distances**	**C–O–C angles**	**O–C–C–O dihedral angles**
18c6–Mg^{2+}				
I(D_2)	2.14, 2.11, 2.14, 2.14, 2.11, 2.14	2.56, 2.56, 2.69, 2.56, 2.56, 2.69	113.8, 117.4, 113.8, 113.8, 117.4, 113.8	38.5, 38.5, 54.2, 38.5, 38.5, 54.2
II(C_1)	2.15, 2.11, 2.14, 2.14, 2.10, 2.14	2.56, 2.57, 2.74, 2.58, 2.62, 2.67	114.1, 117.5, 117.0, 113.7, 116.9, 113.6	38.4, 38.9, -47.8, -45.8, 47.6, 53.2
18c6–Ca^{2+}				
I(D_2)	2.41, 2.39, 2.41, 2.41, 2.39, 2.41	2.67, 2.67, 2.73, 2.67, 2.67, 2.73	115.6, 116.4, 115.6, 115.6, 116.4, 115.6	44.7, 44.7, 57.6, 44.7, 44.7, 57.6
II(C_1)	2.42, 2.41, 2.40, 2.42, 2.41, 2.42	2.67, 2.63, 2.71, 2.69, 2.71, 2.72	115.2, 115.9, 119.2, 114.7, 115.0, 114.9	45.0, 43.7, -47.2, -53.5, 51.8, 56.7
III(C_2)	2.48, 2.41, 2.49, 2.48, 2.41, 2.49	2.66, 2.62, 2.72, 2.66, 2.62, 2.72	113.1, 117.9, 111.9, 113.1, 117.9, 111.9,	49.1, -48.3, 54.9, 49.1, -48.3, 54.9
18c6–Sr^{2+}				
I(C_2)	2,62, 2.59, 2.63, 2,62, 2.59, 2.63	2.74, 2.70, 2.75, 2.74, 2.70, 2.75	114.1, 115.1, 111.7, 114.1, 115.1, 111.7	53.7, -52.6, -56.7, 53.7, -52.6, -56.7
II(D_{3d})	2.69, 2.69, 2.69, 2.69, 2.69, 2.69	2.69, 2.69, 2.69 2.69, 2.69, 2.69	112.4, 112.4, 112.4, 112.4, 112.4, 112.4	-54.2, 54.2, -54.2, 54.2, -54.2, 54.2
18c6–Ba^{2+}				
I(D_{3d})	2.77, 2.77, 2.77, 2.77, 2.77, 2.77	2.78, 2.78, 2.78 2.78, 2.78, 2.78	113.1, 113.1, 113.1, 113.1, 113.1, 113.1	-57.6, 57.6, -57.6, 57.6, -57.6, 57.6

Bibliography

[1] C.J. Pedersen, The Discovery of Crown Ethers, Science 241 (1988) 536–540

[2] G.W. Gokel, Crown ethers and cryptands, Royal Society of Chemistry (1994), ISBN-13: 978-0851867045

[3] J.W. Steed. Coord. Chem. Rev. 215 (2001) 171.

[4] B. Martínez–Haya, P. Hurtado, A.R. Hortal, S. Hamad, J.D. Steill, J. Oomens. 114 J. Phys. Chem. A. (2010) 7048.

[5] P. Hurtado, A.R. Hortal, F. Gámez, S. Hamad, B. Martínez–Haya. Phys. Chem. Chem. Phys. 12 (2010) 13752.

[6] D.M. Peiris, Y. Yang, R. Ramanathan, K.R. Williams, C. Watson, J.R. Eyler. Int. J. Mass Spectrom. Ion Processes. 157/158 (1996) 365.

[7] P.B. Armentrout. Int. J. Mass Spectrom. 193 (1999) 227.

[8] J.S. Brodbelt. Int. J. Mass Spectrom. 200 (2000) 57.

[9] S. Lee, T. Wyttenbach, G. von Helden, M.T. Bowers. J. Am. Chem. Soc. 117 (1995) 10159.

[10] D.T. Moore, J. Oomens, L. van der Meer, G. von Helden, G. Meijer, J. Valle, A.G. Marshall, J.R. Eyler. Chem. Phys. Chem. 5 (2004) 740.

[11] S.M. Blair, E.C. Kempen, J. Brodbelt. J. Am. Soc. Mass Spectrom. 9 (1998) 1049.

[12] J.D. Anderson, E.S. Paulsen, D. Dearden. Int. J. Mass Spectrometry. 227 (2003) 63.

[13] S. Maleknia, J. Brodbelt. J. Am. Chem. Soc., 114 (1992) 4295.

[14] M.B. More, D. Ray, P.B. Armentrout. J. Am. Chem. Soc. 127 (1999) 417.

[15] D. Feller. J. Phys. Chem. A. 101 (1997) 2723.

[16] E.D. Glendening, D. Feller, M.A. Thomson. J. Am. Chem. Soc. 116 (1994) 10657.

[17] S. Al–Rusaese, A.A. Al–Kahtani, A.A. El–Ahzhary. J. Phys. Chem. A. 110 (2006) 8676.

[18] M. Gajewski, J. Tuszynski, H. Mori, E. Miyoshi, M. Klobukowski. Inorg. Chim. Acta 361 (2008) 2166.

[19] S. De, A. Boda, M. Ali. J. Mol. Struct. (Theochem) 941 (2010) 90.

[20] A.R. Hortal, P. Hurtado, B. Martínez–Haya, A. Arregui, L. Bañares. J. Phys. Chem. B. 112 (2008) 8530.

[21] B. Martínez–Haya, P. Hurtado, A.R. Hortal, J.D. Steill, J. Oomens, P.J. Merkling. J. Phys. Chem. A. 113 (2009) 7748.

[22] J.D. Rodriguez, J.M. Lisy. Int. J. Mass Spectrom. 283 (2009) 135.

[23] J.D. Rodriguez, T.D. Vaden, J.M. Lisy. J. Am. Chem. Soc. 131 (2009) 17277.

[24] J.D. Rodriguez, D. Kim, P. Tarakeshbar, J.M. Lisy. J. Phys. Chem. A. 114 (2010) 1514.

[25] P. Hurtado, F. Gámez, S. Hamad, B. Martínez–Haya, J.D. Steill, J. Oomens. J. Phys. Chem. A. 115 (2011)7275.

[26] P.C. Junk. New J. Chem. 32 (2008) 762.

[27] M. Schäfer. Angew. Chem. Int. Ed. 42 (2003) 1896.

[28] R.M. Izatt, R.E. Terry, B.L. Haymore, L.D. Hansen, N.K. Dalley, A.G. Ayondet, J.J. Christensen. J. Am. Chem. Soc. 24 (1974) 7620.

[29] H.-J. Buschmann, E. Schollmeyer. Thermochimica Acta. 211 (1992) 13.

[30] M. Shamsipur, N. Tavakkoli. Pol. J. Chem. 78 (2004) 109.

[31] G.H. Rounaghi, F. Mofazzeli. J. Incl. Phen. Macrocyclic Chem. 51 (2005) 205.

[32] E. Karkhaneei, M.H. Zebarjadian, M. Shamsipur. J. Sol. Chem. 30 (2001) 323.

[33] N. Shen, R.M. Pope, D.V. Dearden. Int. J. Mass Spectrom. 195-196 (2000) 639.

[34] J.D. Rodriguez, J.M. Lisy. J. Phys. Chem. A. 113 (2009) 6462.

[35] Ch.M. Choi, J.H. Lee, Y.H. Choi, H.J. Kim, N.J. Kimm J. Heo. J. Phys. Chem. A. 114 (2010) 11167.

[36] T.E. Cooper, D.R. Carl, J. Oomens, J.D. Steill, P.B. Armentrout. J. Phys. Chem. A. 115 (2011) 5408.

[37] E.D. Glendening, D. Feller. J. Am. Chem. Soc. 118 (1996) 6052.

[38] M.D. Paulsen, B.P. Hay. J. Mol. Struct. (Theochem) 429 (1998) 49.

[39] B. Valeur, I. Leray. Coord. Chem. Rev. 205 (2000) 3.

[40] R. Velu, V.T. Ramakrishnan, P. Ramamurthy. Tetrahedron Lett. 51 (2010) 4331.

[41] R. Kusaka, Y. Inokuchi, S.S. Xantheas SS, E. Takayuki. Sensors 10 (2010) 3519.

[42] J.J. Valle, J.R. Eyler, J. Oomens, D.T. Moore, A.F.G. van der Meer, G. von Helden, G. Meijer, C.L. Hendrickson, A.G. Marshall, G.T. Blakney. Rev. Sci. Instrum. 76 (2005) 023103 1.

[43] D. Oepts, A.F.G. van der Meer, P.W. van Amersfoort. Infrared Phys. Technol. 36 (1995) 297.

[44] http://www.rijnhuizen.nl/felix

[45] N.C. Polfer, J. Oomens. Phys. Chem. Chem. Phys. 9 (2007) 3804.

[46] N.C. Polfer, J. Oomens. Mass Spectrom. Rev. 28 (2009) 468.

[47] A.K. Rappé, C.J. Casewit, K.S. Colwell, W.A. Goddard III, W.M. Skiff. J. Am. Chem. Soc. 114 (1992) 10024.

[48] A.D. Becke. J. Chem. Phys. 98 (1993) 5648.

[49] D. Andrae, U. Häu„ermann, M. Dolg, H. Stoll, H. Preu„. Theor. Chim. Acta. 77 (1990) 123.

[50] S.F. Boys, F. Bernardi. Mol. Phys. 19 (1970) 553.

[51] Gaussian 09, Revision A.1, M.J. Frisch, G.W. Trucks, H.B. Schlegel, G.E. Scuseria, M.A. Robb, J.R. Cheeseman, G. Scalmani, V. Barone, B. Mennucci, G.A. Petersson, H. Nakatsuji, M. Caricato, X. Li, H. P. Hratchian, A.F. Izmaylov, J. Bloino, G. Zheng, J.L. Sonnenberg, M. Hada, M. Ehara, K. Toyota, R. Fukuda, J. Hasegawa, M. Ishida, T. Nakajima, Y. Honda, O. Kitao, H. Nakai, T. Vreven, J.A. Montgomery, Jr., J.E. Peralta, F. Ogliaro, M. Bearpark, J.J. Heyd, E. Brothers, K.N. Kudin, V.N. Staroverov, R. Kobayashi, J. Normand, K. Raghavachari, A. Rendell, J.C. Burant, S.S. Iyengar, J. Tomasi, M. Cossi, N. Rega, J.M. Millam, M. Klene, J.E. Knox, J. B. Cross, V. Bakken, C. Adamo, J. Jaramillo, R. Gomperts, R.E. Stratmann, O. Yazyev, A.J. Austin, R. Cammi, C. Pomelli, J.W. Ochterski, R.L. Martin, K. Morokuma, V.G. Zakrzewski, G.A. Voth, P. Salvador, J.J. Dannenberg, S. Dapprich, A.D. Daniels, Ö. Farkas, J.B. Foresman, J.V. Ortiz, J. Cioslowski, D.J. Fox, Gaussian, Inc., Wallingford CT, 2009.

[52] S.Z. Fairchild, C.F. Bradshaw, W. Su, S.K. Guharay, S.K. Appl. Spectrosc. 63 (2009) 733.

[53] V.V. Yakshin, O.M. Vilkova, S.A. Kotlyar, R.Ya. Grigorash. Phys. Chem. 379 (2001) 176.

[54] E.D. Glendening, D. Feller. J. Phys. Chem. 100 (1996) 4790.

[55] J. Srinivasa Rao, T.C. Dinadayalane, J. Leszczynski, G. Narahari Sastry. J. Phys. Chem. A. 112 (2008) 12944.

[56] T. Wyttenbach, G. von Helden, M.T. Bowers. Int. J. Mass Spectrom. Ion Proc. 165/166 (1997) 377.

[57] J.B. Nicoll, D.V. Dearden. Int. J. Mass Spectrom. 204 (2001) 171.

Chapter 9

Tweezer–like complexes of crown ethers with divalent metals: probing cation–size dependent conformations by vibrational spectroscopy in the gas phase

Crown ethers constitute central building blocks for the synthesis of molecular tweezers capable of trapping cationic species. In this study, isolated ternary complexes comprising two 18–crown–6 (18c6) ether molecules and one divalent cation of varying size (Cu^{2+}, Ca^{2+}, Ba^{2+}) are investigated by means of laser vibrational action spectroscopy and computations. In the ternary $(18c6)_2$–Cu^{2+} complex, one of the crown units folds tightly around the cation, while the second crown ether binds peripherally. Such asymmetrical binding manifests itself as a bimodal splitting of the vibrational bands measured for the complex. The size of the cation in the Ca^{2+} and Ba^{2+} complexes leads to a progressively more symmetrical coordination of the two crown ether molecules with the metal. In particular, in the spectrum of the $(18c6)_2$–Ba^{2+} complex, the two components of the vibrational bands are merged into single–maximum envelopes. This is consistent with a C_2 arrangement predicted by the computation, in which the cation coordinates with the two crown ethers in a fully symmetrical way.

9.1 Introduction

Molecular pincers or "tweezers" were introduced about three decades ago as synthetic molecular structures capable of trapping specific guest molecules, and nowadays play a key role in the development of novel supramolecular and nanotechnological materials [1, 3, 4, 2, 5, 6, 7]. Particular efforts have been devoted to the design of dynamical architectures providing molecular recognition and a clipping action that may be reversibly modulated by photon absorption or chemical additives [3, 4, 5, 6, 7].

Crown ethers bind with remarkable selectivity monovalent and divalent metal cations, as well as molecular cations such as ammonium and protonated amines [8, 9, 10]. An important class of molecular pincers and related supramolecular assemblies is based on crown ether building blocks [3, 11, 12, 13, 14, 15, 16, 17, 18, 19, 20, 21]. The fundamental understanding of such complex structures demands for benchmark systems that capture the main driving forces of pincer action within a simplified molecular framework. The core of pincer activity can be considered to rely on the interaction of the guest species with the two capping molecular moieties that act as selective binders. Such interaction can be investigated in detail in isolated ternary complexes resembling the chemical and conformational features of the actual pincer molecule while being sufficiently small to be accessible to both experimental and computational techniques. The potential of this approach has been demonstrated in different gas phase investigations of binary crown–cation complexes [21, 22, 23, 24, 25] and of ternary tweezer–like complexes formed between one metal cation and two capping crown ethers [21, 18, 19, 20]. Those investigations have probed relevant conformational and energetic aspects that control the stability and selectivity of the complexes. Specifically, the flexibility and orientational freedom of the crown ether units was shown to aid in providing an optimum balance between the crown–cation attractive forces and the mutual repulsive forces exerted by the crown ether backbones. Nevertheless, efforts devoted to characterize isolated ternary cationic complexes of crown ethers are scarce in comparison to their binary counterparts.

The ternary complexes formed between a pair of crown ethers and a cation are actually relevant by themselves for both fundamental and practical reasons. It has been shown that these complexes tend to dominate the thermodynamic equilibrium in diluted cation/crown ether solutions, at least for a range of guest–host pairs [26]. In addition, the ternary complexes display an enhancement of the selectivity of the complexation with respect to the crown–cation binary system [12].

In this study, we aim at providing novel insights into the conformational properties of the tweezer–like complexes formed by the common native 18–crown–6 crown ether with divalent metal cations (Cu^{2+}, Ca^{2+}, Ba^{2+}). The investigation employs laser–induced vibrational action spectroscopy of the cationic complexes isolated in an ion trap at room temperature. Density Functional Theory quantum computations are carried out in order to assign the recorded spectra to molecular conformations of the complexes. In addition to inspecting specific aspects of the individual complexes, we address the issue of the constraints imposed by the relative size of the cation and the crown ether ring in determining the conformation and stability of the ternary system. The results are expected to aid in the design of optimal molecular tweezer architectures based on crown ethers for specific cation binding.

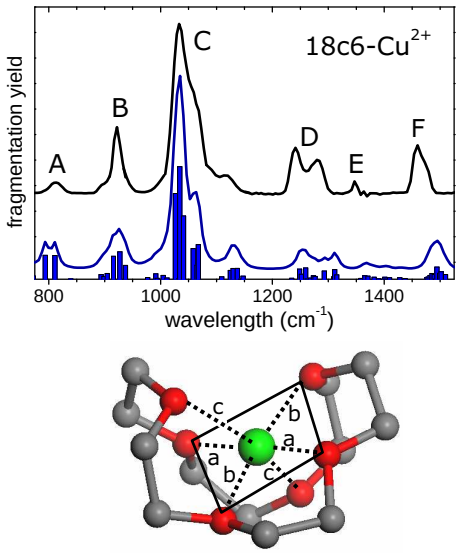

Figure 9.1: Top panel: experimental IRMPD spectrum (upper trace) of the 18c6–Cu^{2+} binary complex, and corresponding computational B3LYP/6-311++G(2d,2p) IR spectrum (lower trace), obtained from the convolution of the transitions represented by the histograms with a broadening of 15 cm^{-1}. The vibrational bands are labelled A–F for discussion and the associated vibrational modes are indicated in the text. Bottom panel: Representation of the lowest energy B3LYP conformer indicating the approximately square-planar coordination network built by the crown ether backbone around the cation.

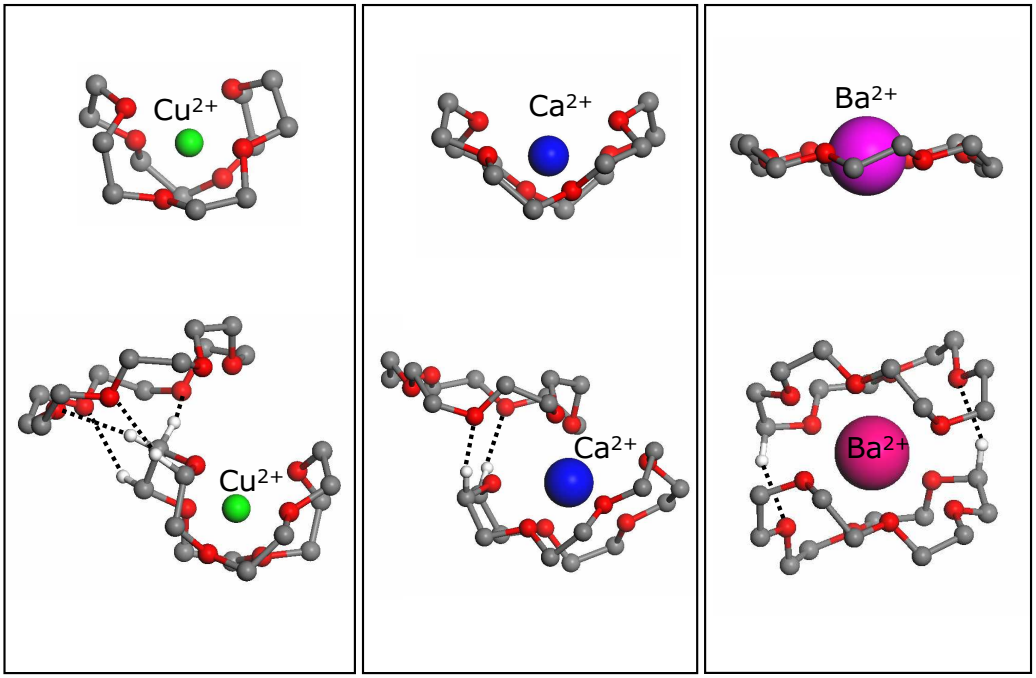

Figure 9.4: Representation of the computational lowest energy conformers of the 18c6–M^{2+} binary (B3LYP/6-311++G(2d,2p)) and $(18c6)_2$–M^{2+} ternary (B3LYP/6-311++G(d,p)) complexes (M= Cu, Ca, Ba) associated with the IR spectra shown in Figs. 9.1 and 9.3. The hydrogen atoms of the crown ether backbone have been removed for clarity, except those involved in CH$\cdots$O bonds (indicated with dashed lines) between the two ether rings in the ternary systems. The 18c6–Ca^{2+} and 18c6–Ba^{2+} conformers are from ref. [23].

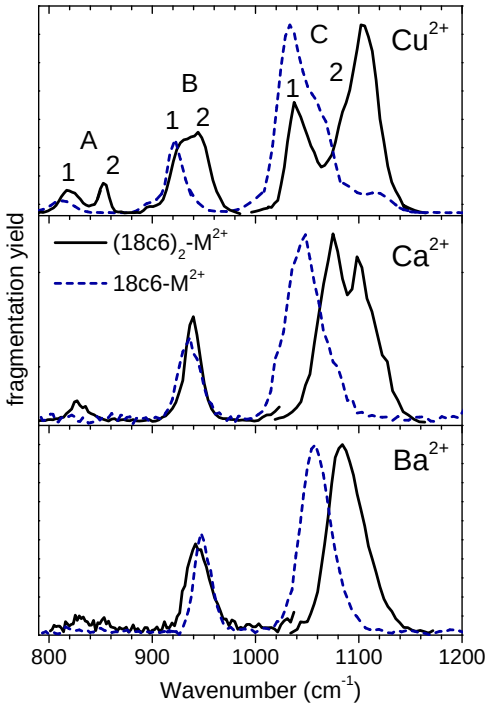

Figure 9.2: Comparison of the experimental IRMPD spectra of the $(18c6)_2$–M^{2+} ternary complexes (solid line traces, M= Cu, Ca, Ba) with the corresponding 18c6–M^{2+} binary complexes (dashed line traces). The 18c6–Ca^{2+} and 18c6–Ba^{2+} spectra are from ref. [23]. See text for a description of the vibrational modes associated with the bands labelled A–C. In the $(18c6)_2$–Cu^{2+} ternary complex, each band is split into two components (denoted '1' and '2'), one of which roughly coincides with the bands of the 18c6–Cu^{2+} binary complex. The two components merge into a single band as the size of the cation increases in the Ca^{2+} and Ba^{2+} complexes. This is indicative of a transition from a marked asymmetry in the binding strength of the two crown ether molecules with the cation for $(18c6)_2$–Cu^{2+} to an even sharing of the coordination for $(18c6)_2$–Ba^{2+}, with the $(18c6)_2$–Ca^{2+} complex being an intermediate case (see text and Fig. 10.5).

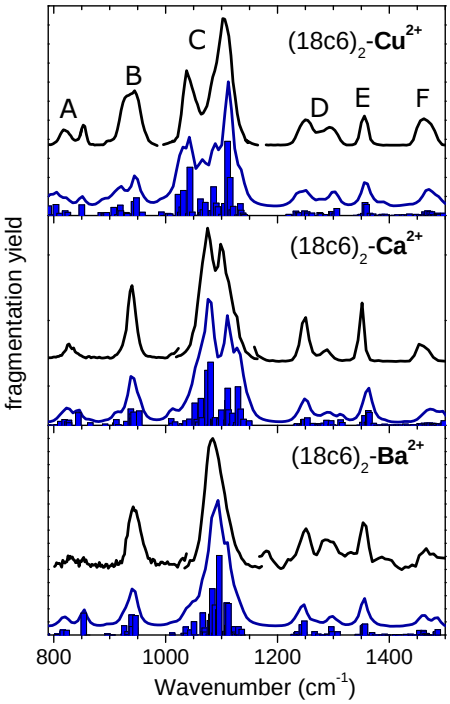

Figure 9.3: Full representation of the experimental IRMPD spectra registered for the $(18c6)_2$–M^{2+} (M= Cu, Ca, Ba) ternary complexes (upper trace in each panel), and comparison with the respective computational B3LYP/6-311++G(d,p) IR spectra (lower race in each panel). The vibrational bands are labelled A–F for discussion and the associated vibrational modes are indicated in the text. The intense C–O stretching band C was measured independently with attenuated laser power in order to avoid saturation effects. The B3LYP spectra are obtained from the convolution of the transitions represented by the histograms with a broadening of $15\,cm^{-1}$. The lowest energy B3LYP conformers associated with the spectra are represented in Fig. 10.5.

9.2 Methods

9.2.1 ESI-FTICR IRMPD spectroscopy

Infrared multiple photon dissociation (IRMPD) spectra were recorded using a Fourier-Transform Ion Cyclotron Resonance (FT–ICR) mass spectrometer coupled to the free electron laser FELIX [27]. The binary 18c6-Cu^{2+} and ternary $(18c6)_2$–M^{2+} (M= Cu, Ca, Ba) crown–metal complexes were produced at room temperature via electrospray of 1 mM solutions of the crown ether and a metal salt ($CuCl_2$, $CaCl_2$, $BaCl_2$) in a water/methanol mixture. Ions are accumulated in a hexapole trap and then pulse injected into the ICR cell for isolation of the parent mass and subsequent irradiation with typically 10 FELIX macro–pulses. Each macro–pulse is approximately 5 μs long, has an energy of about 35 mJ, and consists of a train of micro–pulses with a repetition frequency of 1 GHz. The nominal spectral bandwidth of the radiation amounts to 0.5% of the central wavelength. Further description of typical experimental procedures can be found in ref. [28].

If the infrared wavelength is in resonance with a vibrational mode of the complex, multiple photon absorption occurs leading to dissociation of the parent ion. The IRMPD spectrum is constructed by plotting the relative ionic fragment yield as a function of the wavenumber of the radiation. For the binary 18c6-Cu^{2+} complex, two dominant fragmentation channels were observed, namely those associated with the cleavage of one or two OC_2H_4 ether monomers from the crown ring. In all ternary complexes, a single dominant fragment was detected which corresponded to the loss of one of 18c6 molecules, hence leading to the binary complex 18c6–M^{2+}. The recorded fragment ion signals were linearly corrected for the changes in laser pulse power [28]. The intense C–O stretching band (at about 1000–1200 cm^{-1}) was repeatedly probed with attenuated laser power in order to avoid saturation due to depletion of complexes in the laser beam path.

9.2.2 Quantum Chemistry calculations

Simulated annealing with the Universal force field was employed to generate an ensemble of molecular structures. For the ternary complexes, the procedure was initiated from arrangements generated *ad hoc* by incorporating a second 18c6 unit to the 18c6–M^{2+} binary structures determined here for Cu^{2+} and in a previous similar investigation for Ca^{2+} and Ba^{2+}.[23] The conformations of lowest energy resulting from the simulated annealing were optimized with Density Functional Theory at the B3LYP/6-31G(d,p) level. Finally, the overall most stable conformers were reoptimized with the larger basis set 6-311++G(d,p). For the 18c6–Cu^{2+} binary system the basis set was also extended to 6-311++G(2d,2p) for a better comparison with the previous studies on the analogous alkaline–earth complexes.[23] All energies reported here for the conformers are Gibbs free energies including vibrational zero–point corrections. The non–valence electrons of Ba^{2+} were treated with the Stuttgart/Dresden effective core potential [29]. For the Cu^{2+} complexes, only the doublet ground electronic state of the cation was considered. Spin promotion due to the ligand field, inducing the stabilization of spin states of higher multiplicity, was observed for lighter third row transition metal cations (*e.g.* Cr^+) [**?**]. A similar effect is not expected for the d^9 electronic configuration of Cu^{2+}. The calculations were carried out with the Gaussian 09 code.[31]

The theoretical harmonic IR spectra shown in this work were calculated by convoluting the B3LYP lines with a lorentzian broadening of 15 cm^{-1} (full width at half maximum). The computed vibrational frequencies for all the complexes were scaled for comparison with experiment by a factor 0.982. This factor is in agreement with the scaling derived in previous studies for the level of theory presently employed [32].

9.3 Results

9.3.1 Cu^{2+} complexes

The starting point of this investigation was the characterization of the binary and ternary complexes formed by the 18c6 crown ether with the Cu^{2+} cation. On the one hand, we intended to determine what kind of coordination arrangement would this open shell divalent cation build with the oxygens of the 18c6 ether ring. Furthermore, we were interested in describing how that coordination changes when a second ether molecule binds to the complex to form the $(18c6)_2$–Cu^{2+} ternary complex.

We focus first on the results for the 18c6–Cu^{2+} complex. Fig. 9.1 shows the IRMPD spectrum recorded for this system together with the computed IR spectrum corresponding to the lowest energy conformer predicted by the B3LYP/6-311++G(2d,2p) method. For the sake of discussion, the vibrational bands are labelled A through F in order of increasing wavenumber. The dominant types of nuclear motions of the vibrational modes associated with these bands are as follows: Band A is due to COC bending coupled with CH_2 torsion vibrations, bands B and C correspond to the C–C and C–O stretching modes, respectively, and bands D, E and F are related to CH_2 torsions, wagging and scissoring motions, respectively. It can be observed that the B3LYP

spectrum reproduces quite accurately the experimental IRMPD spectrum, except for a slight shift of the bands of higher frequency associated with the CH_2 vibrations (bands D, E and F).

The lower panel of Fig. 9.1 depicts the molecular structure of the B3LYP lowest energy 18c6–Cu^{2+} conformer and sketches the six-fold coordination of the cation involving all the oxygens of the ring. It can be seen that such coordination arrangement demands that the 18c6 ring folds tightly around the cation. Such conformation is qualitatively similar to that displayed by the analogous complex of 18c6 with Mg^{2+},[23] a cation with an ionic radius similar to Cu^{2+} (*ca.* 0.7 Å). However, whereas the lowest energy conformation of the 18c6–Mg^{2+} complex was found to be of D_2 symmetry,[23] for 18c6–Cu^{2+} it is of C_1 symmetry, with the D_2 conformation lying higher in energy by about 2 kJ mol^{-1} at the B3LYP/6-311++G(2d,2p) level of theory.

Such loss of symmetry appears to be related to the tendency of Cu^{2+} to build a roughly square-planar coordination with four oxygens of the ring, and a somewhat looser coordination with the other two oxygens in normal directions. With the notation indicated in Fig. 9.1, in the most stable C_1 conformer the bond lengths take values $a \approx b \approx 2.0$ Å, $c = 2.3$ Å. In the higher lying D_2 conformer (not shown but visually similar), the bonds a and b are coplanar as in the C_1 conformer but the bond lengths are $a = 2.0$ Å, $b = c = 2.2$ Å (hence, the bonds of equal length are not coplanar). In any case, the difference in energy between the C_1 and D_2 conformations is small and within the typical accuracy of the B3LYP computations, so that a contribution from both conformers in the present room temperature experiments can be expected. Our measurements cannot confirm nor rule out this possibility as the two structures are conformationally close and display similar IR spectra within the resolution of the present experiments.

Irrespective of the precise symmetry (C_1 or D_2) of the 18c6–Cu^{2+} system, the folded cage–like arrangement of the crown ring around the cation makes the stability and structure of the $(18c6)_2$–Cu^{2+} ternary complex uncertain. It is *a priori* not clear to what extent the incorporation of the second ether unit would be able to disrupt the tight coordination of the cation with the first 18c6 molecule. The IRMPD spectrum measured for the $(18c6)_2$–Cu^{2+} complex is shown in the top panel of Fig. 9.2 together with the IRMPD spectrum of the 18c6–Cu^{2+} binary complex. It can be appreciated that the vibrational bands of the ternary complex are split into two components with maxima at about 820 and 850 cm^{-1} for band A, 930 and 950 cm^{-1} for band B (unresolved) and 1040 and 1100 cm^{-1} for band C. It is also noticeable that the IRMPD spectrum of the binary complex overlaps closely with the component of lower frequency within each of the bands. An intuitive interpretation of this finding readily emerges: in the $(18c6)_2$–Cu^{2+} complex one of the crown ethers is coordinated tightly with the cation in a similar way as in the binary complex, while the second 18c6 molecule binds more peripherally to the 18c6–Cu^{2+} moiety. That second, weakly bound 18c6 molecule would then be responsible for the blue-shifted component of the bands (denoted '2' in Fig. 9.2). Such an interpretation is in fact supported by the present computations.

The IRMPD spectrum of the $(18c6)_2$–Cu^{2+} complex is shown in its full extent in the top panel of Fig. 9.3, where it is compared with the IR spectrum of the most stable conformer predicted by the B3LYP/6-311++G(d,p) computation. The agreement between the B3LYP and the experimental spectra is remarkable. Fig. 10.5 represents the molecular structure of the B3LYP conformer which is indeed characterized by the asymmetrical binding of the two crown ethers with the cation as anticipated above. The inspection of the vibrational motions associated with each of the normal modes predicted by the computation corroborates the assignment of the two band components in the IR spectrum to the two differentiated 18c6 units of the complex. It can be noted that the peripheral "spectator" 18c6 molecule is bound due to an ensemble of short range (2.2–2.4 Å) CH$\cdots$O H–bonding intermolecular interactions, in addition to the longer range (4–6 Å) charge–dipole interactions of the oxygens with the Cu^{2+} cation.

It is of interest to mention that it was fairly straightforward to produce and store the $(18c6)_2$–Cu^{2+} ternary complex in the ICR trap. In contrast, no trace of the $(18c6)_2$–Cu^{+} complex could be found when the same experiment was performed with the monovalent Cu^{+} cation (with CuCl as precursor). The binding energy of the "spectator" 18c6 molecule appears to be significantly reduced for the singly charged cations, so that the complex is unstable under the present operating conditions of the ion source and the preconcentration hexapole trap. This observation suggests that charge–dipole interactions should be key for the stability of this type of asymmetric ternary complex.

9.3.2 Ternary complexes of Ca^{2+} and Ba^{2+}

The second stage of the study was devoted to the evolution of the $(18c6)_2$–M^{2+} most stable conformation for progressively larger guest divalent cations. For this purpose, we considered as reference our previous study on the binary complexes formed by 18c6 with the cations of the alkaline–earth series.[23] The cations Ca^{2+} and Ba^{2+} (ionic radii of 1.00 and 1.35 Å, respectively) seemed appropriate choices to work out the transition from a folded conformation to a fully open one in the 18c6–M^{2+} binary

system. Fig. 10.5 shows that indeed the 18c6–Ca^{2+} complex displays a partly folded structure, while the 18c6–Ba^{2+} complex is fully open and quasi-planar. In this study, we explore how the structure of the corresponding ternary complexes evolves with cation size.

The IRMPD spectra recorded for the $(18c6)_2$–Ca^{2+} and $(18c6)_2$–Ba^{2+} complexes are shown in Figs. 9.2 and 9.3 in similar representations as the ones described above for the Cu^{2+} complex. One of the most obvious changes in the spectra as the cation becomes larger is the merging of the two components of the vibrational bands. This is particularly apparent for the C-O stretching band (1000–1200 cm^{-1}), dominant in the IRMPD spectra. The splitting between the two components of this band is only of about 25 cm^{-1} for the Ca^{2+} complex (*i.e.*, more than a factor of 2 smaller than in the case of Cu^{2+}), while both components are merged into a relatively narrow single–maximum envelope for the Ba^{2+} complex. This trend is indicative of a progressively more symmetric participation of the two 18c6 molecules in the binding of the cation. The agreement with the B3LYP IR spectra is again very good.

Fig. 9.2 also shows that the C–O stretching bands of the ternary complexes of Ca^{2+} and Ba^{2+} are appreciably blue–shifted with respect to the corresponding bands of the binary complexes. This finding can be attributed to an overall weakening of the interactions of each of the ether oxygens with the cations due to the sharing of the coordination between the two 18c6 molecules. Such a shift was not observed when comparing the spectra of the binary and ternary complexes of Cu^{2+} since in that case one of the 18c6 molecules essentially retains the same coordination arrangement with the cation in the two types of complexes. Note that the C–C stretching band does not shift from the binary to the ternary complex as it is not so directly affected by the coordination of the oxygens with the cation [23].

The most stable B3LYP conformations for the $(18c6)_2$–Ca^{2+} and $(18c6)_2$–Ba^{2+} complexes, depicted in Fig.10.5, are consistent with the above considerations. In the ternary Ca^{2+} complex, the participation of the two 18c6 molecules is still uneven but the cation interacts directly with oxygens of the two ether molecules. One 18c6 embraces the cation in a somewhat more open conformation than in the binary complex, while the second 18c6 molecule places two oxygens in tight coordination with the cation. In this way, the Ca^{2+} coordinates with eight ether oxygens in a remarkable uniform way, at distances within 2.5–2.6 Å (in the binary complex all six cation–oxygen distances are of 2.4 Å [23]). It can also be noted that this ternary complex is sustained in addition by two weak CH$\cdots$O intermolecular H bonds (2.2 Å bond distance) between the two ether backbones.

The $(18c6)_2$–Ba^{2+} complex stabilizes in a remarkable symmetric C_2 arrangement in which the interaction with the cation is evenly balanced between the two 18c6 molecules. The partly folded conformation displayed by the two crown ethers is in marked contrast with the quasi–planar D_{3d} structure of the ether ring in the binary complex (see Fig.10.5). In this way, all twelve oxygens coordinate with the Ba^{2+} cation at distances within 3.0–3.3 Å (*versus* 2.8 Å in the binary complex). Two CH$\cdots$O weak intermolecular H bonds are also formed between the crown ethers in this complex with bond distances of about 2.4 Å.

It is interesting to note that the coordination of the Ca^{2+} and Ba^{2+} cations with eight and twelve ether oxygens, respectively, in the ternary complexes is in line with previous hydration studies for the 18c6 complexes of these two cations. [26] Hydration numbers of two and six were determined for the 18c6–Ca^{2+} and 18c6–Ba^{2+} complexes, respectively. It turns out that the number of water molecules that each of the binary complexes can accommodate is coincident with the number of oxygens from a second ether that it can bind tightly.

9.4 Conclusions

Infrared multiple photon dissociation vibrational spectroscopy in combination with quantum–chemical computations have been employed to provide insights into the conformational features of tweezer–like prototypes involving the 18–crown–6 ring molecule. The ternary complexes comprised by two 18–crown–6 molecules and one of the divalent metal cations Cu^{2+}, Ca^{2+} or Ba^{2+} have been considered as benchmark systems in order to explore the dependence of the resulting structures on cation size.

The Cu^{2+} cation induces a tightly folded arrangement of the crown ether backbone in the binary 18c6–Cu^{2+} complex, in a qualitatively similar way as found previously for the 18c6–Mg^{2+} complex [23]. As a consequence, the ternary $(18c6)_2$–Cu^{2+} complex displays a markedly asymmetric conformation for the two ether units. Whereas one 18c6 molecule coordinates with the cation in a folded conformation similar to that of the binary complex, the second 18c6 molecule binds peripherally through longer range electrostatic interactions with the cation and CH$\cdots$O intermolecular bonds with the first 18c6 ring. This behavior leads to a pronounced splitting in some of the main vibrational bands of the complex into two components, namely a red–shifted component for the strongly bound crown ether backbone and a blue–shifted one associated with the more weakly bound 'spectator' crown ether.

As the size of the cation becomes larger, represented here by the Ca^{2+} and Ba^{2+} complexes, the participation of the two 18c6 molecules becomes progressively more even. In the $(18c6)_2$–Ca^{2+} complex, one of the crown ethers still retains a resemblance of the coordination found in the 18c6–Ca^{2+} binary complex. Nevertheless, the cation manages to coordinate tightly with two of the oxygens of the second 18c6 molecule, for a total cation–oxygen coordination number of eight. For the $(18c6)_2$–Ba^{2+} complex, the appreciable size of the cation favors a symmetric coordination of the two ethers with the cation in a C_2 conformation in which all 12 ether oxygens are involved. In accord with these trends, the experimental IRMPD spectrum shows a moderate splitting of the vibrational bands for $(18c6)_2$–Ca^{2+} complex, while the two components are fully merged into single bands for the $(18c6)_2$–Ba^{2+} complex.

The present study has shown that the conformation adopted by the crown ethers in ternary $(18c6)_2$–M^{2+} complexes depends dramatically on the relative sizes of the ether ring and the cation. This general result indicates that the flexibility of the crown ether moiety in a molecular pincer should play a key role in the type of binding that it will achieve with a given cationic species. If the crown ethers have sufficient conformational freedom in the pincer architecture, the simultaneous participation of the two pincer arms will only be efficient for large cations while small cations will tend to coordinate with only one of the crown ether arms. The good agreement found between the experiments and the computations in this study indicate that the relatively inexpensive Density Functional Theory can be employed to draw predictions in this field.

Bibliography

[1] C.-W. Chen, H.W. Whitlock. J. Am. Chem. Soc. 100 (1978) 4921.

[2] a) S.C. Zimmerman, C.M VanZyl, J. Am. Chem. Soc. 109 (1987) 7894; b) S.C. Zimmerman, Top. Curr. Chem. 165 (1993) 71.

[3] S. Shinkai, T. Nakaji, T. Ogawa, K. Shigematsu, O. Manabe. J. Am. Chem. Soc. 103 (1981) 111.

[4] M. Irie, M. Kato. J. Am. Chem. Soc. 107 (1985) 1024.

[5] F.G. Klärner, B. Kahlert. Acc. Chem. Res.36 .(2003) 919.

[6] A. Petitjean, R.G. Khoury, N. Kyritsakas, J.M. Lehn, J. Am. Chem. Soc. 126 (2004) 6637.

[7] J. Leblond, A. Petitjean. CHEMPHYSCHEM 12 (2011) 1043.

[8] C.J. Pedersen. Science, 241 (1988) 536.

[9] J.S. Bradshaw, R.M. Izatt, Acc. Chem. Res. 10(1997) 338.

[10] G.W. Gokel, M. Leevy, M.E. Weber, Chem. Rev.104 (2004) 2723.

[11] M. Takeshita, M. Irie. J. Org. Chem. 63 (1998) 6643.

[12] S. Fery–Forgues, F. Al–Ali. J. Photochem. Photobiol. C: Photochem. Rev. 5 (2004) 139.

[13] a) A.I. Vedernikov, E.N. Ushakov, N.A. Lobova, A.A. Kiselev, M.V. Alfimov, S.P. Gromova, Russian Chem. Bull. 54 (2005) 666; b) S.Y. Zaitsev, E.N. Zarudnaya, D. Mobius, V.V. Bondarenko, V.I. Maksimov, I.S. Zaitsev, E.N. Ushakov, N.A. Lobova, A.I. Vedernikov, S.P. Gromov, M.V. Alfimov, Mendeleev Comm. 18 (2008) 270; c) S.P. Gromov, A.I. Vedernikov, L.G. Kuz'mina, N.A. Lobova, S.S. Basok, Y.A. Strelenko, M.V. Alfimov. Russian Chem. Bull. 58 (2009) 108.

[14] A.M.M. Abe, J. Helaja, A.M.P. Koskinen. Org. Lett. 8 (2006) 4537.

[15] H. Shimakoshi, K. Shibata, Y. Hisaeda. Inorg. Chem. 48 (2009) 1045.

[16] H. Shimakoshi, D. Maeda, Y. Hisaeda. Supramol. Chem. 23 (2011) 131.

[17] P.R. Ashton, E.J.T. Chrystal, P.T. Glink, S. Menzer, C. Schiavo, N. Spencer, J.F. Stoddart, P.A. Tasker, A.J.P. White, D.J. Williams. Chem. Eur. J. 2 (1996) 709.

[18] T. Wyttenbach, G. von Helden, M.T. Bowers. J. Mass. Spectrom. Ion Processes. 377 (1997) 165.

[19] N. Shen, R.M. Pope, D.V. Dearden. Int. J. Mass Spectrom. 195-196 (2000) 639.

[20] J.B. Nicoll, D.V. Dearden. Int. J. Mass Spectrom. 204 (2001) 171.

[21] B. Martínez–Haya, P. Hurtado, A.R. Hortal, J.D. Steill, J. Oomens, P.J. Merkling. J. Phys. Chem. A. 113 (2009) 7748.

[22] a) B. Martínez–Haya, P. Hurtado, A.R. Hortal, S. Hamad, J.D. Steill, J. Oomens. J. Phys. Chem. A. 114 (2010) 7048; b) P. Hurtado, A.R. Hortal, F. Gámez, S. Hamad, B. Martínez–Haya. Phys. Chem. Chem. Phys. 12 (2010) 13752; c) P. Hurtado, F. Gámez, S. Hamad, B. Martínez–Haya, J.D. Steill, J. Oomens. J. Phys. Chem. A. 115 (2011) 7275.

[23] F. Gámez, P. Hurtado, B. Martínez–Haya, G. Berden, J. Oomens. Int. J. Mass Spectrom. 308 (2011) 217.

[24] a) J.D. Rodriguez, J.M. Lisy. Int. J. Mass Spectrom. 283 (2009) 135; b) J.D. Rodriguez, J.M, Lisy. J. Am. Chem. Soc. 133 (2011) 11136.

[25] Y. Inokuchi, O.V. Boyarkin, R. Kusaka, T. Haino, T. Ebata, T.R. Rizzo. J. Am. Chem. Soc. 133 (2011) 12256.

[26] H. H∅yland, J.A. Ringseth, T.S. Brun. J. Sol. Chem. 8 (1979) 779.

[27] http://www.rijnh.nl/felix

[28] a) N.C. Polfer, J. Oomens. Phys. Chem. Chem. Phys. 9 (2007) 3804; b) N.C. Polfer, J. Oomens. Mass Spectrom. Rev. 128 (2009) 468.

[29] D. Andrae, U. Häu„ermann, M. Dolg, H. Stoll, H. Preu„. Theor. Chim. Acta. 77 (1990) 123.

[30] D.T. Moore, J. Oomens, J.R. Eyler, G. von Helden, G. Meijer, R.C. Dunbar. J. Am. Chem. Soc. 127 (2005) 7243.

[31] Gaussian 09, Revision A.1, M.J. Frisch, G.W. Trucks, H.B. Schlegel, G.E. Scuseria, M.A. Robb, J.R. Cheeseman, G. Scalmani, V. Barone, B. Mennucci, G.A. Petersson, H. Nakatsuji, M. Caricato, X. Li, H. P. Hratchian, A.F. Izmaylov, J. Bloino, G. Zheng, J.L. Sonnenberg, M. Hada, M. Ehara, K. Toyota, R. Fukuda, J. Hasegawa, M. Ishida, T. Nakajima, Y. Honda, O. Kitao, H. Nakai, T. Vreven, J.A. Montgomery, Jr., J.E. Peralta, F. Ogliaro, M. Bearpark, J.J. Heyd, E. Brothers, K.N. Kudin, V.N. Staroverov, R. Kobayashi, J. Normand, K. Raghavachari, A. Rendell, J.C. Burant, S.S. Iyengar, J. Tomasi, M. Cossi, N. Rega, J.M. Millam, M. Klene, J.E. Knox, J. B. Cross, V. Bakken, C. Adamo, J. Jaramillo, R. Gomperts, R.E. Stratmann, O. Yazyev, A.J. Austin, R. Cammi, C. Pomelli, J.W. Ochterski, R.L. Martin, K. Morokuma, V.G. Zakrzewski, G.A. Voth, P. Salvador, J.J. Dannenberg, S. Dapprich, A.D. Daniels, Ö. Farkas, J.B. Foresman, J.V. Ortiz, J. Cioslowski, D.J. Fox, Gaussian, Inc., Wallingford CT, 2009.

[32] S.Z. Fairchild, C.F. Bradshaw, W. Su, S.K. Guharay. App. Spectrosc. 63 (2009) 733.

Chapter 10

Gas phase investigation of α-cyclodextrine complexed with alkali metals: combined infrared, mass spectrometry and quantum chemistry calculations.

The relative binding energies and the structure of the complexes formed by α–cyclodextrin with alkali metal cations is investigated by means of MALDI and IRMPD experiments and by quantum computations. Careful solvent-free MALDI measurements lead to a trend of decreasing binding energy with increasing cation size for the gas–phase complexes. Previous studies indicating a preference for the Na^+ complex are likely to be affected by solvent effects. The IRMPD spectra of the sequence Li^+, Na^+, K^+, Cs^+ complexes are qualitatively similar and match with a metal coordination on the primary carboxylic side of the cyclodextrine cavity. This finding is consistent with the prediction of quantum computations which also shows that the inclusion of the cation converts the C_6 symmetry of the free cyclodextrin into C_3 for Li^+, C_2 for Na^+ and K^+ and C_1 for the larger alkali cations.

10.1 Introduction

Cyclodextrins (CD), known historically as cellulosines, are non–reduced sugars that were first discovered in 1891 by Villiers in the bacterial digestion of starch [1]. Their composition and cyclic structure were finally elucidated in the 1930's by means of enzymatic hydrolysis, acetolysis and hydrolysis of permethylated dextrines. Cyclodextrines are cyclic oligomers based on α-D-glucopyranosyl units connected by α-(1→4)-glycosidic linkages. Native cyclodextrines are made of six (α-CD), seven (β-CD) or eight (γ-CD) glucose units. The three-dimensional architecture of the CD macrocycle is of funnel-like geometry, with a larger (secondary) and smaller (primary) openings dressed by one -CH_2OH or -OH hydroxylic group per glucose ring, respectively. A summary of geometrical and some aqueous properties is presented in Table 10.1. The noticeable small solubility of β-cyclodextrine is due to the rigidity confered by the complete belt of H-bonds in the secondary surface of the sugar. While the rims are strongly polar, the interior of the cavity cavity is hydrophobic, and in consequence they do not include many water molecules in them. Hence, their aqueous solution complexation is favoured with hydrophobic guests and have been extensively studied and have been the basis of numerous applications [2].

The driving force in the complexation of a given CD/guest pair is the balance between the inter and intramolecular interactions, i.e. the Van der Waals steric interactions opposed to electrostatic attractions (dipole/charge and dipole-dipole, as leading contributions in this case), hydrogen bonding and solvophobic effects. The process will then be directed by the removal of water molecule from the cavity while the guest is included in the most favourable environment of the CD interior while facing steric repulsions.

From a fundamental viewpoint, the competition and importance of intramolecular interaction can be explored in detail under the conditions of molecular isolation provided by gas phase experiments. In comparison to the crown ethers considred in previous chapters, gas phase studies of cyclodextrines are much more scarce. The combined MALDI and ionic mobility measurements of cationic complexes performed by Lee et al [3] and the mass spectrometry experiments on equilibrium and stabilization of cationized CD in solution with both atomic and molecular guests as aminoacids of several groups [4, 5, 6] are among the most prominent studies found in the literature. The bibliography of theoretical studies is not much richer, probably because of the difficulties related to system size. Isolated CDs in a neutral charge state tend to build extensive hydrogen bonding networks in their primary and secondary hydroxyl groups, leading to symmetric conformations [7, 8]. The inclusion of a guest in the cavity inevitably disrupts such hydrogen bond network [9].

This work is devoted to the characterization of the gas phase complexes of α-CD with alkali cations by means of MALDI and IRMPD experimetns combined with quantum chemical calculations. Perhaps surprisingly, no conclusive investigation has been reported about the most stable conformations for these relatively simple benchmark complexes. The present investigation intends to determine the location of the guest ion within the CD substrate and the conformational features of the complexes that determine the relative affinities, as a function of the alkali metal size.

10.2 Methods

10.2.1 MALDI spectrometry and sample preparation

The MALDI experiments discussed in this chapter have been performed in an UltrafleXtreme spectrometer (Bruker) in positive ion reflectron mode with 355 nm pulses from a Nd:YAG laser. For each spectrum, 2000 shots were averaged at a 1 kHz repetition rate. Mass calibration was performed with a mixture of polar polymers (polyethylene glycol 600 and 1000). Additionally, collisional induced decay (CID) experiments has been performed in some doubly cationized complexes employing the LIFT technique coupled to the spectrometer. In these MALDI measurements, special attention was devoted to the comparison of different sample preparation methods providing information about the actual binding energies of the complexes in the gas phase. The cyclodextrin, the alkali salts and the compounds for the synthesis of the room temperature ionic liquid (RTIL) were purchased from Sigma-Aldrich and used without further purification. The following sample preparation methods and procedures were employed:

a) **Conventional dried-droplet method (DD)**: A solution of α-CD with alkali-chloride salts and 2,5-DHB matrix was prepared in methanol:water 1:1 solution. Equimolar amounts of the salts (chlorides) of the five metals Li, Na, K, Rb, Cs were employed and the CD:salt:matrix molar ratio was fixed to 1:10:1 in the solution. Finally, 1 μL of sample solution was spread on the MALDI plate for analysis.

c) **Solvent–free method (SF)**: In this case, the same molar ratios of α-CD, alkali salts and matrix were applied, although with two main fundamental differences. First, the compounds are mixed as solid fine powders, without the addition of any solvent. Second, two metals are applied in each sample employing pairs of salts with a

Table 10.1: Geometrical features of native cyclodextrines from [2].

Geometrical parameter	α-CD	β-CD	γ-CD
Number of glucopyronase units	6	7	8
Molecular weight (amu)	972	1135	1297
Solubility in water (g/100 mL at 298 K)	14.5	1.85	23.2
Water molecules in cavity	6	11	17
Inner cavity diameter (Å)	4.7-5.3	6.0-6.5	7.5-8.3
Outer cavity diameter (Å)	14.6	15.4	17.5
Cavity height (Å)	7.9	7.9	7.9
Volume of the cavity (Å^3)	174	262	427

similar lattice energy; for instance, LiI/NaBr, NaBr/KCl and KI/CsBr. In this way, similar densities of the two cations are expected to build in the desorption plume to assist the (gas-phase) complexation process.

c) **Matrices based on Room Temperature Ionic Liquids (RTIL)**: The RTIL matrix glycerol /α-CHCA /3-aminoquinoline introduced by Sze et al [10] was employed. Ratios of 1:4:6 by weight of the three components were employed. Small volumes of methanol were added and sonication (30 minutes) was applied in order to ensure the homogeneity in the matrix. Once the IL showed a consistent and homogeneous appearance, we mixed it with the cyclodextrine and the alkali chloride salts in a molar ratio 1:100. For the MALDI measurements 5 μL of RTIL solution were spread on the sample plate.

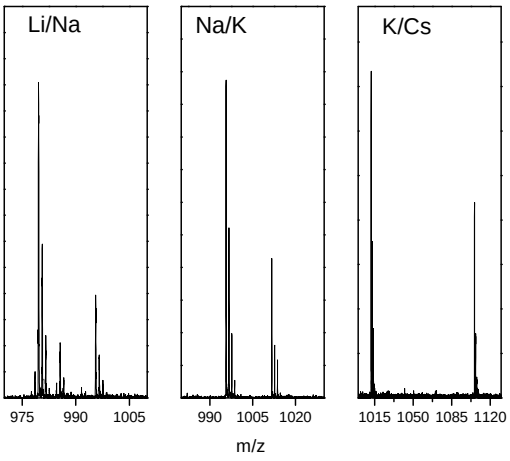

Figure 10.1: Solvent-free MALDI measurements of α-CD complexed with alkali metals

10.2.2 ESI-FTICR IRMPD spectroscopy

Infrared multiple photon dissociation (IRMPD) spectra were recorded using a Fourier-Transform Ion Cyclotron Resonance (FT–ICR) mass spectrometer coupled to the free electron laser FELIX. The α-CD–M$^+$ complexes with (M=Li, Na, K, Cs) were produced at room temperature *via* electrospray of 0.1 mM solutions of the α–cyclodextrin and chloride metal salt in a water/methanol mixture. Details of the typical experimental procedures are provide in Chapter 6 and can also be found in ref. [11]. The main IRMPD fragments observed for the complexes corresponded to the release of the cation from the CD. The fragmentation of the Li$^+$ and Na$^+$ complexes demanded a greater laser power which also led to cleavage of glycosidic bonds leading to cationized fragments lacking one or several sugar units. Since the free cations are not easily quantified in the FT-ICR spectrometer, the IRMPD spectra were recorded from the intensity of the sugar fragments for Li$^+$ and Na$^+$ and from the depletion of the precursor CD-M$^+$ ion for K$^+$ and Cs$^+$.

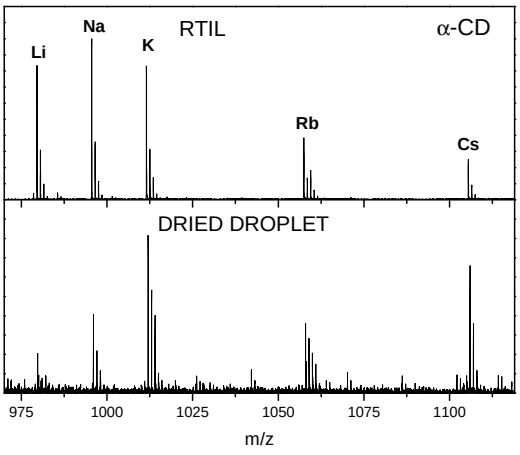

Figure 10.2: Conventional dried-droplet and RTIL MALDI measurements of α-CD complexed with alkali metals

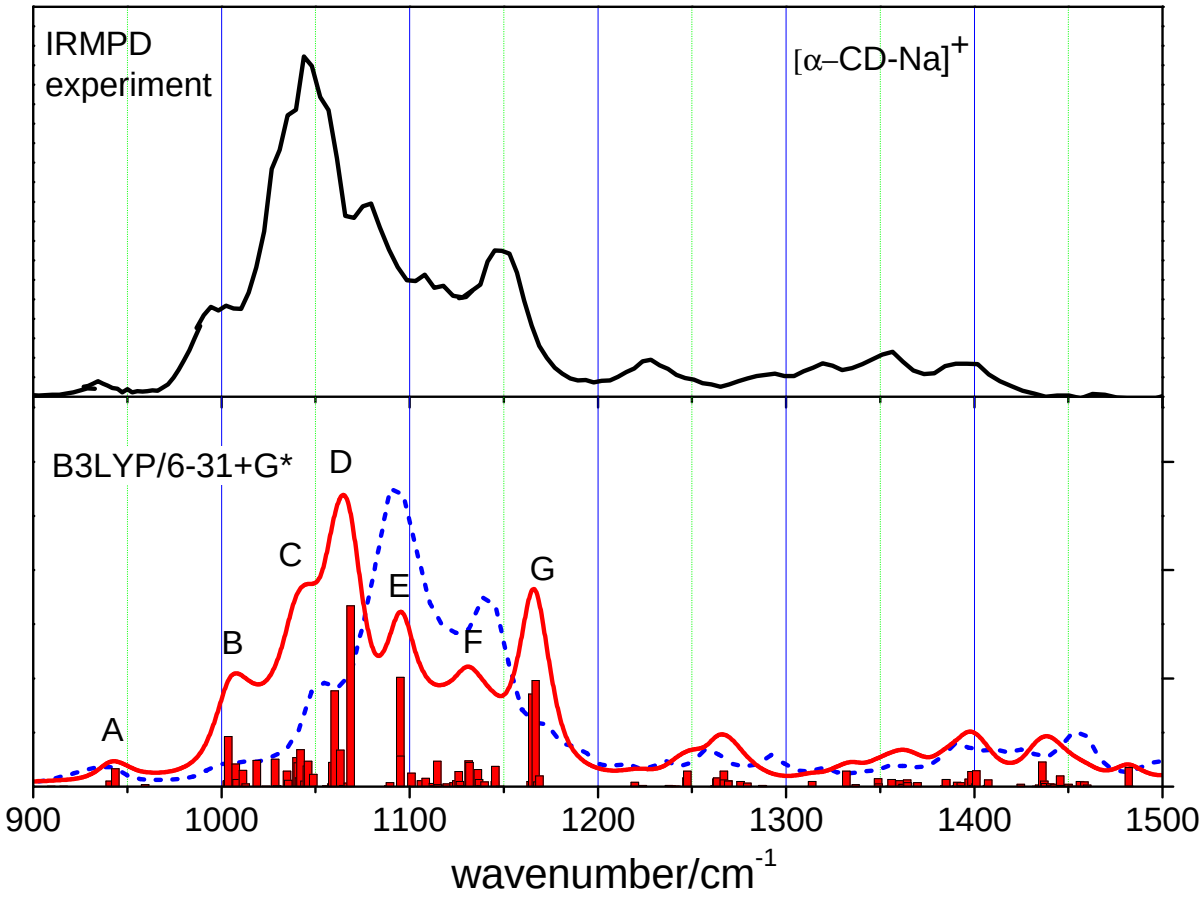

Figure 10.3: Comparison of the experimental IRMPD spectra of the sodiated CD complex with the corresponding with quantum chemical calculations. The red spectrum (plotted together with its density of states) corresponds to the inclusion of the cation in the primary side, while the blue one to the conformer with the cation located in the secondary O–H rim.

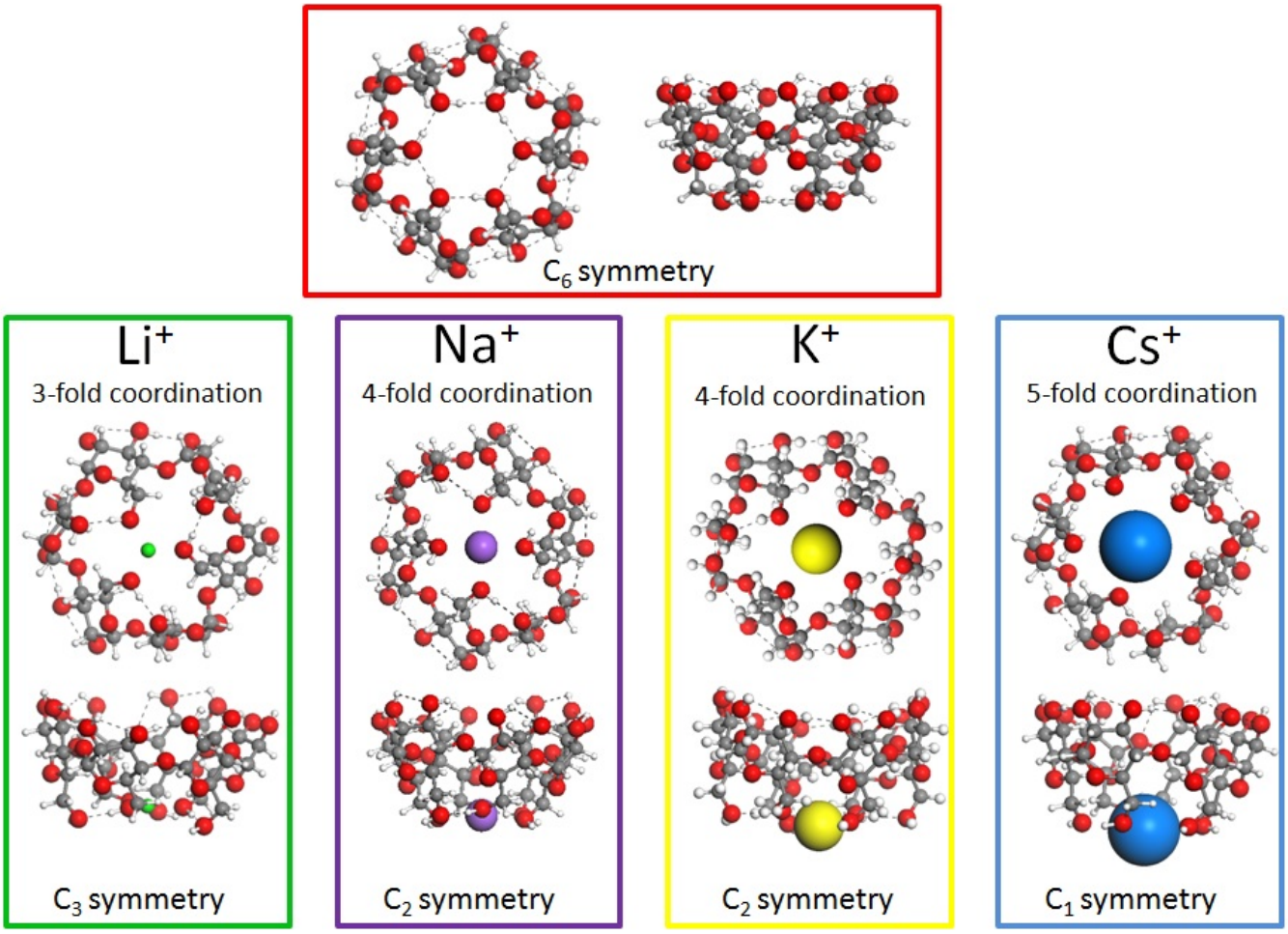

Figure 10.5: Schematic view of the lowest energy conformers of the free and alkali–CD complexes obtained with quantum chemical calculations at the B3LYP/6–31+G* level.

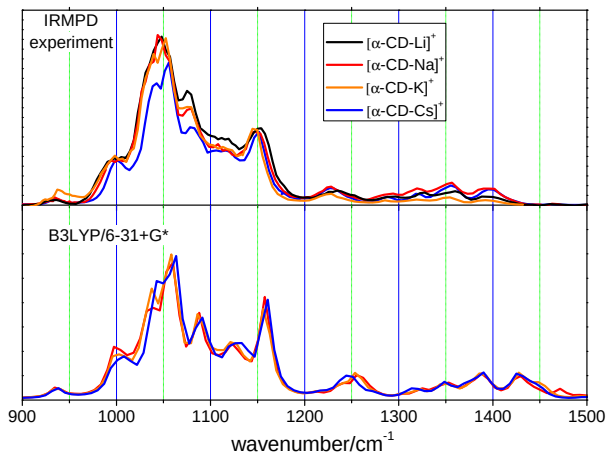

Figure 10.4: Full comparison of the experimental IRMPD spectra of the alkali–CD complexes (upper panel, M=Li, Na, K, Cs) with the corresponding with quantum chemical calculations at the B3LYP/6–31+G* level of theory (lower panel). The IRMPD spectrum of the Li complex has been extracted from the analysis due to convergence problems when employing the larger basis–set.

10.2.3 Quantum Chemistry calculations

Simulated annealing with the Universal Force Field was employed to generate an ensemble of molecular structures of the α-CD–M^+ complexes. The conformations of lowest energy resulting from the simulated annealing were optimized with Density Functional Theory at the 6-31+G* basis set. The large system size precludes the use of higher level methods with our computational resources. For the Cs^+ cation the core electrons are substituted for the Stuttgart/Dresden effective core potentials (ECP) [12]. The calculations were carried out with the Gaussian 09 code[13]. The theoretical harmonic IR spectra shown in this work were calculated by convoluting the calculated density of states with a lorentzian broadening of $15\,cm^{-1}$ (full width at half maximum). The computed vibrational frequencies for all the complexes were scaled for comparison with experiment by a factor 0.99 for comparison with experiment.

10.3 Results

10.3.1 MALDI spectrometry

The determination of gas-phase host/guest affinities with MALDI is not a trivial task. We will show that solvent effects strongly modify the relative intensities of different cyclodextrin complexes observed in MALDI spectra. Solvent free (SF) approaches in MALDI emerges as a method of key importance when dealing with gas phase affinities [14]. Under solvent-free conditions, the interaction between the cyclodextrin and the cation will take place primarily in the gas phase, after the initiation of the laser desorption process. In a typical SF-MALDI experiment the cyclodextrin is mixed with well defined molar ratios of pairs of cation precursors in order to evaluate the relative affinity of the host for the two cations. It is then crucial that the density of cations in the desorption plume resembles their original molar ratio in the sample. In our experiments, this is achieved by combining alkali salts of similar lattice energy in each sample, as outlined above. The present SF-MALDI results are shown in Fig. 10.1 and clearly indicate a quantitative order of affinities that decreases with cation size as occurs in the previously studied crown ether molecules [14].

Solvent effects are explored by performing MALDI experiments with the dried droplet method from aqueous solutions, and with RTIL liquid matrix. Fig. 10.2 illustrates the shift of intensity (i.e. relative population) observed with these methods towards the complexes of the CD with the larger cations. In the DD spectrum the strongest yield is found for the CD–Na^+ complex, while in the RTIL spectrum it is found for CD–K^+. These results are expected to hardly reflect the real gas-phase affinities of CD for the alkali cations, which should correspond to those displayed by the SF MALDI measurements. It must be mentioned that the DD method should be affected by solvent effects (preformed ions) and salt effects (lattice energies decreasing with cation size). On the other hand, salt effects are eliminated in the RTIL samples, since the salts are expected to dissociate in the. Hence, the RTIL MALDI spectra should largely reflect the cation affinities of the cyclodextrin in the RTIL polar environment.

We performed collision-induced dissociation (CID) experiments on ternary complexes involving two cations in order to corroborate the preference of the CD for the lighter cations under isolated conditions. Multiple cationized complexes have been previously described under ESI conditions, with a relatively abundant presence in the MS spectra. For example, up to six-eight lithium atoms have been detected to be complexed with CD [6]. In our experiments, even within the RTIL MALDI approach, the doubled lithiated complexed (with lost of 1H) have been detected, denoting the possible linkage of Li to the O center of sugar units. The formation of these complexes are not expected to constitute an appreciable sink for cations affecting the relative affinities determined for the binary CD-M^+ complexes, in particular under the excess of cationizing agents employed for sample preparation in the present study. For instance, the singly charged adduct $[(CD\text{-}H)+(NaLi)]^+$ (deprotonated cyclodextrin, bound to Na and Li) was observed in the MALDI spectra. The CID of this complex consistently led to the loss of the Na cation from the complex. This result reinforces the stronger binding of Li over Na with the CD and corroborates similar earlier experiments for

β-CD [5]. Further insights into the conformational features of these complexes is necessary in order to account for the gas phase CD–alkali affinities. The results of such an investigation are given in the next subsection.

10.3.2 IRMPD spectroscopy and Quantum chemical calculations

In order to shed some light in the complexation mechanism underlying the observed gas-phase affinities of α-CD with the alkali metals, we have performed a thorough IRMPD spectroscopy and quantum chemical calculation investigation of these systems. The computational exploration of the conformational landscape of the isolated α-CD led to a minimum energy conformer of C_6 symmetry with hydroxylic bonding networks groups oppositely oriented in each rim of the molecule. This finding is in concordance with previous studies [7].

The sugar skeleton of the free un-solvated CD is well stabilized by a completed belt of intramolecular hydrogen bonds, with a significant loss of degrees of freedom. This gas phase stability caused by the H-bonds leads to the fact that, in solution, the solvophobic forces are of key importance in the complexation behavior, since they scorted ion-dipole one in the overall balance between the increase of energy cause by cyclodextrine rearrangement against the H–bond network and the diminution provoked by the inclusion process. The gas phase study carried out in this investigation tries to help in the elucidation of conformational features of complexed CD free of solvent effects. In other words, only the intramolecular and guest-host electrostatic and steric interactions will play a role in the observed gas phase affinities of cyclodextrines for different cation metal sizes.

The first question to be solved is the specific location of the cation. IRMPD studies performed within this investigation shed light into this question, giving a definite confirmation that at least for the 1:1 complexes, the guest cation is located in the primary surface of the CD. Fig. 10.3 shows the experimental spectra of the α-CD–Na^+ complex together with the B3LYP prediction for the IR spectrum of conformers in which the cation is bound to the primary and the secondary faces of the CD. It is clearly observed that a full match of the experimental IRMPD bands is achieved for the case in which the guest cation is located in the primary OH side. Similar results are found for the rest of the cations explored, Li^+, K^+ and Cs^+. The main vibrational bands observed in the IRMPD spectrum have been assigned with the help of the B3LYP computation to the vibrational motions indicated in Table 1. A full comparison of experimental and primary–side coordination conformers is depicted in Fig. 10.4. It can be noticed that for the lighter atoms the most intense bands C and D merge into a single envelop within the resolution of the experiments.

The B3LYP conformers that best fit the IRMPD spectra are depicted in Fig. 10.2. As the cation size increases, the CD–M^+ complex displays an increasing number of O...M^+ coordination and a lesser degree of distortion in the native CD. Specifically, the computations indicate that such coordination converts the C_6 symmetry of the free cyclodextrin into C_3 for Li^+ and C_2 for Na^+ and K^+, while a five-fold coordination is reached with the heavier Cs^+ cation. The increase in the O–M^+ coordination does not enhance however the binding energy of the cation to the CD. The coordination of the lighter cations is much tighter, which compensates for the smaller coordination number. As a consequence, the B3LYP Gibbs free energy of binding decreases with cation size, from -414 kJ/mol for Li^+ to -324 kJ/mol for Na and finally -23 kJ/mol for K. The data for the Cs complex is not reproduced because the use of ECP lead to unphysical values of the binding energy due to the uncomparability of data obatined within different method/basis sets. The value given for the Li complexes corresponds to a smaller basis-set, but no qualitative changes are expected.

The energy balance in the complexation phenomena in aqueous solution is not easy to be extrapolated from our gas phase results. We have seen that the complexes with the larger cations keep the CD structure less distorted. More importantly, the larger cations are in those complexes more exposed to solvation than the smaller ones. Consequently, a facile hydration of the large cations is still possible, both from the outide and from the inside of the CD cavity. For instance, the tight C_3 coordination of the Li^+ cation with the primary hydroxyl arms of the CD allows for a more limited number of molecules in the hydration shell around the cation in comparison to the looser C_1 coordination of the Cs^+ cation. This scenario is qualitatively similar to the one found for crown ethers. The balance between solvation effects and CD–M^+ intrinsic binding determines the preference of cyclodextrines for Na^+ and K^+ in aqueous environments, in contrast to their preference for Li^+ in the gas phase.

10.3.3 Conclusions

The gas-phase affinities of cyclodextrins for alkali cations decreases with increasing cation size. The result of previous investigations suggesting that sodium or potassium are favourably bound is likely to be an artifact due to solvent effects or to the wrong choice of cationizing agents and the sample preparation methods. Solvent free MALDI yields realistic gas phase affinities, avoiding condensed phase effects.

The comparison of IRMPD spectroscopy with DFT computations leads to the conclusion that the alkali

Table 10.2: Assignment of the vibrational modes corresponding to the main bands observed in the IRMPD spectra of the α–CD–M^+ complexes. The dominant type of vibration is indicated in each case. Bands are labelled with capital letters A–G in order of increasing wavenumber (see Fig. **??**).

Band	**Band center**	Main vibrational mode
A	945 cm^{-1}	C–C stretching of sugar rings
B	1010 cm^{-1}	C–C–OH·M^+ stretching; ring distortion
C	1040 cm^{-1}	C–C–OH stretching; ring distortion
D	1065 cm^{-1}	glycosidic C–O–C stretching
E	1095 cm^{-1}	In-ring C–O–C stretching; stretching of H-bonded secondary C–O–OH
F	1130 cm^{-1}	stretching of non H-bonded secondary C–O–OH
G	1165 cm^{-1}	concerted vibrations of in-ring and glycosidic C–O–C

cations build a coordination shell on the primary hydroxylic side of the cavity. Upon complexation, the C_6 symmetry of the free cyclodextrin is transformed into symmetries of lower order, *e.g.* C_3 for Li^+, C_2 for Na^+ and K^+ and C_1 for larger guest cations. These structural arrangements give a a naïve view of the affinity trend with the cation size in solution.

Bibliography

[1] A. Villiers. Compt. Rendu. 112 (1891) 536.

[2] J. Szejtli. Chem. Rev. 98(5) (1998)1743.

[3] S. Lee, T. Wyttenbach, M. T. Bowers. Int. J. Mass Spectrom. Ion Process. 167/168 (1997) 605.

[4] L. C. Ngoka, J. Gal, C. B. Lebrilla. Anal. Chem. 66 (1994) 692.

[5] S. Reale, E. Texeidò, F. de Angelis. Annali di Chimica. 95 (2005) 375.

[6] K. P. Madhusudanan. J. Mass Spectrom. 38 (2003)409.

[7] C. P. A. Anconi, C. S. Nascimento, J. Fedoce-Lopes, H. F. Dos Santos, W. B. De Almeida, J. Phys. Chem. A. 111 (2007) 12127.

[8] A. Karpfen, E. Liedl, W. Snor, P. Weiss-Greiler, H. Viernstein, P. Wolschan. J. Incl. Phenom. Macrocycl. Chem. 57 (2007) 38.

[9] Y. Fu, L. Liu, Q. Guo. J. Incl. Phen. Mac. Chem. 43 (2002)223.

[10] E. T. P. Sze, T-W.D. Chan, G. Wang. J. Am. Chem. Soc. Mass. Spectrom. 99 (1998) 166.

[11] a) N.C. Polfer, J. Oomens. Phys. Chem. Chem. Phys. 9 (2007) 3804; b) N.C. Polfer, J. Oomens. Mass Spectrom. Rev. 28 (2009) 468.

[12] D. Andrae, U. Häuβermann, M. Dolg, H. Stoll, H. Preuβ. Theor. Chim. Acta. 77 (1990) 123.

[13] Gaussian 09, Revision A.1, M.J. Frisch, G.W. Trucks, H.B. Schlegel, G.E. Scuseria, M.A. Robb, J.R. Cheeseman, G. Scalmani, V. Barone, B. Mennucci, G.A. Petersson, H. Nakatsuji, M. Caricato, X. Li, H. P. Hratchian, A.F. Izmaylov, J. Bloino, G. Zheng, J.L. Sonnenberg, M. Hada, M. Ehara, K. Toyota, R. Fukuda, J. Hasegawa, M. Ishida, T. Nakajima, Y. Honda, O. Kitao, H. Nakai, T. Vreven, J.A. Montgomery, Jr., J.E. Peralta, F. Ogliaro, M. Bearpark, J.J. Heyd, E. Brothers, K.N. Kudin, V.N. Staroverov, R. Kobayashi, J. Normand, K. Raghavachari, A. Rendell, J.C. Burant, S.S. Iyengar, J. Tomasi, M. Cossi, N. Rega, J.M. Millam, M. Klene, J.E. Knox, J. B. Cross, V. Bakken, C. Adamo, J. Jaramillo, R. Gomperts, R.E. Stratmann, O. Yazyev, A.J. Austin, R. Cammi, C. Pomelli, J.W. Ochterski, R.L. Martin, K. Morokuma, V.G. Zakrzewski, G.A. Voth, P. Salvador, J.J. Dannenberg, S. Dapprich, A.D. Daniels, Ö. Farkas, J.B. Foresman, J.V. Ortiz, J. Cioslowski, D.J. Fox, Gaussian, Inc., Wallingford CT, 2009.

[14] A. R. Hortal, P. Hurtado, B. Martínez-Haya, A. Arregui, L. Bañares. J. Phys. Chem. B. 112 (2008) 8530.

[15] B. Martínez-Haya, P. Hurtado, A.R. Hortal, S. Hamad, J.D. Steill, J. Oomens. J. Phys. Chem. A. 114 (2010) 7048.

Chapter 11

Conclusions and Perspectives

In the previous chapters, we have presented our results on molecular and laser spectroscopy on model inclusion complexes mimicking complex supramolecular behavior. The main conclusions obtained will be outlined here:

• Microwave Spectroscopy has been employed to characterize a wide set of rotamers of the 15-crown-5 ether(15c5). Due to its flexible backbone, the 15c5 molecule can display a variety of qualitatively different conformations (*e.g.*, of prolate and oblate character) within a narrow energetic range. Each of such conformations finds an optimum balance between the flexibility of the ether backbone and the intramolecular O$\cdots$O repulsions and CH$\cdots$O attractions. The present study has shown that MB–FTMW spectroscopy, combined with quantum computations at the MP2 level, constitutes a powerful tool to unveil the fine aspects of the conformational landscape of these systems. Our results also pave the way for the study of higher molecular weight systems when care is taken on experimental conditions.

• Infrared Multiphoton Dissociation experiments on protonated ethers has been carried out in order to investigated intramolecular proton bridge formation and delocalization effects. The IRMPD experiments show clear evidence of O$\cdots$H$^+\cdots$O proton bridges in the native crown ethers 18-crown-6, 15 crown-5 and 12-crown-4. For these systems, the vibrational bands of the IRMPD spectrum are significantly broadened due to proton delocalization. In contrast, for the N–substituted aza-18-crown-6 and diaza-18-crown-6 substrates, the proton is localized on a nitrogen site. Hence, the IRMPD spectrum displays well defined vibrational bands qualitatively similar to those found in the complexes with the alkali or alkaline-earth cations. Sharing between the two opposed nitrogens in the diaza-crown does not take place. In turn, IRMPD spectroscopy has revealed itself as a sensitive probe to detect proton delocalization effects. These effects have been followed as well by means of Hartree-Fock Molecular Dynamics and the results are consistent with the scenario outlined above of the formation of dynamic proton bridges in the native crown ethers but not in the N-substituted crowns.

• Since the group has previously studied the conformational features of crown ethers with alkali metals, we have faced the task of incorporating the effect of an increased cation charge on the conformational landscape of this model molecules. Firstly, we have carried out IRMPD studies of 18c6 with alkaline–earth cations Mg^{2+}, Ca^{2+}, Sr^{2+} and Ba^{2+}. The structure of the spectrum in combination with B3LYP computations has served to define conformational features dominated by symmetric structures. These structures vary from a low energy conformer of compact D_2 geometries for the smaller cations, Mg^{2+} and Ca^{2+}, to a more open C_2 configuration for Sr^{2+} and to a planar D_{3d} structure for Ba^{2+}. In general, the effect of the charge is the stabilization of folded geometries.

• A more complete view on crown ether complexes with double charged cations (Cu^{2+}, Ca^{2+} or Ba^{2+}) has been performed by carrying out vibrational spectroscopy in combination with quantum–chemical computations of tweezer–like (ternary) complexes of the 18–crown–6 ring molecule. The structure of such complexes display a strong dependence on cation size. While the ternary complexes built on Cu^{2+} show a very asymmetric structure where one crown molecule coordinates much more tightly than the second one with the cation in a folded conformation, for bigger cations (such as Ca^{2+} and Ba^{2+}) the complexes become more symmetric and leads to a balanced coordination of the two ethers with the cation in a C_2 conformation in which all 12 ether oxygens are involved.

• The experience acquired within the research performed in this thesis is guiding current work of the UPO group around the complexes formed by chiral substituted crown ethers with the enantiomers of protonated amines and aminoacids. This line of work has already led to relevant results and will be the topic of several publications in the near future.

• Our results combining MALDI and IRMPD experiments of cyclodextrins with alkali metals has proven a $Li^+ > Na^+ > K^+$ size-dependent cation affinity rank on the gas phase. Previous studies showing predominance of sodium or potassium in wet MALDI preparation are likely to be affected by solvent effects. Hence, special care must be taken in this type of experiments in ensuring solvent–free conditions. DFT calculations indicate that the alkali cations build a coordination structure preferentially with the primary carboxylic groups od the rim of the cyclodextrin. This prediction has been confirmed by our IRMPD spectroscopy and DFT studies of the complexes of α–cyclodextrin with the alkali cations, which also show that the cation transforms the C_6 symmetry of the free cyclodextrine into a C_3 for Li^+, C_2 for Na^+ and K^+ and C_1 for the greater cations.

• The group is currently exploring in detail the effect of solvents and environment in the complexation of cyclodextrins and other model macrocycles (*e.g.* crown ethers and calixarenes). Particular efforts are being devoted to the study of the formation of inclusion complexes in ionic liquids. For this purpose, novel methodologies are under development that are based on the direct MALDI analysis of mixtures of the macrocycles with guest cations and molecules in ionic liquid solution.